VILNIUS UNIVERSITY

CENTER FOR PHYSICAL SCIENCES AND TECHNOLOGY

VYTAUTAS KLIMAVIČIUS

SOLID STATE NMR SPECTROSCOPY OF COMPLEX INNOVATIVE MATERIALS

Doctoral dissertation

Physical Sciences, Physics (02P)

Vilnius, 2017

The dissertation has been developed during the years 2013 – 2017 in Vilnius University

Supervisor – prof. habil. dr. Vytautas Balevičius (Vilnius University, Physical sciences, Physics – 02P)

VILNIAUS UNIVERSITETAS

FIZINIŲ IR TECHNOLOGIJOS MOKSLŲ CENTRAS

VYTAUTAS KLIMAVIČIUS

KOMPLEKSINIŲ INOVATYVIŲJŲ MEDŽIAGŲ KIETOJO KŪNO BMR SPEKTROMETRIJA

Daktaro disertacija

Fiziniai mokslai, Fizika (02P)

Vilnius, 2017 metai

Disertacija rengta 2013 – 2017 metais Vilniaus universitete

Mokslinis vadovas – prof. habil. dr Vytautas Balevičius (Vilniaus universitetas, fiziniai mokslai, fizika – 02P)

Table of Content

Abbreviations

ACP – Amorphous clustered phosphate phase

ADP – Amonium Dihydrogen Phosphate

BD – Bloch Decay

CA – Commercially available

CaHap – Calcium Hydroxyapatite

CaP – Calcium Phosphate

CP – Cross Polarization

CSA – Chemical Shift Anisotropy

EDTA – 1,2-ethylendiaminetetraacetic acid

EDX – Energy Dispersive X-Ray spectroscopy

EG – ethylene glycol

EM – Electron microscopy

FAp – Fluorapatite

FTIR – Fourier Transform Infrared spectroscopy

FWHM – Full Width at Half Maximum

GL – glycerol

HAp – Hydroxyapatite

HETCOR – Heteronuclear Correlation Spectroscopy

HH – Hartmann Hahn

MAS – Magic Angle Spinning

NMR – Nuclear Magnetic Resonance

NS – Neutron Scattering

RF – Radio Frequency

SEM – Scanning Electron Microscopy

TA – tartaric acid

TEM – Transmission Electron Microscopy

XRD – X-Ray Diffraction

Introduction

Complex structures, according definition, are constructed by combining and/or removing parts from simple geometrical shapes, namely cuboids, cylinders, prisms, spheres, etc. There are many successful attempts to synthesise organic and inorganic materials possessing complex structures [1-6]. Fast development of state of the art synthesis of complex innovative materials these days is undeniable. The demand of characterization at a nano- and meso-scale is *per se* important for the development of advanced synthesis routes in order to apply them in innovative industry.

Moreover, many biological solids, such as bones, dentin, enamel, etc. possess complex inorganic architecture, particularly their structures are composed of nanometer-sized platelets and/or needles incorporated within organic fibrils [7-10]. The idea to treat diseases and injuries by replacing the damaged bone/dentin/etc area by replacing with something similar is not new [11]. To date, there are many techniques developed for this reason, namely Calcium phosphate (CaP) bone graft substitutes, injectable CaP pastes, cements and moldable CaP pastes [12-16]. As well as attempts to manufacture CaP coatings on metallic implants to achieve better mechanical properties preserving the biocompatibility at the same time [17]. Moreover, 3D printing techniques were employed to shape artificial bone implant out of HAp powder [18, 19].

Whereas above mentioned approaches uses CaP materials which should possess complex structures at the nano-scale, new synthesis routes as well as the characterization methods are extremely important because the osteoinductivity, the ability to absorb guest implant, highly depends on the organization of pores, surfaces and cavities in the CaP materials [20, 21]. As the CaP complex solids at the nano- or meso- scale have much larger surface area compared to the crystalline ones or the containing amorphous clustered phosphate phase (ACP), a powerful probe could be the analysis of the surfaces *versus* bulk material in the complex structures. The first intuitive approach for such analysis could be the Electron microscopy (EM) methods [22, 23].

Nevertheless, obtaining the information about chemical composition is not possible. Other techniques, such as FTIR and NMR, might be the methods of choice, as they are powerful to provide information about chemical composition and interactions present at a molecular level [24-26].

There are many NMR experimental methods, namely Bloch decay (BD), Cross Polarization (CP), Heteronuclear correlation (HETCOR), Magic Angle Spinning (MAS), etc and taking into the account the number of NMR active isotopes the possibility to employ it in the analysis of materials possessing complex structure is promising [26, 27 and citations therein]. Though, sometimes there are experimental challenges, such as long relaxation values, low natural abundance of the isotope of interest, large magnitude of anisotropic interactions. However, there are sophisticated experimental approaches which cope with such problems but the qualified experimenter is needed. Probably the most interesting approaches are these which exploit the dipolar coupling as it is distance dependent ($\sim 1/r^3$) between the interacting spins [27 and citations therein]. If the experimental data is processed properly, the obtained results might be used complimentary to the X-Ray diffraction (XRD) or neutron scattering (NS) data, recently, this area was named as NMR crystallography [27]. However, the introduction of crystallographic problems in the field of NMR is new and the existing methods, namely CP kinetics, REDOR, TEDOR, etc, is not always possible to adopt for materials possessing complex structures [27-29]. The reason is that basically translational order is interrupted and the dipolar couplings become distributed within unknown distribution profile. Therefore the development of NMR based methods capable of coping with crystallographic problems in nanostructured materials would be very welcome.

1.1. Goals and tasks of the work

Regarding to the above mentioned problems and possibilities occurring applying NMR spectroscopy for studying complex solids, namely nano-structured Calcium Hydroxyapatites (CaHAps), the main goal is to analyse the possibility to employ NMR spectroscopy methods for characterising complex nano-structured CaHAps possessing different morphological features. To achieve this, the following task are formulated:

1. To investigate the possibility to use conventional ^{1}H and ^{31}P NMR spectroscopy methods for analysing morphological difference in various sol-gel derived nano-structured and containing amorphous clustered phosphate phase (ACP) complex CaHAps.
2. To investigate the possibilities to employ existing Cross-Polarization (CP) kinetics models for studying complex materials.
3. To complement existing CP kinetics models to describe CP kinetics behaviour through the whole observed dynamic range.
4. To exploit the possibilities to distinguish the difference in morphological features situating within different CaHAp samples from CP kinetics data.

1.2 Statements of the doctoral thesis

1. ^{1}H and ^{31}P NMR spectroscopy is capable to discriminate differences in surface and bulk species in the sol-gel derived nano-structured complex CaHAps.
2. Cross Polarization (CP) kinetics behaviour in the nano-structured CaHAps is described within the whole observed dynamic range using various dipolar coupling distributions, such as Gauss, Lorentz, etc, but fine structural effects are revealed using radial distribution approach.
3. The angularly-averaged and purely distance-depending distribution profiles of coupled spins can be determined by the proper

mathematical treatment that has been created and that allowed to reduce the Fourier - Bessel (Hankel) transform to the routine Fourier transform.

4. The developed CP kinetics processing models are powerful enough to characterise nano-structured materials in the sub nano scale.

1.3. Scientific novelty

1. Studied nano-structured CaHAps are unique as they were synthesised in Vilnius University using novel aqueous sol-gel synthesis routes and have never been studied by any experimental methods before.
2. Difference of organisation of structural hydroxyl groups in the nano-structured CaHAps derived using different complexing agents was shown for the first time.
3. Developed CP kinetics models allowed to describe the CP behaviour within the whole observed dynamic range in the nano-structured as well as in the amorphous clustered materials for the first time.
4. The angular part of the dipolar coupling interaction was averaged during processing the CP kinetics applying mathematical treatment which allowed to avoid Fourier - Bessel (Hankel) transform.
5. It was shown that non-classical *I*-*I**-*S* CP kinetics model at a certain circumstances converge to the classical one *I*-*S*.
6. Morphological differences in the sol-gel derived nano-structured CaHAps applying novel CP kinetics processing models were revealed for the first time.
7. It was shown that NMR spectroscopy might be used as a probe for development of target nano-structured CaHAps synthesis.

1.4. Publications included in the thesis

1. V. Klimavicius, A. Kareiva, V. Balevicius, *Solid-State NMR Study of Hydroxyapatite Containing Amorphous Phosphate Phase and Nano-Structured Hydroxyapatite: Cut-Off Averaging of CP MAS Kinetics and Size Profiles of Spin Clusters*, The Journal of Physical Chemistry C, 118 (49), 28914-28921, (2014).

2. L. Dagys, V. Klimavičius, J. Kausteklis, A. Chodosovskaja, V. Aleksa, A. Kareiva, V. Balevičius, *Solid-state ^{1}H and ^{31}P NMR and FTIR spectroscopy study of static and dynamic structures in sol-gel derived calcium hydroxyapatites*, Lithuanian Journal of Physics, 55 (1), 1-9, (2015).

3. V. Klimavicius, L. Dagys, V. Balevicius, *Sub-Nano Scale Order and Spin Diffusion in Complex Solids through the Processing of Cross Polarization Kinetics*, The Journal of Physical Chemistry C, 120 (6), 3542–3549, (2016).

4. S. Kareiva, V. Klimavicius, A. Momot, J. Kausteklis, A. Prichodko, L. Dagys, F. Ivanauskas, S. Sakirzanovas, V. Balevicius, A. Kareiva, *Sol–gel synthesis, phase composition, morphological and structural characterization of $Ca_{10}(PO_4)_6(OH)_2$: XRD, FTIR, SEM, 3D SEM and solid-state NMR studies*, Journal of Molecular Structure, 1119, 1-11, (2016).

5. L. Dagys, V.Klimavicius, V. Balevicius, *Processing of CP MAS kinetics: Towards NMR crystallography for complex solids*, The Journal of Chemical Physics, 145, 114202, (2016)

6. K. Kristinaitytė, L. Dagys, J. Kausteklis, V. Klimavicius, I. Doroshenko, V. Pogorelov, N. R. Valevičienė, V. Balevicius, *NMR and FTIR studies of clustering of water molecules: From low-temperature matrices to nano-structured materials used in innovative medicine*, Journal of Molecular Liquids, 235, 1-6, (2017).

7. V. Klimavicius, L. Dagys, V. Chizik, V. Balevicius, *CP MAS Kinetics Study of Ionic Liquids Confined in Mesoporous Silica: Convergence of Non-*

Classical and Classical Spin Coupling Models, Applied Magnetic Resonance, 48, 673-685, (2017).

8. V. Balevicius, L. Dagys, V. Klimavicius, *^{1}H and ^{31}P NMR spectroscopy of dynamic structures in nano-and mesostructured hydroxyapatites*, Journal of Materials Sciences and Engineering, 4 (3), 55, (2015). Conference Proceedings.

1.5. Other publications

1. V. Balevicius, Z. Gdaniec, V. Klimavicius, A. Marsalka, J. Plavec, *NMR monitoring of nonequilibrium aggregation in ionic solutions*, Chemical Physics Letters 503, 235-238, (2011)

2. V. Aleksa, J. Kausteklis, V. Klimavicius, Z. Gdaniec, V. Balevicius, *2D Raman correlation and NMR spectroscopy study of liquid crystalline ionogel phase in ionic liquid/H2O mixtures: the states of water*, Journal of molecular structure 993, 91-96, (2011)

3. V. Klimavicius, Z. Gdanec, J. Kausteklis, V. Aleksa, K. Aidas, V. Balevicius, *NMR and Raman spectroscopy monitoring of proton/deuteron exchange in ionic liquids forming hydrogen bond: a dual role of anions*, Journal Physical Chemistry B 117, 10211-10220, (2013)

4. V. Klimavicius, Z. Gdaniec, V. Balevicius, *Very short NMR relaxation times of anions in ionic liquids: New pulse sequence to eliminate the acoustic ringing*, Spectrochimica Acta Part A: Molecular and Biomolecular Spectroscopy 132, 879-883, (2014)

5. V. Klimavicius, V. Bacevicius, Z. Gdaniec, V. Balevicius, *Pulsed-field gradient ^{1}H NMR study of diffusion and self-aggregation of long-chain imidazolium-based ionic liquids*, Journal of Molecular Liquids, 210, 223-226, (2015)

6. L. Pavasaryte, A. Katelnikovas, V. Klimavicius, V. Balevicius, A. Krajnc, G. Mali, J. Plavec, A. Kareiva, *Eu^{3+} doped $Y_{3-x}Nd_xAl_3O_{12}$ garnet: synthesis and*

structural investigation, Physical Chemistry Chemical Physics, 19, 3729-3737, (2017).

7. L. Pavasarytė, A. Katelnikovas, V. Klimavicius, V. Balevicius, A. Momot, M. Van Bael, A. Hardy, A. Kareiva, *Eu^{3+} - doped $Y_{3-x}Sm_xAl_5O_{12}$ garnets: synthesis and structural investigation,* New Journal of Chemistry, Submited.

1.6. Presentations at the conferences

1. V. Klimavičius, V. Balevičius, *Amorphous versus nano-structured hydroxyapatites: cut-off averaging of CP MAS kinetics,* The 16th Central European NMR Symposium (CEUM 2014), 2014, Zagreb, Croatia.

2. V. Balevicius, Z. Gdaniec., V. Klimavicius, V. Bacevicius, A. Marsalka, *NMR study of ionic liquids: perfect mixing, non-equilibrium aggregation, diffusion and relaxation,* 2nd International Conference on Ionic Liquids in Separation and Purification Technology (ILSEPT), 2014, Toronto, Canada.

3. V. Klimavicius, A. Marsalka, V. Balevicius, *NMR study of molecular-ionic interactions, micro-diffusion, relaxation, mixing and proton/deuteron exchange in ionic liquids,* 9th Liquid Matter Conference - Liquids 2014, 2014, Lisbon, Portugal.

4. S. Kareiva, Z. Stankeviciute, A. Beganskiene, A. Selskis, F. Ivanauskas, V. Klimavicius,V. Balevicius, S. Sakirzanovas , A. Kareiva, *Reproducibility of Sol-Gel Synthesis method: case of Calcium Hydroxyapatite,* Chemistry and Chemical Technology, 2015, Vilnius, Lithuania.

5. V. Klimavičius, L. Dagys, V. Balevičius, *Kalcio hidroksi apatititų kietojo kūno BMR tyrimas,* 41 – oji Lietuvos nacionalinė fizikos konferencija, 2015 Vilnius, Lithuania.

6. L. Dagys, V. Klimavičius, V. Balevičius, T. Šalkus, A. Dindune, A. Kanepe, J. Ronis, A. Kežionis, A.F. Orliukas, *BMR relaksacijos tyrimas kietuosiuose*

NASICON elektrolituose, 41 – oji Lietuvos nacionalinė fizikos konferencija, 2015 Vilnius, Lithuania.

7. V. Balevicius, L. Dagys, V. Klimavicius, *^{1}H and ^{31}P NMR spectroscopy of dynamic structures in nano-and mesostructured hydroxyapites,* 269th OMICS International Conference and Exhibition on Mesoscopic and Condensed Matter Physics, 2015, Boston, USA.

8. V. Balevicius, V. Klimavicius, *Hydroxyapatite with Amorphous Phosphate Phase versus Nano-structured Hydroxyapatite: Solid-State NMR, FTIR and Raman Study of Static and Dynamic Structures,* International Conference on Advances in Functional Materials, 2015, New York, USA.

9. V. Balevicius, V. Klimavicius, L. Dagys, *Solid state NMR study of materials for innovative medicine: sub-nano structure and dynamics of spin clusters containing hydroxyl groups,* XXIth International Conference on Horizons in Hydrogen Bond Research, 2015, Wroclav, Poland.

10. A. Marsalka, V. Klimavicius, I. Svoboda, H. Fuess, V. Balevicius, *^{1}H, ^{13}C, ^{17}O NMR spectroscopy and X-ray study of media versus temperature effects on proton dynamics in hydrogen bond in picolinic acid N-oxide,* XXIth International Conference on Horizons in Hydrogen Bond Research, 2015, Wroclav, Poland.

11. J. Kausteklis, V. Klimavicius, S. Kareiva, V. Aleksa, A. Kareiva, V. Balevicius, *FTIR and NMR spectroscopy of sol-gel derived calcium hydroxyapatites: correlation of experimental data and the size profiles of sub-nanospin clusters,* Functional Materials and Nanotechnologies, 2015, Vilnius, Lithuania.

12. V. Klimavicius, L. Dagys, V. Balevicius, A. Kareiva, *Solid State NMR study of calcium hydroxyapatites: cut-off averaging of dipolar coupling, spin clusters, CP beating and relaxation effects*, Functional Materials and Nanotechnologies, 2015, Vilnius, Lithuania.

13. V. Klimavicius, L. Dagys, V. Balevicius, A. Kareiva, *Solid State NMR study of complex solids*, Pittcon, 2016, Atlanta, USA.

14. S. Bielskute, K. Aidas, V. Klimavicius, G. Pitsevich, V. Balevicius, *NMR and quantum chemistry study of interaction of water molecules with ions and ionic liquids: towards heterogeneity and formation of water pockets*, PLMMP, 2016, Kyiv, Ukraine.

15. V. Balevicius, V. Klimavicius, L. Dagys, *Spectroscopy of states of water in advanced nao-structured materials for innovative medicine,* American Advanced Materials Congress, 2016, Miami, USA

16. L. Pavasarytė, V. Klimavičius, V. Balevičius, A. Katelnikovas, A. Kareiva, *Investigation of structural and luminescense properties of* Eu^{3+}*-doped* $Y_{3-x}Sm_xAl_5O_{12}$ *garnets,* Functional Materials and Nanotechnologies, 2017, Tartu, Estonia.

1.7. Authors contribution

The aqueous sol-gel synthesis using different complexing agents were performed in the Sol-Gel group in the department of the inorganic Chemistry, Vilnius University (Head. Prof. Habil. Dr. Aivaras Kareiva). SEM micrographs and XRD patterns (shown in the appendix) were accomplished by the same group. The majority of the NMR experimental work presented in the thesis was done by the author. Parts of the NMR experimental work published in the above mentioned publications was carried out by Laurynas Dagys but the author was participating during measurements. Other experimental work published in the publications was done by the co-authors. The data analysis and above publications preparation were a team work of all authors.

2. Overview

2.1. Materials based on Calcium Phosphates

There is big variety of calcium phosphates and the most common of them are: monocalcium phosphate monohydrate [$Ca(H_2PO_4)_2 \cdot H2O$], dicalcium phosphate (Monetite) [$CaHPO_4$], dicalcium phosphate dehydrate (Brushite) [$CaHPO_4 \cdot 2H_2O$], hydroxyapatite [$Ca_{10}(PO_4)_6(OH)_2$], etc [7]. These materials are of the big importance because they are found in biological hard tissues, such as, bone, enamel, dentin, etc [30]. The idea to replace the damaged tissue by something with close biological similarity is not new, the first idea was proposed in 1920 [11]. Up to now, there are numerous studies performed analysing possibilities to apply these compounds in innovative medicine [7 and references therein]. In present thesis only calcium hydroxyapatites possessing different morphological complex features in nano and meso scale were investigated. For this reason from now only hydroxyapatites will be discussed.

Calcium Hydroxyapatite being thermodynamically the most stable form of calcium phosphates plays a big role in implantology, orthopedic and periodontal surgery [9, 31]. What is more, natural bone like tissues are formed mostly from biological apatite [13]. Majority of bone mineral consist of nanometer or micrometer scale platelets and needles together with incorporated collagen fibrils [32, 33]. Such nanostructured HAp and HAp nanorods were successfully synthesized and showed their application possibilities [34, 35]. There are different attempts to use HAp, such as, bulk nanostructured powders, injectable cements, pastes, moldable pastes [34-39]. Cements and pastes are easier to be operated with as long as they do no fall outside the borders of the repaired defect. CaHAp has often been used to study properties of antiresorptive agents for the prevention and treatment of bone diseases [40]. Although sintered CaHAp has been used as artificial bone substitute in clinics, bone apatite is not high crystalline HAp. Moreover, current artificial bone substitutes are inferior to auto-graft with respect to osteoconductivity (property to form new bone on the surface of materials). It has been also reported that

cells attachment, proliferation and differentiation behaviour is regulated on the crystallinity and surface morphology [4, 10, 41, 42].

The challenges and opportunities of controlling the morphological characteristics of phosphate materials were also put forward [5, 6]. The specific chemical structural and morphological properties of CaHAp bioceramics are highly sensitive to the changes in chemical composition and processing conditions [43-46]. The solid-state synthesis of CaHAp from oxide or inorganic salt powders usually requires extensive mechanical mixing and lengthy heat treatments at high temperatures [47, 48]. These processing conditions do not allow facile control over micro-structure, grain size and grain size distribution in the resulting powders. It has been well demonstrated that the sol-gel process offers considerable advantages of good mixing of the starting materials and excellent chemical homogeneity and stoichiometry of the CaHAp. Several sol-gel approaches, starting from nonaqueous solutions of different precursors of calcium and phosphorus, have been used for the preparation of HAp powders [50-52]. The major limitation for their applications was found to be very low solubility of the calcium alkoxides in the organic solvents and their low reactivity which caused deviations from the stoichiometry of the final materials. The aqueous synthesis route of sol-gel preparation offers an effective and relatively simple way to produce CaHAp.

In this dissertation there were complex nano-structured CaHAp materials analysed which were produced via an aqueous sol-gel synthesis route using different complexing agents, namely, 1,2–ethylendiaminetetraacetic acid, $C_{10}N_2H_{16}O_8$ (EDTA), ethylene glycol $C_2H_6O_2$ (EG), tartaric acid $C_4H_6O_6$ (TA), and glycerol $C_3H_8O_3$ (GL). Whereas it is behind the scope of this thesis, the details of the synthesis will not be discussed. The precise sol-gel synthesis route is presented in the ref. 53.

2.2. Methods used to characterize innovative materials

There are many experimental techniques used to study complex innovative materials, such as, hydroxyapatites possessing various morphological features. Namely, these methods are small angle X-ray diffraction (XRD), neutron scattering (NS), Fourier transform infrared spectroscopy (FTIR), Raman spectroscopy, scanning electron microscopy (SEM), transmission electron microscopy (TEM), Optical microscopy (OM) and nuclear magnetic resonance spectroscopy (NMR).

Using XRD it is possible to analyse lattice parameters [54] or crystallographic aspects of the nanostructures, namely the crystallinity of the system of interest [55]. Whereas NS is more powerful to probe hydrogen atoms, it is often used to analyse such problems as hydroxyl ion deficiency within HAp structures [56]. Moreover, NS was employed to study silicon substituted HAps, to explain higher bioactivity and the substitution process in the silicon-substituted HAps [57 - 59]. SEM, TEM and OM microscopy techniques enables to study the morphological features of the complex materials. Mainly SEM or TEM is a standard technique to show morphology and nano-structures in newly synthesised complex materials and composites, such as coatings or functionalised nano-rods [22, 23, 60, 63]. What is more, there is a successful attempt to reconstruct 3D structures of the CaHAps possessing complex nano-structures [53]. Vibrational spectroscopy (FTIR and Raman) is often employed due to its availability across the laboratories and powerfulness to solve structural problems as well as provide information about chemical composition [24, 25, 53, 61 - 63]. Whereas other experimental techniques accept Solid State NMR were not used in this dissertation, hereinafter achievements in studying complex materials using NMR as well as experimental improvements will be discussed.

The targets for Solid-State NMR analysis are the nuclei which possess spin quantum number greater than zero $I \geq 1/2$. In the case of CaHAps , ^{1}H, ^{31}P, ^{17}O and ^{43}Ca could be used as a target. Unfortunately, only ^{1}H and ^{31}P are the

nuclei of a choice as they are not quadrupolar and have high gyromagnetic ratio, as well as their natural abundance are 99.9% and 100%, respectively. In order to obtain ^{17}O and ^{43}Ca NMR spectra isotopic enrichment and high magnetic fields or hybrid techniques, namely Dynamic Nuclei Polarization (DNP), are needed [64]. Therefore, only few studies where ^{43}Ca was employed are present, nevertheless, two inequivalent calcium sites were resolved for CaHAp and nanocrystalline -CaHAp [64-66]. However, no application of ^{17}O for studying CaHAps were found in literature, only application for apatite-type lanthanum silicates is present [67]. Other nuclei (^{1}H and ^{31}P) were widely employed for studying CaHAps and FAps possessing complex structures, namely crystalline, containing amorphous clustered phosphate phase, nanostructured, biological, etc CaHAps [25, 68-74]. Employing various ^{1}H and ^{31}P based NMR techniques, such as BD, CP, HETCOR, Inversion recovery, etc Osman et.al managed to assign representative spectral lines for surface and bulk chemical species appearing in various HAp specimens [25]. Local environments in biomimetic hydroxyapatite-gelatin nano composites were analysed employing ^{1}H-^{31}P HETCOR technique, the presence of both ACP and nano-structured phases was proved [71]. What is more, the incorporation of silicon, carbonate, magnesium ions in the HAp structures and their degradation under physiological conditions were probed using ^{1}H and ^{31}P NMR techniques [71, 75]. Other important aspects, such as the incorporation of structural molecular water in the HAp structure and the pore filling peculiarities in the deuterated nano-structured HAp were analysed by means of ^{2}H and ^{1}H NMR [25, 77]. There is a sufficient high number of successful attempts to employ CP kinetics for analysing HAps [70, 72, 75, 76]. It was shown that the CP transfer rate constants as well as the relaxation times in the rotating frame are different for the amorphous clustered and the nano-crystalline HAps which enables fast discrimination of both species [70, 72]. Moreover, transient oscillations were observed in CP kinetics and fitted with the theoretical curves for nano-crystaline, hydratated and containing incorporated magnesium ions HAps [75,

78, 79]. Nevertheless, rather low data point density in these studies was achieved which may lead to inappropriate results.

Moreover, as the CP mechanism rely on the dipolar coupling which is distance dependent (~$1/r^3$) the dipolar coupling distance distribution may be obtained but serious problem arises: nano-structured materials possess very complex structure and this leads to a very complex dipolar coupling distribution. There are successful attempts to obtain proximities between interacting 1/2 spins, namely ^{1}H-^{31}P, ^{1}H-^{19}F, ^{19}F-^{29}Si, ^{1}H-^{13}C, etc, as well as between spin 1/2 and quadrupolar nuclei, namely ^{1}H-^{27}Al, ^{31}P-^{27}Al using various techniques which employ dipolar coupling as source of information, namely CP-MAS, REDOR, TEDOR, PINTASEMA-MAS, etc [28, 80-89]. It is worth mentioning that Mali et al and Fyve et al managed to average the angular part of the dipolar coupling expressing powder average by Bessel functions of the first kind while others were recalculating proximities from pake-like patterns [86, 28]. Very nice coincidence between proximities obtained using above mentioned NMR based methods and the conventional crystallographic methods, such as XRD or ND were met. Nevertheless, the analysed solids we conventional powder samples while for the complex solids the situation is much more complicated. Therefore, the existing models will be reviewed and modified in order to process experimental data obtained for the complex nano-structured materials studied this work.

3. Methodology

Nuclear magnetic resonance (NMR) is a physical phenomenon when an ensemble of nuclei absorb and reemits radiofrequency radiation. It was first observed in 1946 by two independent groups from Harvard (E.M. Purcell, H.G. Torrey, R.V. Pound) and Stanford (F. Bloch, W. Hansen, M.E. Pacard) Universities [96, 97]. Later on, in 1952 the leaders of both groups were awarded by the Nobel Prize. For the development of modern NMR methods, namely Fourier transform and multidimensional NMR, R.R. Ernst from ETH got Nobel Prize in 1991. These days NMR widespread to many fields, namely High Resolution, Solid State, Relaxometry, Gradient, Tomography, etc. The variety of objects of interest is as well very broad, ranging from small organic molecules to extremely large biological molecules, such as DNA, proteins, etc in liquid or solid state. What is more, if the crystal lattice is present in a solid, NMR might be used a complementary technique to XRD and ND. It is a very promising and developing field, often called as NMR crystallography [27].

In a forthcoming chapter only the most important topics regarding the dissertation will be touched. The reasoning for such choice is that there are numerous literature sources available and, in the opinion of the author, there is no necessity to summarize them.

3.1. Solid State NMR spectroscopy

Solid state NMR is widely used in many studies analysing novel complex materials including nanostructured apatites [25, 71-85]. Whereas the scope of this work is NMR some experimental methods will be discussed more in details, namely wideline NMR, MAS and CP.

From the first view wideline NMR is the simplest technique out of all solid state NMR techniques. The sample is fixed in the static $\boldsymbol{B}_0$ magnetic field. In most cases the sample is placed in a perpendicular NMR coil to the static $\boldsymbol{B}_0$ field. Having such experimental conditions all anisotropic interactions such as

chemical shielding or quadrupolar are present. For the sake of simplicity let's take that we are analysing non quadrupolar nuclei which are characterised by spin quantum number *I* equal to 1/2. If we have a single crystal, depending on the orientation in the $\boldsymbol{B}_0$ field different spectral lines will be observed. This is explained by the fact that nuclei are shielded not necessary in a spherical manner unlike in liquids where molecular tumbling averages it. Therefore chemical shielding becomes a tensor unit that in the principal axis coordinate system (PACS) can be written as:

$$\sigma = \begin{pmatrix} \sigma_{xx} & 0 & 0 \\ 0 & \sigma_{yy} & 0 \\ 0 & 0 & \sigma_{zz} \end{pmatrix}. \tag{3.1.1}$$

Depending on the tensor orientation in $\boldsymbol{B}_0$ the spectrum will shift (Fig. 3.1.1)

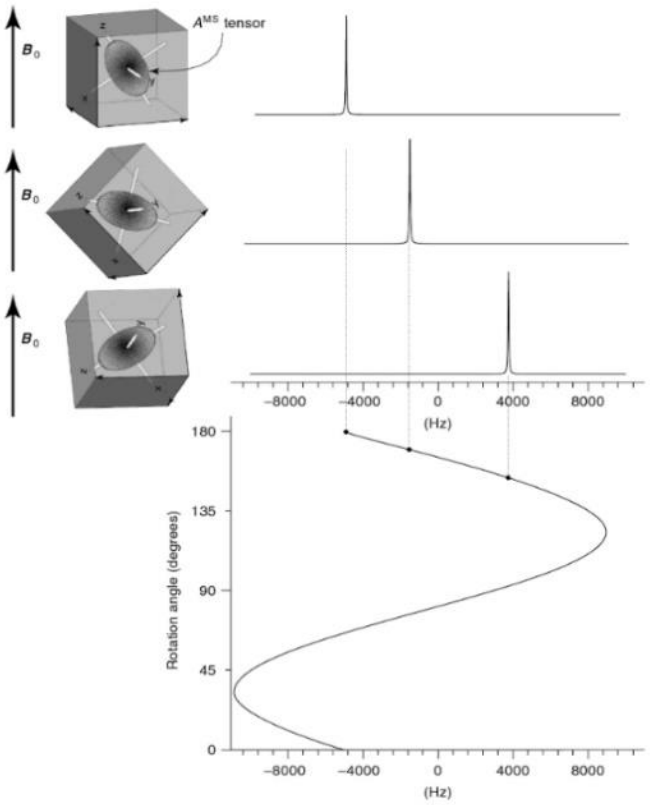

Fig. 3.1.1. Sketch of the effect of varying the orientation of a single crystal in laboratory frame on the NMR spectrum of a single tensor. [27]

If the sample is a powder, situation changes dramatically. Now the sample consist of many randomly oriented crystallites which correspond to different

chemical shielding. The frequency shift arising from the shielding interaction can be written as:

$$\Delta\omega = -\sigma_{iso}\omega_0 - \frac{\omega_0\Delta_{CS}}{2} \times ((3\cos^2\beta - 1) - \eta\sin^2\beta\cos 2\alpha), \quad (3.1.2)$$

where isotropic shielding , anisotropy, and asymmetry are introduced:

$$\sigma_{iso} = \frac{1}{3}(\sigma_{xx} + \sigma_{yy} + \sigma_{zz}), \quad (3.1.3)$$

$$\Delta_{CS} = \sigma_{zz} - \sigma_{iso}, \quad (3.1.4)$$

$$\eta = \frac{\sigma_{xx} - \sigma_{yy}}{\Delta_{CS}}. \quad (3.1.5)$$

Depending on these parameters the shape of spectral line changes (fig 3.1.2).

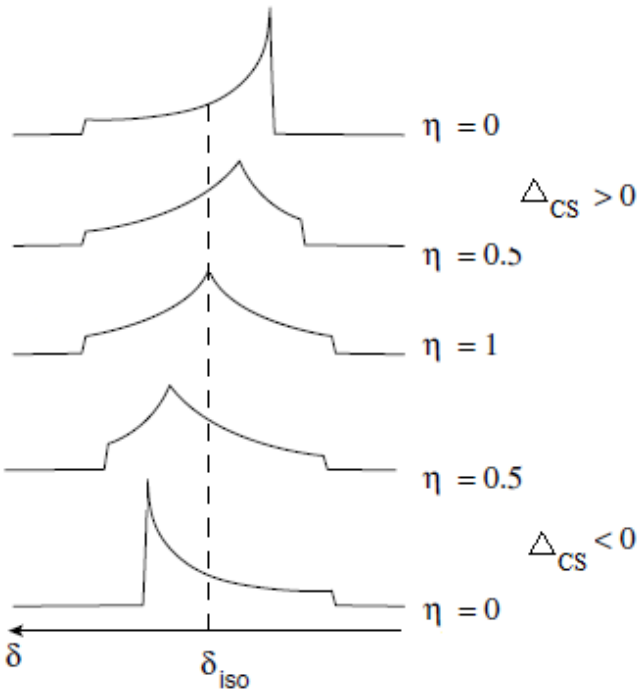

Fig. 3.1.2. Powder pattern NMR spectral line dependency on chemical shift anisotropy and anisotropy parameter [29].

Chemical shift anisotropy parameters give rich information about chemical environment around the nuclei. What is more, they are sensitive to structural changes and chemical composition in the sample. Though in the presence of more than one overlapping spectral line the unambiguous determination of

chemical shift parameters is hard. Therefore more complicated experimental technique as Magic angle spinning (MAS) is needed.

Nowadays MAS NMR is the most widely used solid state NMR technique. The goal of MAS is to reduce or to eliminate the anisotropic interactions by employing the symmetry feature existing in them. The experimental setup is rather complicated: the powdered sample is placed in a rotor which is spun rapidly inside the NMR coil which is tilted at 54.74 degrees along the static magnetic field $\boldsymbol{B}_0$. The idea of MAS is to introduce the time dependency on the NMR Hamiltonian. For the sake of simplicity let's assume that the shielding tensor is symmetrical η=0. Then 3.1.2 formula becomes simpler:

$$\Delta\omega = -\sigma_{iso}\omega_0 - \frac{\omega_0\Delta_{CS}}{2} \times (3\cos^2\beta - 1). \qquad 3.1.6$$

The frequency shift is proportional to the isotropic and anisotropic parts. The anisotropic part is equal to zero when angle β is equal to 54.74 degrees. Therefore in order to observe only isotropic part in the spectrum the sample is needed to spin along $\boldsymbol{B}_0$ axis at frequencies larger than the interaction magnitude (fig. 3.1.3).

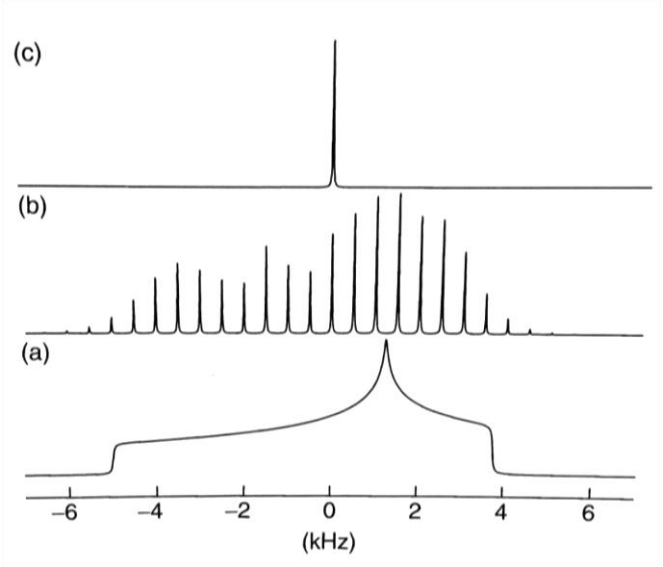

Fig. 3.1.3. The effect of MAS on a powder pattern originating from single species ($\Delta_{CS} = 5\text{kHz}, \eta = 0.5$), a) powder pattern, b) "slow spinning regime" ($\omega_{rot}/2\pi = 500\text{Hz}$), c) "fast spinning regime" ($\omega_{rot}/2\pi = 20\text{kHz}$) [28].

If the sample is spun at lower frequencies compared to the magnitude of interaction, the isotropic line becomes modulated by a spinning frequency. It is possible to visualize that the magnetization vector $\boldsymbol{M}$ after being tilted from equilibrium is rapidly dephased and rephased after one rotor period, this is the reason why during "slow spinning" regime spinning sidebands are present. Having wideline and MAS spectra, the determination of anisotropic shielding parameters could be done unambiguously.

Another widely used NMR technique is Cross polarization (CP). Theoretically it was proposed by S. R. Hartmann and E. L. Hahn in 1962 [90]. Experimentally the technique was developed by A. Pines et all and back then called Proton Enhanced Nuclear Induction Spectroscopy [91]. Due to improper abbreviation it was renamed to nowadays known CP. The main goal of this technique is sensitivity enhancement which is achieved by polarization transfer from high gyromagnetic ratio abundant spins to lower gyromagnetic ratio rare spins, in example from ^{1}H or ^{19}F to ^{13}C or ^{15}N. Moreover, polarization transfer is possible between abundant spins like ^{1}H and ^{31}P but in this case enhancement is ineffective or even the signal is weaker than those obtained from conventional pulse-acquire pulse sequence. Anyway, the CP between the abundant nuclei is very useful in physical characterization of solids materials because the polarization is transferred via dipolar coupling. Cross polarization is a coherent process which is described by the time evolution of the density operator under an effective Hamiltonian. For large spin systems, a description using thermodynamic quantities is often more appropriate and reflects the experimental observations better than a coherent description applied to a small spin system. The principle of CP is to match the nutation frequency of I and S spins to fulfil Hartmann-Hahn matching condition. It is not possible in the presence only of a static magnetic field $\boldsymbol{B}_0$. Additional B_{1I} and B_{1S} oscillating magnetic fields are needed to fulfil Hartmann-Hahn matching condition (Fig 3.1.4).

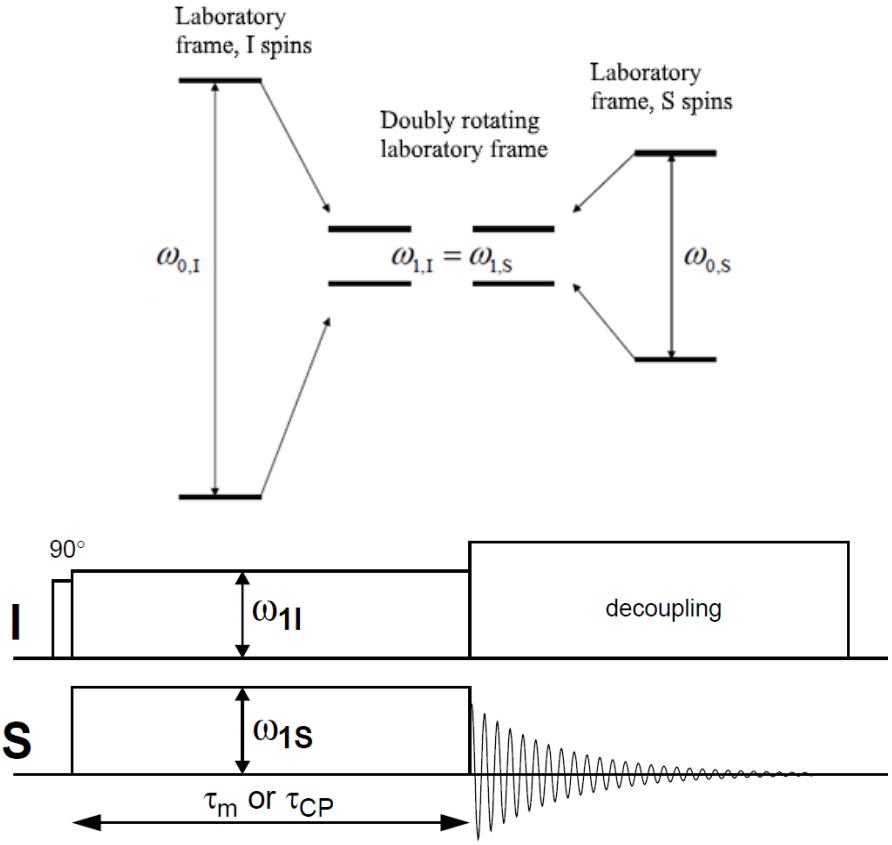

Fig. 3.1.4. Representation of doubly rotating laboratory frame for CP (top), pulse sequence for Hartmann-Hahn Cross Polarization (bottom) [92].

The pulse sequence for Hartmann-Hahn cross polarization (Fig. 3.1.4) is quite simple. After a 90° pulse on the *I* spins the magnetization is spin locked by a continuous radio-frequency field that is 90° out of phase with the initial 90° pulse. At the same time a spin-lock field on the *S* spins is applied which has an amplitude that corresponds to the same nutation frequency as the one on the *I* spins. The so-called Hartmann-Hahn condition can be written as:

$$|\omega_{1I}| = |\omega_{1S}|, \qquad 3.1.7$$

or

$$|\gamma_I B_{1I}| = |\gamma_S B_{1S}| \qquad 3.1.8$$

Under this condition, magnetization transfer is observed from the *I* spins to the *S* spins. The amount of transfer depends on the mixing time and on how well the Hartmann-Hahn condition is fulfilled. The optimal cross-polarization time τ_{CP} depends on the magnitude of the heteronuclear dipolar coupling and on the relaxation in the rotating frame $T_{1\rho}$ constants of the two spins. Typically the τ_{CP} times are of the order of milliseconds but have to be optimised experimentally for every sample. The sensitivity enhancement for a two interacting spins is equal to:

$$\xi = \frac{\gamma_I}{\gamma_S} \cdot \frac{1}{1+\varepsilon}, \qquad 3.1.9$$

$$\varepsilon = \frac{N_S}{N_I}, \qquad 3.1.10$$

where N_S and N_I correspond to the abundance of spins *S* and *I* involved in polarization transfer. Stejskal et al put forward the idea to couple CP and MAS to gain sensitivity and resolution at the same time in 1977 [93]. Despite the fact that MAS averages out the heteronuclear dipolar couplings to first-order approximation, one can combine Hartmann-Hahn polarization transfer with MAS. Under MAS the Hartmann-Hahn matching profile centred at $|\omega_{1I}| = |\omega_{1S}|$ now is split to more narrow sidebands separated by the spinning frequency ω_{rot} .

$$\omega_{1,I} = \omega_{1,S} + n\omega_{rot}, \qquad 3.1.11$$

$$n = 0, \pm 1, \pm 2, ... \qquad 3.1.12$$

Now better sensitivity and resolution is achieved at the same time. Moreover, for routine CP-MAS experiments the pulse sequence shown in figure 3.1.4 is modified by sweeping the spin-lock amplitude to fulfil several Hartmann-Hahn matching conditions. Then Hartmann-Hahn matching optimisation is not needed and an experiment is set up much faster.

Whereas the polarization transfer is transferred via the dipolar coupling the idea to collect polarization transfer kinetics on the contact time τ_{CP} seems promising because the dipolar coupling D_{IS} is $1/r^3$ proportional to the distance

between the interacting spins. Therefore structural information might be extracted. There is a nice review by Kolodziejski et.al [94] where several mechanisms for the analysis of polarization transfer are discussed. The simplest model is called classical *I*-*S* model. For simplicity it assumes that the both participating spins *I* and *S* are equal to 1/2. Thermodynamically such system might be analysed as a lattice possessing huge heat capacity and two subsystems *I* and *S* (fig. 3.2.5). The *I* subsystem has much larger heat capacity that *S*.

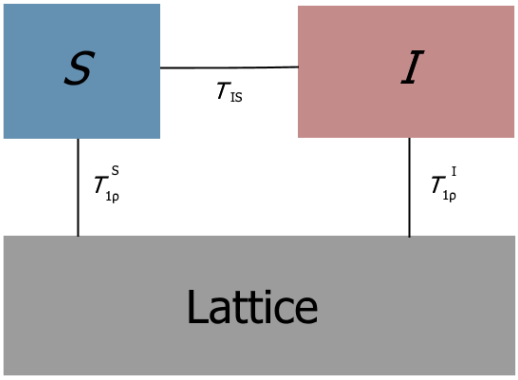

Fig. 3.1.5 Diagram of the CP thermodynamics in classical *I*-*S* model.

The system is analysed in terms of the inverse temperature β and assumed that the magnetization of *I* spins is spin locked along the $\boldsymbol{B}_{1I}$ field. During the spin lock the large $\boldsymbol{M}_{1I}$ magnetization is held by a relatively weak magnetic field $\boldsymbol{B}_{1I}$. This corresponds to a large population difference between two spin levels or to a very low spin temperature. In other words, just before the CP contact the *I* spins subsystem has a very high inverse spin temperature β_I^0. At the same moment the magnetization of spins S is equal to zero which correspond to infinite temperature or zero inverse temperature β_S^0. The Hartmann-Hahn match (3.1.11) brings both subsystems to the thermal contact and the energy/polarization transfer may occur. When the system reaches thermodynamic equilibrium the spin temperature equalizes. The hot dilute *S* spins system is cooled via thermal contact with the cold abundant spins *I* reservoir. During this thermal contact both spins systems are in contact with

the lattice through the relaxations in the rotating frame $T_{1\rho}^{I}$ and $T_{1\rho}^{S}$. The whole process during the contact time t is describe in the following way:

$$\frac{\mathrm{d}\beta_S}{\mathrm{d}t} = \frac{(\beta_S - \beta_I)}{T_{IS}} - \frac{\beta_S}{T_{1\rho}^{S}}, \tag{3.1.13}$$

$$\frac{\mathrm{d}\beta_I}{\mathrm{d}t} = -\epsilon\alpha^2 \cdot \frac{(\beta_I - \beta_S)}{T_{IS}} - \frac{\beta_I}{T_{1\rho}^{I}}, \tag{3.1.14}$$

where $T_{IS}$is the CP time constant, $\epsilon = \frac{N_S}{N_I}$ is the spin population ratio and $\alpha = \frac{\gamma_S B_{1S}}{\gamma_S B_{1I}}$ is a Hartmann-Hahn matching coefficient. After some mathematical operations taking to account that the ϵ is very small, α is equal to 1 and that inverse temperatures are proportional to the respective magnetizations or peak intensities *I*(t) it is possible to express the formula describing CP kinetics:

$$I(t) = I_0 \frac{1}{1 - \frac{T_{IS}}{T_{1\rho}^{I}}} \left[e^{-\frac{t}{T_{1\rho}^{I}}} - e^{-\frac{t}{T_{IS}}} \right]. \tag{3.1.15}$$

The above equation describes a double exponential behaviour of the CP kinetics curve consisting of fast rise of the intensity described by the T_{IS} time constant and and slow decrease which is described by the time constant $T_{1\rho}^{I}$. If the time constant $T_{1\rho}^{I}$ is much greater than 1 the CP kinetics curve reaches the plateau. The time constant T_{IS} is governed from the dipolar interactions between *I* and *S* spins. In principle T_{IS} depends on the number of nuclei participating in the CP and their internuclear distances because dipolar interaction is proportional to $1/r^3$. In other words, the more *I* spins are participating in CP the more efficient it is and the faster rise is. If CP occurs between an isolated spin pair the dipolar oscillations are present mimicking the energy transfer between a coupled pendulums which was first seen by Müller [95]. The oscillation frequency is equal to one half of the dipolar splitting *b* and is damped due to *I* spins diffusion characterized by diffusion time T_{df}. Such CP behaviour is characterized by the non-classical *I*-*I**-*S* model (Fig. 3.1.6).

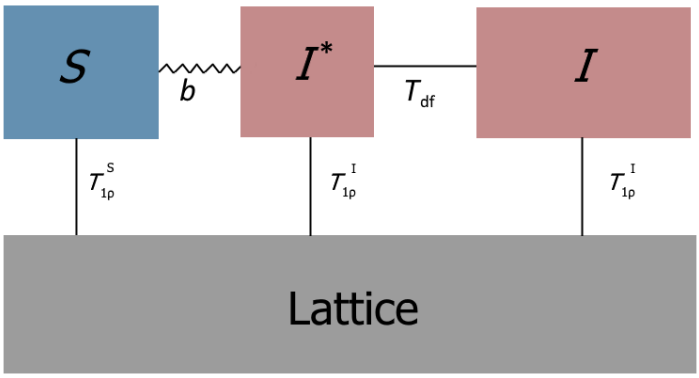

Fig. 3.1.6. Diagram of CP thermodynamics in the non-classical *I*-*I**-*S* model.

The asterisk denotes *I* spins close to the *S* spins. The *I**-*S* spins may be viewed as an isolated spin cluster wherein the polarization is transferred in an oscillatory manner which is damped by the spin-diffusion contact within the remaining *I* spins. Taking this to account the equation describing non-classical *I*-*I**-*S* model is equal:

$$I(t) = I_0 e^{-\frac{t}{T_{1\rho}^I}} \left[1 - \frac{1}{2} e^{-\frac{t}{T_{df}}} - \frac{1}{2} e^{-\frac{3}{2}\frac{t}{T_{df}}} \cdot \cos\left(\frac{bt}{2}\right) \right]. \tag{3.1.16}$$

Assuming that the sample is a rotating powder the last term in the 3.1.16 equation needs to be transformed. It is needed to calculate the mean value for all crystallites over all orientations. It was shown by the Alemany et al [96] that transient oscillations could be replaced by simple Gaussian decay:

$$\overline{\cos\left(\frac{b_i t}{2}\right)} \cong 1 - \frac{t^2}{2!T_2^2} \cong e^{-\frac{t^2}{2T_2^2}} \tag{3.1.17}$$

where the decay $1/T_2$ may be considered as a root-mean-squared average of $b_i/2$ properly weighted by the fraction $I_i / \sum_i I_i$ of molecules with a given orientation. Introducing the parameter λ describing an isolated *S*-I_n spins cluster and inserting the 3.1.17 relation into 3.1.16 the non-classical *I*-*I**-*S* CP models relation where oscillations are vanished is obtained:

$$I(t) = I_0 e^{-\frac{t}{T_{1\rho}^I}} \left[1 - \lambda e^{-\frac{t}{T_{df}}} - (1-\lambda) e^{-\frac{3}{2}\frac{t}{T_{df}}} \cdot e^{-\frac{t^2}{2T_2^2}} \right]. \tag{3.1.18}$$

The described classical *I*-*S* and both non-classical *I*-*I**-*S* CP behaviours are shown in figure 3.1.7.

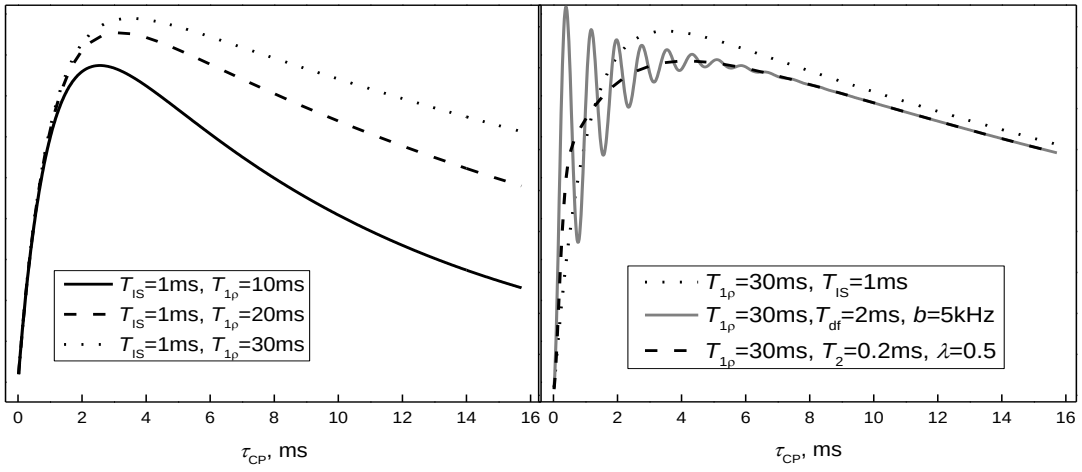

Fig. 3.1.7. Simulated CP behaviour curves. Left – classical *I*-*S* CP model (eq. 3.1.15) varying time constant $T_{1\rho}$. Right – a comparison between classical *I*-*S* (eq. 3.2.15) model (dots), the non-classical *I*-*I**-*S* (eq. 3.1.16) (dash) and non-classical *I*-*I**- *S* (eq. 3.1.18) (solid line). More details in the figure.

It is clearly seen from figure 3.1.17 that CP behaviour is highly sensitive to the time constants. This sometimes is used as a probe for studying complex materials. [27, 29, 99, 100].

4. Experimental results

Materials

The studied complex innovative materials were Calcium hydroxyapatites $Ca_{10}(PO_4)_6(OH)_2$ (CaHAps) synthesised by the aqueous sol-gel process. They were prepared by prof. habil. Dr. Aivaras Kareiva group in Vilnius University, Chemistry and Geosciences faculty, department of Inorganic chemistry. Calcium acetate monohydrate, $Ca(CH_3COO)_2 \cdot H_2O$, and ammonium–hydrogen phosphate, $(NH_4)_2HPO_4$, were selected as Ca and P sources, respectively, in Ca/P molar ratio 1.67. There were different complexing agents used, namely 1,2-ethylendiaminetetraacetic acid, $C_{10}N_2H_{16}O_8$ (EDTA), ethylene glycol, $C_2H_6O_2$ (EG), tartaric acid, $C_4H_6O_6$ (TA), or glycerol, $C_3H_8O_3$ (GL). The detailed synthesis route is published in the reference [53]. For simplicity the prepared complex materials will be further called EDTA-CaHAp, EG-CaHAp, TA-CaHAp and GL-CaHap respectively to the complexing agent used in the aqueous synthesis route. Another CaHap prepared by the same group was the one containing amorphous clustered phosphate phase (ACP) which will be named ACP-CaHAp. The synthesis route of this compound, where the glycerol, $C_3H_8O_3$ (GL), as complexing agent was used, is found in reference [60]. The last nanostructured CaHAp studied in this work was the commercial available (further CA-CaHAp) from Sigma Aldrich, synthetic, 99.999%, from metal basis. The mentioned materials were characterized by scanning electron microscopy (SEM) and energy-dispersive X-ray analysis (EDX) using a Helios NanoLab 650 scanning electron microscope coupled with energy-dispersive X-ray spectrometry system [53, 60, 111]. The corresponding XRD patterns and EM micrographs are shown in the appendix. Another compound which drops out from the mentioned above is commercial available Ammonium dihydrogen phosphate $NH_4H_2PO_4$ (ADP) from Reachem Slovakia, 99 % purity which was used as a model compound. ADP is a technologically important material because of its unique piezoelectric, ferroelectric, dielectric, and nonlinear optical properties [101]. Due to the complex variety of hydrogen bonding

(three centered or bifurcated bonds) ADP is an interesting system for fundamental studies of this type of interactions in crystals [102]. The crystallographic structure of ADP has been well examined in numerous XRD and ND experiments. Namely ND is very important because it is powerful to determine the hydrogens positions within the lattice [103-110]. As ADP lattice parameters and distances between different atoms within it are well known, this compound was chosen as a model system in one part of the dissertation.

Experimental setup

All NMR measurements were performed in Vilnius University, Physics faculty, department of General Physics and Spectroscopy using *Bruker AVANCE III HD* NMR spectrometer operating at resonance frequencies of 400 and 162 MHz for ^{1}H and ^{31}P, respectively. *Bruker Ascend 400WB* superconducting magnet which creates magnetic field of 9.4T was used. All MAS (magic angle spinning) measurements were performed using Bruker 4mm H/X CP-MAS probe-head, which is capable to spin the sample up to 15 kHz. The MAS rate varied from 0 kHz to 10 kHz depending on the experiment (it is marked in figures and text). All NMR measurements were done at 298K temperature. The ^{1}H spectra were measured using *zgbs* pulse sequence which supresses the background artefacts and experimental settings were following: 64 scans, 90^{o} pulse duration was 2.5 μs, repetition delay was 10 s. ^{31}P Bloch decay (BD) spectra were performed using *hpdec* pulse sequence using high power decoupling during FID collection, 90^{o} pulse duration was 1.8 μs, repetition delay was 10 s and 16 scans were accumulated. ^{1}H–^{31}P CP spectra were measured employing rectangular contact time pulse in order to fulfil only one Hartmann-Hahn matching condition (3.2.11), number of scans was 4/2, repetition delay was of 15/2 s respectively for CaHaps and ADP samples. For ^{1}H–^{31}P HETCOR experiments *lghetfq* pulse sequence was used with subsequent parameters: 16 scans, 256 increments, short 500 μs contact time pulse and 15s of repetition delay. Before measuring CP kinetics for any specimen at any MAS spinning frequency the *HH* matching profiles were obtained to validate the correct radio-frequency (RF) fields for ^{1}H and ^{31}P (Figure 4.2.1) which varied depending on the sample, MAS frequency, *HH* matching condition and were 50 – 100 kHz. There were 498 contact time increments collected which varied from 50 μs to 10 ms for every CaHAp CP kinetics curve under MAS condition. For ADP CP kinetics there were 996 contact time increments collected which varied from 50 μs to 10 ms. NMR spectra were processed using built in the spectrometer software *Topsin 3.2*.

Additionally the signal shapes and CP kinetic curves were processed using the Levenberg - Marquardt method implemented in *Microcal Origin* 9 and *Mathcad* 15 packages [112, 113].

4.1. ^{1}H, ^{31}P 1D NMR results

Firstly, the newly synthesised complex innovative CaHAp samples were analysed by means of XRD and EM spectroscopy [53, 60]. The XRD analysis have revealed that all CaHAp's were composed of principal apatite crystalline phase. EDX study proved that additional calcium and phosphorous containing phases which are not detectable by XRD are present in the CaHAp samples (see the appendix). In such case NMR spectroscopy is the method of choice to detect and analyse nearly invisible differences at the nano/mezo scale in similar complex materials.

The complex CaHAp samples were analysed by means of ^{1}H and ^{31}P NMR spectroscopy methods. From the first glance all CaHAp samples except ACP-CaHAp possessed similar spectral features. For this reason TA-CaHAp and ACP-CaHAp samples were used as references to determine the effect of MAS on the spectral linewidth and the effectiveness of MAS. The MAS technique fails to suppress anisotropic spin interactions fully if intensive reorientational dynamics is present [114, 115]. This cause the different MAS effect on the ^{31}P interaction with protons in the structural hydroxyl groups and adsorbed water. The effect of MAS is indeed much less pronounced on the ^{31}P NMR spectra of ACP-CaHAp. The signal is narrowing from ~ 4000 Hz (static sample) to 940 Hz (MAS, at 5 - 10 kHz spinning, Fig. 4.1.1). In the spectra of TA-CaHAp the observed signal narrowing is very significant – from 2540 Hz (static sample) to the width of 150 - 67 Hz that depends on the spinning rate (MAS, 1 - 8 kHz, Fig. 4.1.1).

In the presence of reorientational motion the rotor-synchronized MAS linewidth ($\Delta\nu_{1/2}$) becomes dependent on the strength of anisotropic spin interactions, such as dipolar coupling, chemical shift anisotropy, etc (the term of the magnitude of the inhomogeneous anisotropic broadening (ν_{an}) will be used hereinafter), the kinetics (represented by the rate constant k) and the spinning rate (ν_{MAS}) [115].

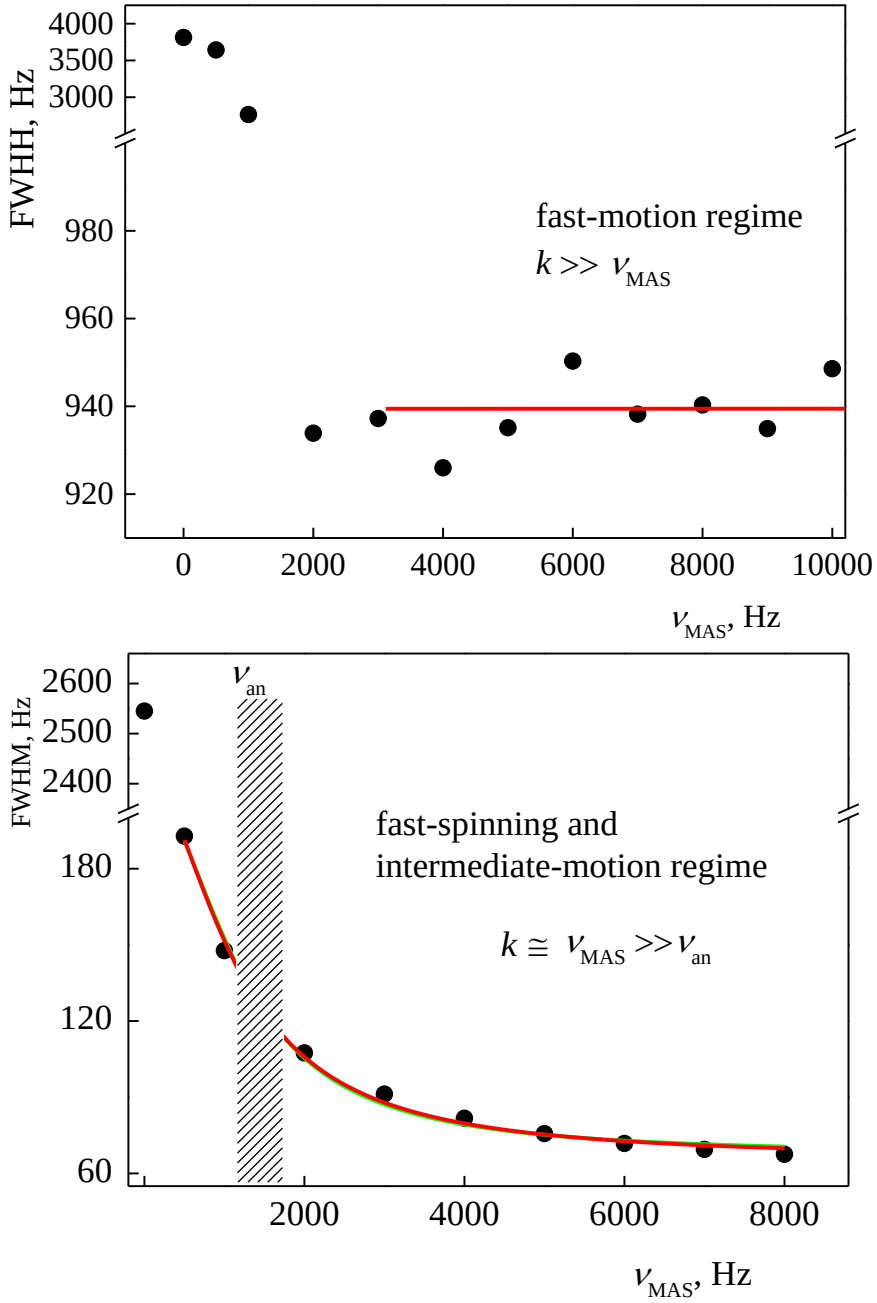

Fig. 4.1.1 Effect of MAS rate on the ^{31}P NMR linewidth for ACP-CaHAp (upper) and nano-structured EG-CaHAp (lower).

In the fast-spinning regime the linewidth $\Delta\nu_{1/2}$ can be expressed as:

$$\Delta\nu_{1/2} = \frac{\pi\nu_{an}^2}{2\nu_{MAS}(16\pi^2+x^2)^2}[-16\pi^2(e^{-x}-1-x)+x^2(e^{-x}-1+x)], \quad (4.1.1)$$

where $x = k/\nu_{MAS}$. In the regime close to maximal broadening ($2\pi\ \nu_{MAS}/k \approx 0.55$) this equation can be simplified:

$$\Delta\nu_{1/2} = \frac{k\pi\nu_{an}^2}{2k^2+32\pi^2\nu_{MAS}^2}. \quad (4.1.2)$$

Both equations have been used analysing the effect of MAS rate on the ^{31}P NMR linewidth for ACP-CaHAp and nano-structured TA-CaHAp (Fig. 4.1.2). Some distinguishing features have to be noted. The signal width of ACP-CaHAp sample drops steeply down as ν_{MAS} oversteps ~ 1 kHz and becomes to be independent on the spinning rate up to 10 kHz (Fig. 4.1.1). This can occur if, $k >> 4\pi\nu_{MAS}$ (Eq 4.1.2). It means that the fast spin motion takes place in ACP-CaHA. The situation in the nano-structured TA-CaHAp is quite different. The signal width is drastically narrowed already at rather slow spinning (ν_{MAS} ~ 500 Hz, Fig. 4.1.1). The linewidth in the MAS range 0.5 - 8 kHz becomes dependent on the spinning rate (Fig. 4.1.1). This dependency has been processed using Eq 4.1.1 and Eq 4.1.2. However, both equations are valid in the fast-spinning regime, when ν_{MAS} is large compared with ν_{an} [115]. Therefore the fitting was repeated for several experimental data sets composed increasing the minimal value of the spinning rate $(\nu_{MAS})_{min}$ (Fig. 4.2.2). The values of the magnitude of the inhomogeneous anisotropic broadening (ν_{an}) as well as the rate constant (k) have been determined with the least errors processing. The identical coincidence between experimental points and theoretical curves (solid lines, Fig. 4.1.1) has been achieved for the data set that starts at $(\nu_{MAS})_{min}$ = 2 kHz (Fig 4.1.2). Hence, the fast-spinning regime ($\nu_{MAS} > \nu_{an}$) for nano-structured TA-CaHAp is fulfilled at the spinning rates above ~ 2 kHz. The rate constant k ~ 30 000 s^{-1} (Fig. 4.1.2) means that the spin dynamics is much slower than in ACP-CaHAp.

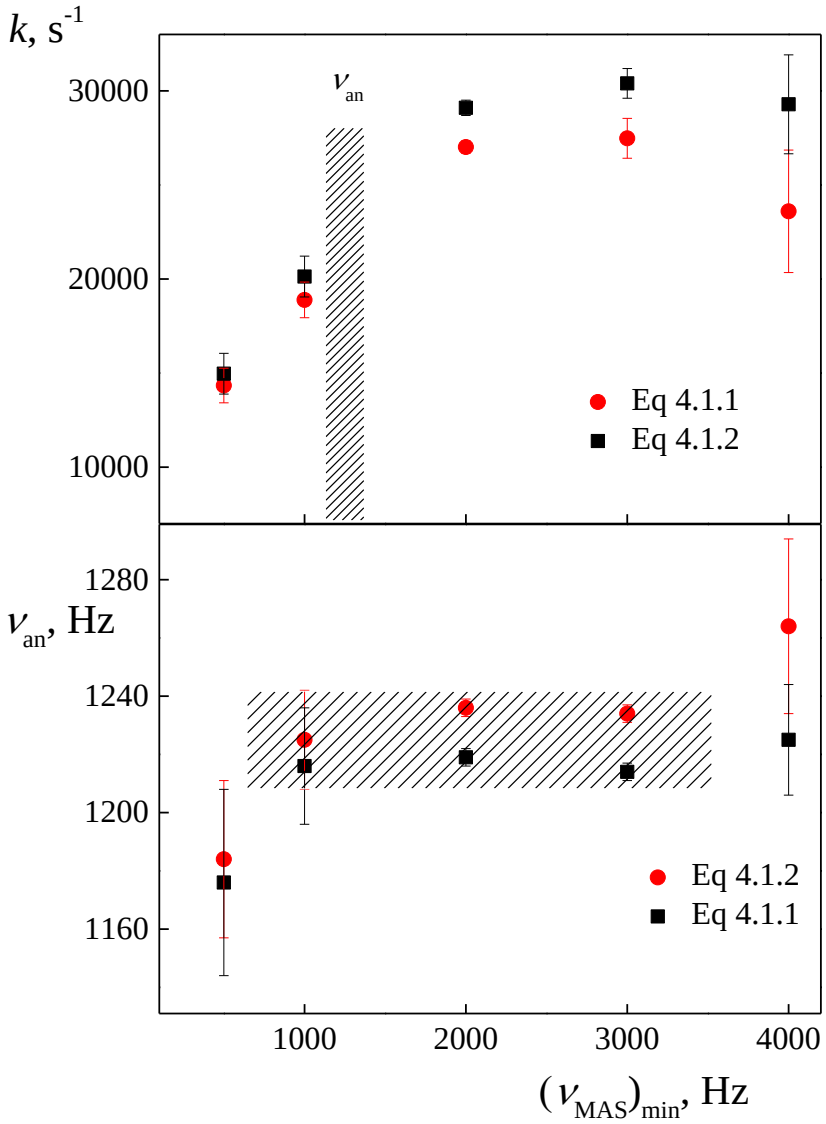

Fig. 4.1.2.The magnitude of the inhomogeneous anisotropic broadening (ν_{an}) and the rate constant (k) determined processing the experimental data sets composed increasing the minimal of the spinning rate $(\nu_{MAS})_{min}$ for nano-structured TA-CaHAp.

4.1.1. ^{1}H NMR Results

In order to obtain results without any undesirable anisotropic line broadening 10 kHz of MAS spinning is used in further analysis. The complexity of these materials lies in the manifold of the structures in nano and meso scale, namely in the ratio of surface and bulk species. Recently Osman et al published a study on the surface and bulk structures in crystalline hydroxyapatite nanoparticles [26]. Their proposed spectral line assignment is shown in Table 4.1.1

Table 4.1.1 ^{1}H and ^{31}P NMR spectral lines assignments in nano-crystaline CaHAp discriminating surface species and the bulk [26].

	δ, ppm		Assignment and (comments)
bulk	^{1}H	^{31}P	
		2.90	PO_4
	0.1		OH_{UP}
	-0.13		OH_{DOWN}
	3.1	4.8	HPO_4
	+2-7	+2-6	Disordered HPO_4 due to defects to ideal HAp structure (broad line)
	5.1		Physi/chemisorbed H2O
surface		6.3	PO_4
	8-13	3-7	H_xPO_4 (broad line)
	-0.01		OH_{SURF} (not fully resolved)
	1.3		H_2O_{UP} (structured)
	0.8		H_2O_{DOWN} (structured)
	1.1		Structured stacking H_2O (split into 1.3/0.8 ppm contributions at low water content)
	5.1		Physi/chemisorbed H_2O

^{1}H NMR spectroscopy revealed that all nanostructured samples, namely EDTA/EG/TA/GL/CA-CaHAps possess spectra which consist of a sharp peak at approximately 0 ppm and much broader one at 5.1 ppm which is attributed to chemi/physisorbed water (Fig 4.1.3.). In TA/GL-CaHAps a shoulder at -0.75 ppm of the OH spectral line is observed which is not resolved fully but might be the outcome of the defects within the HAp structure or some protonated bulk/surface phosphate group. It is rather complicated to separate the spectral line attributed to the disordered HPO_4 due to defects of HAp crystal structure and/or the surface H_xPO_4 species, however these lines not necessary are present. Even drying the samples in the inert atmosphere to extract the moisture from the powders may not enable to detect these species because water could be trapped within the HAp structures, for example, in the pores or encapsulated in the cavities. There are low intensity but rather sharp peaks visible in the region of 0.5 – 2 ppm.

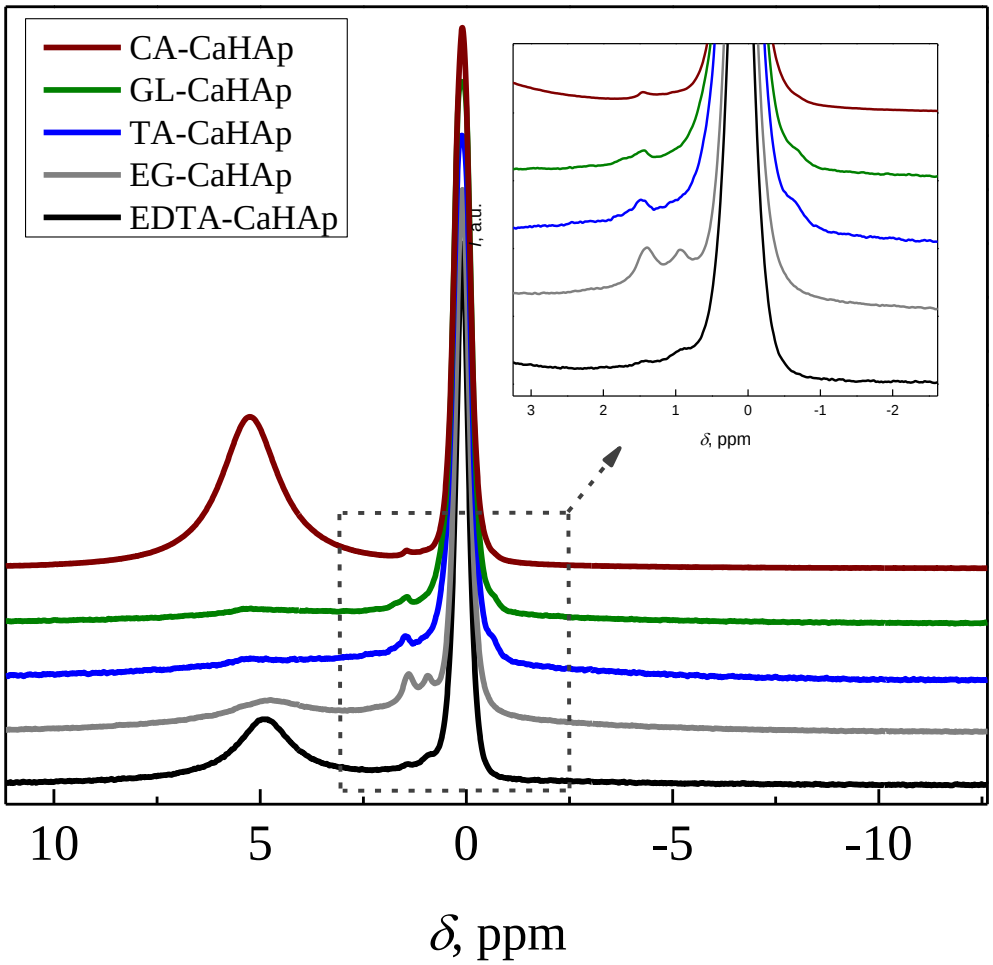

Fig. 4.1.3. ^{1}H 10 kHz MAS EDTA/DCTA/EG/GL/CA-CaHAps NMR spectra. An expansion of spectral region of -2 – 3 ppm (Right top). More details in the graph.

These spectral lines belong to the surface adsorbed water [26]. It is known that water chemical shift is highly dependent on the structure and bonding of water molecules, in other words, it is possible to discern monomeric, dimeric, etc. species [116-118]. It is possible to observe two peaks of monomeric water species specified as H_2O_{UP} and H_2O_{DOWN} according to the OH configuration on the surface of HAp structures at low water content (Table 4.1.1). Two peaks are visible in EDTA/EG-CaHAps while only one in TA/GL/CA-CaHAps. Such behaviour might be related to the different amount of water within the samples. To analyse this phenomenon one sample, namely CA-CaHAp was chosen as target. After measuring ^{1}H MAS spectrum of the sample the rotor was opened and placed in the vacuum chamber (vacuum of 10^{-2} mbar) for 24 hours at

100˚C to extract the moisture. Immediately after the procedure it was closed with Kel-F rotor cap to prevent from moisture from air and ^{1}H MAS spectrum was measured. Later on a drop of water was added with a micropipette and additional spectrum was measured (Fig. 4.1.4).

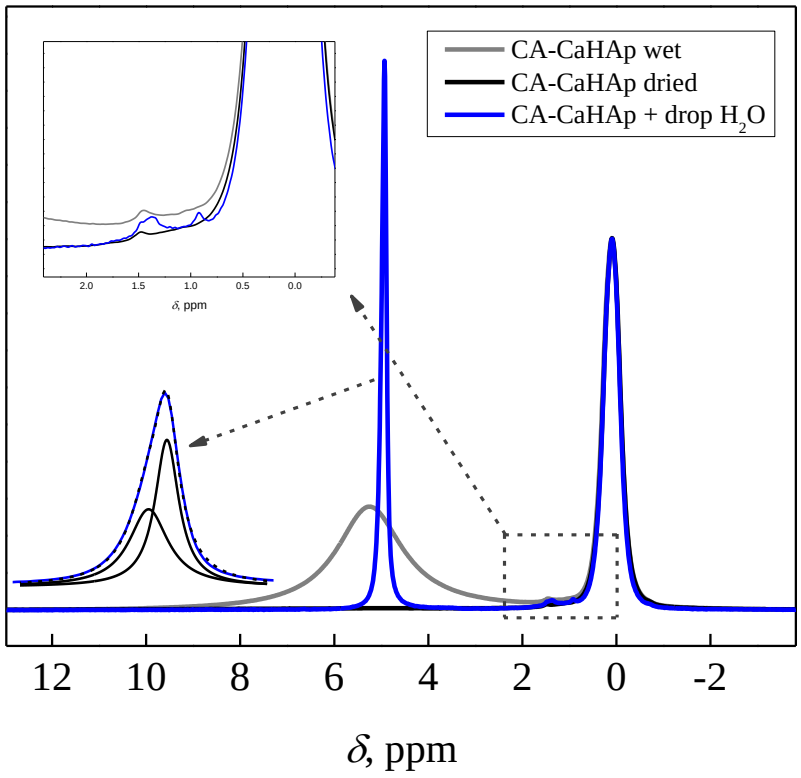

Fig. 4.1.4. ^{1}H 10 kHz MAS CA-CaHAp spectra depending on the water content. More details in the graph.

It is clearly seen that drying in the vacuum helps to extract physi/chemisorbed water and surface water from the sample. What is more, at low water content the structural H_2O_{UP} and H_2O_{DOWN} lines split into two while in the wet sample only one is present. It is important to point out that after small amount of water was introduced the spectral line attributed to physi/chemisorbed water shifted to lower chemical shift values compared to wet sample. Moreover, the FWHM decreases 14 times from 698 Hz to 49 Hz and the peak becomes composed from two Lorentz shaped components (Fig. 4.1.4). The water spectral line in wet sample is broadened because fast exchange processes are present. Most probably, two components appears from the surface and the bulk water. It is very important and interesting to analyse the water filling phenomenon in the

HAp structures. Although it is not analysed more in details here but as mentioned in ref. 26 the process is rather sophisticated and needs to be investigated - this is the goal for future projects. While the spectral features in the nano-structured CaHAps are rather similar the ACP-CaHAp which consists from amorphous clustered phosphate phase possesses completely different spectral lines (Fig. 4.1.5 lower right). There were observed peaks at 12.2/5.5/5.1 ppm which were assigned to surface H_xPO_4/ bulk disordered HPO_4/ chemi/physisorbed water respectively. Besides that, some low intensity sharp peaks at a region specific for structural H_2O_{UP} and H_2O_{DOWN} were observed. The signal at 0.0 ppm is not seen in ^1H NMR spectrum and thus it can be supposed that the amount of structural hydroxyl groups is practically negligible or they are even absent. However this can be not true. The molecules of adsorbed water possess much higher degree of motional freedom. If the adsorbed water is present in the sample in enough large amount the ^1H peak of the structural –OH can be significantly broadened and averaged with water signal due to fast exchange processes. And indeed, FTIR spectroscopy data confirm the presence of structural –OH groups in ACP-CaHAp [119]. Whereas ^1H spectral lines are very different between ACP-CaHAp and other nano-structured HAps it is complicated to compare structures between them quantitatively. Nevertheless, it is possible to characterise nano-structured CaHAps by their sharp O-H line analysis (Fig 4.1.5). In all of the nano-structured CaHAps the OH line consists of several Lorentz shaped peaks. In TA/GL-CaHAps the effect is mostly pronounced (Fig 4.1.5 middle). What is more, there are three spectral lines, namely at 0.1/-0.13/-0.01 attributed to $OH_{UP}/OH_{DOWN}/OH_{SURF}$ respectively [26]. Thanks to the proper instrumental setting ^1H MAS spectra of high data point density (50 points/ppm) were measured which allowed to perform Lorentz function fit unambiguously. Such high data point density reduces excess degrees of freedom in the non-linear signal contours fitting procedure targeting its flow towards the 'true' (global) minimum on the multi-parameter surface χ^2, i.e. the sum of weighted squares

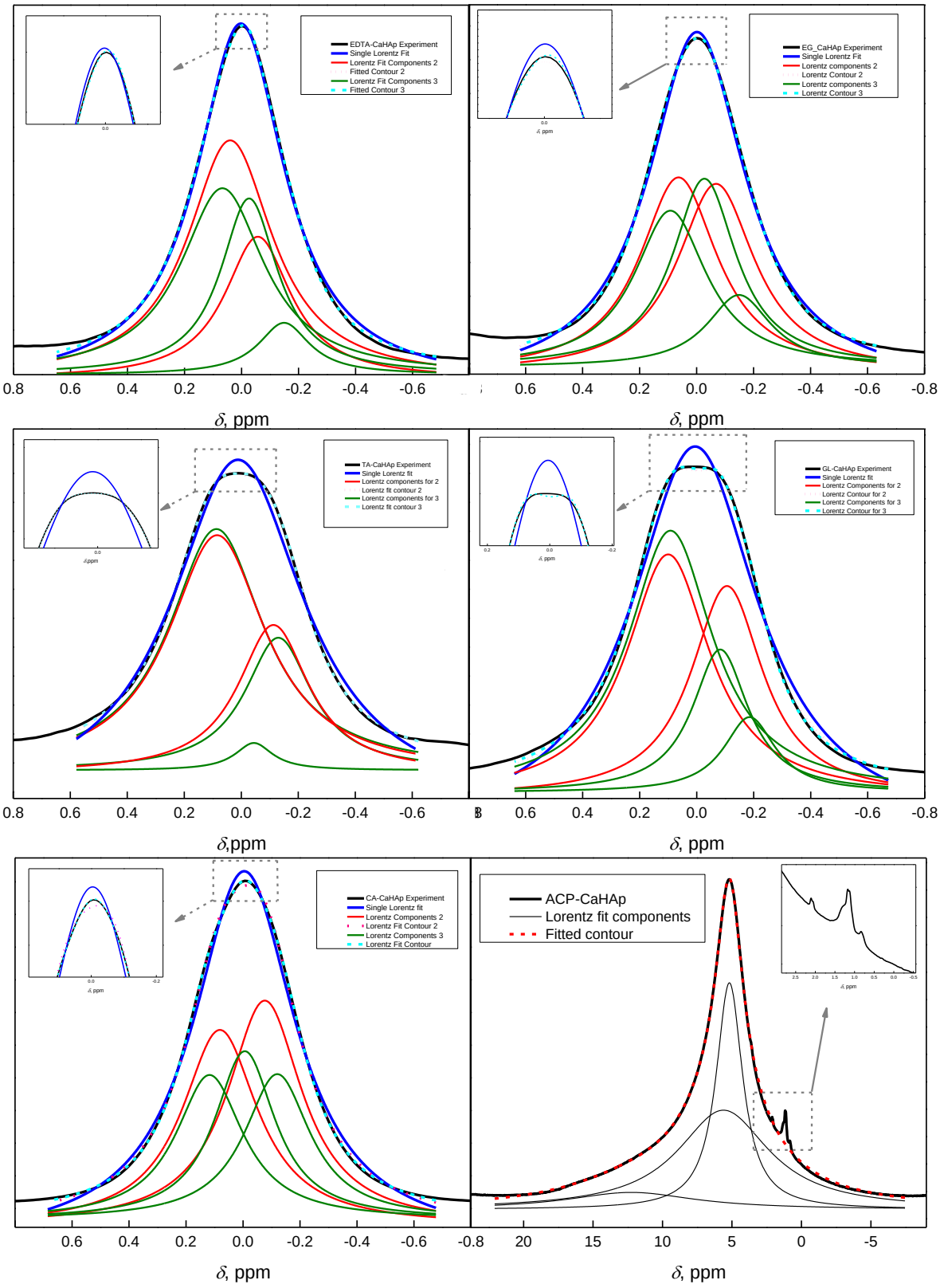

Fig. 4.1.5. ^{1}H 10 kHz MAS NMR spectra including theoretical fittings. More comments in the graphs and text.

of deviations of the chosen theoretical model curve from the experimental points. It makes possible more rigorous decision concerning the validity of the hypothetic models (signal shapes) and more fitting parameters can be used and determined unambiguously. There were three approximations performed consisting of single, double and triple Lorentz contours. Even approximation using a single Lorentz function produced a perfect fit with the correlation coefficient R^2=0.99. However, some at the first glance not apparent systematic (non-random) deviations persist on the top of the OH line contours (Fig. 4.1.5). Only the increase of a Lorentz shaped components number to three eliminated these deviations. To corroborate this choice it is important to note that in Ref. 26 was proved that OH line consists of three overlapped peaks (Table 4.1.1). The summarised data showing chemical shift and integral intensity value for OH_{UP}, OH_{SURF} and OH_{DOWN} spectral lines is shown in the table 4.1.2.

Table 4.1.2. Lorentz fitting parameters, more details in the text.

	OH_{UP}		OH_{SURF}		OH_{DOWN}			
	δ, ppm	A, a.u.	δ, ppm	A, a.u.	δ, ppm	A, a.u.	$A_{OH_{SURF}}/_{OH\ BULK}$	$A_{OH_{UP}}/A_{OH_{DOWN}}$
ED TA	0.06 ±0.02	0.31	-0.02 ±0.01	0.20	-0.15 ±0.02	0.05	0.55	5.9
EG	0.09 ±0.01	0.23	-0.03 ±0.01	0.25	-0.15 ±0.02	0.09	0.75	2.45
TA	0.09± 0.01	0.53	-0.02 ±0.01	0.02	-0.13 ±0.01	0.20	0.03	2.58
GL	0.09 ±0.01	0.46	-0.08 ±0.01	0.17	-0.18 ±0.01	0.08	0.31	5.7
CA	0.12 ±0.01	0.20	-0.01 ±0.01	0.21	-0.12 ±0.01	0.20	0.53	1.01

It is clearly seen that the chemical shift values obtained after fitting procedure coincide with the ones showed in table 4.1.1 with great accuracy. Only one sample, namely GL-CaHAp drops out a bit. Whereas, the integral intensities of OH_{UP}, OH_{SURF} and OH_{DOWN} lines are obtained parameters $A_{OH_{SURF}}/_{OH\ BULK}$ and $A_{OH_{UP}}/A_{OH_{DOWN}}$ showing the organization of the OH structural groups are

introduced. In the CA-CaHAp the ratio of the $A_{OH_{UP}}/A_{OH_{DOWN}}$ is equal to 1.01 which means that there are nearly the same amount of OH_{UP} and OH_{DOWN} species and according to the fit there are twice times less of the surface species. In other CaHAps, namely EDTA/EG/TA-CaHAps the situation is different, by changing the complexing agent in the aqueous sol-gel synthesis route it is possible to control the amount of OH_{UP} and OH_{DOWN} species ratio within the HAp structure. What is more, the amount surface and bulk species is as well dependent on the complexing agent used, in other words, the nano-structural aspects are controlled. Certainly, this phenomenon should be investigated more, there should be more synthesis routes performed applying different complexing agents and different their ratio to create the target synthesis protocol for these complex innovative CaHAp based materials.

4.1.2. ^{31}P NMR Results

Solid-state ^{31}P NMR spectra and the signal shape analysis are often exploited in the studies of some closely related systems [26, 71-75]. The narrow Lorentz-shaped peak at maximum around 3 ppm and the full widths at half maximum ($\Delta\nu_{1/2}$) of 109 Hz was registered in the synthetic crystalline HAp whereas that from mesoporous bioactive glass was Gauss-shaped and an order of magnitude broader (1020 Hz) [72]. A single ^{31}P signal centered at 2.3 ppm is also displayed in fluoroapatite (FAp) gelatin nano-composite [74]. This signal was attributed to PO_4^{3-} groups in crystalline FAp. Its $\Delta\nu_{1/2}$ of 178 Hz is typical for that of pure HAp and deviates significantly from that observed in HAp-based nano-composite prepared by direct precipitation in solution (373 Hz). The broadening of the latter was explained by the presence of an amorphous calcium phosphate (CaP) phase located at the surfaces or at grain boundaries of the HA nano-platelets [74]. The signal at 2.6 ppm is dominating in ^{31}P MAS NMR spectra of CaP and gel/CaP, similarly to pure HA [71]. Therefore this peak was also attributed to PO_4^{3-} groups. However the signal shapes in both CaP and gel/CaP are asymmetric and significantly broader, demonstrating

structural inhomogeneities, which can include the presence of an additional phase different from pure crystalline HA. The linewidths were found to be increased from 243 to 373 Hz when gelatin was introduced into the mineral matrix [71]. Note for several systems it was succeeded to decompose the observed ^{31}P signal into 2-3 spectral components [26, 70, 71, 74, 75]. These components have been attributed to bulk PO_4^{3-} (2.5 - 3.2 ppm), surface unprotonated PO_4^{3-} (4.4 - 6.0 ppm) and to protonated bulk/surface HPO_4^{2-} groups (0.45 - 1.3 ppm), respectively [74, 75].

The studied nano-structured EDTA/EG/TA/GL/CA-CaHAps showed similar features as the synthetic crystalline HAp or FAp [72, 74], ^{31}P MAS NMR signals were found being Voigt-shaped and the FWHM were between 56-81 Hz, while the ACP-CaHAp signal was Gauss shaped and the FWHM was 974 Hz similar to the HAp produced from mesoporous bioactive glass [72]. The Voigt profile is the convolution of Gauss (G) and Lorentz (L) functions, i.e. $V = G * L$. In the NMR studies of structuring effects it can be assumed that the presence of various non-uniformities (short-range disorder, heterogeneities, etc) in nano- and mesoscopic scales enhances the Gauss contribution to the Voigt-shaped signals, whereas the Lorentz contribution is originated from the uniform spin interactions and dynamics. The corresponding spectral lines are showed in Fig 4.1.6. There were pulse-acquire Bloch decay (BD) and Cross-Polarization with ramped contact time (CP) pulse sequences employed for all speciments. The reasoning for such choice is that by combining those two it is possible to separate the protonated and non-protonated phosphate groups as in the CP the signal is obtained via the polarization transfer from ^{1}H nuclei. It is clearly seen that in all of the BD spectra of nano-structured CaHAps (Fig. 4.1.6. black line) the spectral contour consists of a broad component and one or more much sharper ones. The broad component being Voigt shaped having a considerable Gauss function contribution shows its non-uniform origin. Moreover, in CP spectra it disappears or decrease significantly which means that it arises from an unprotonated PO_4^{3-} group.

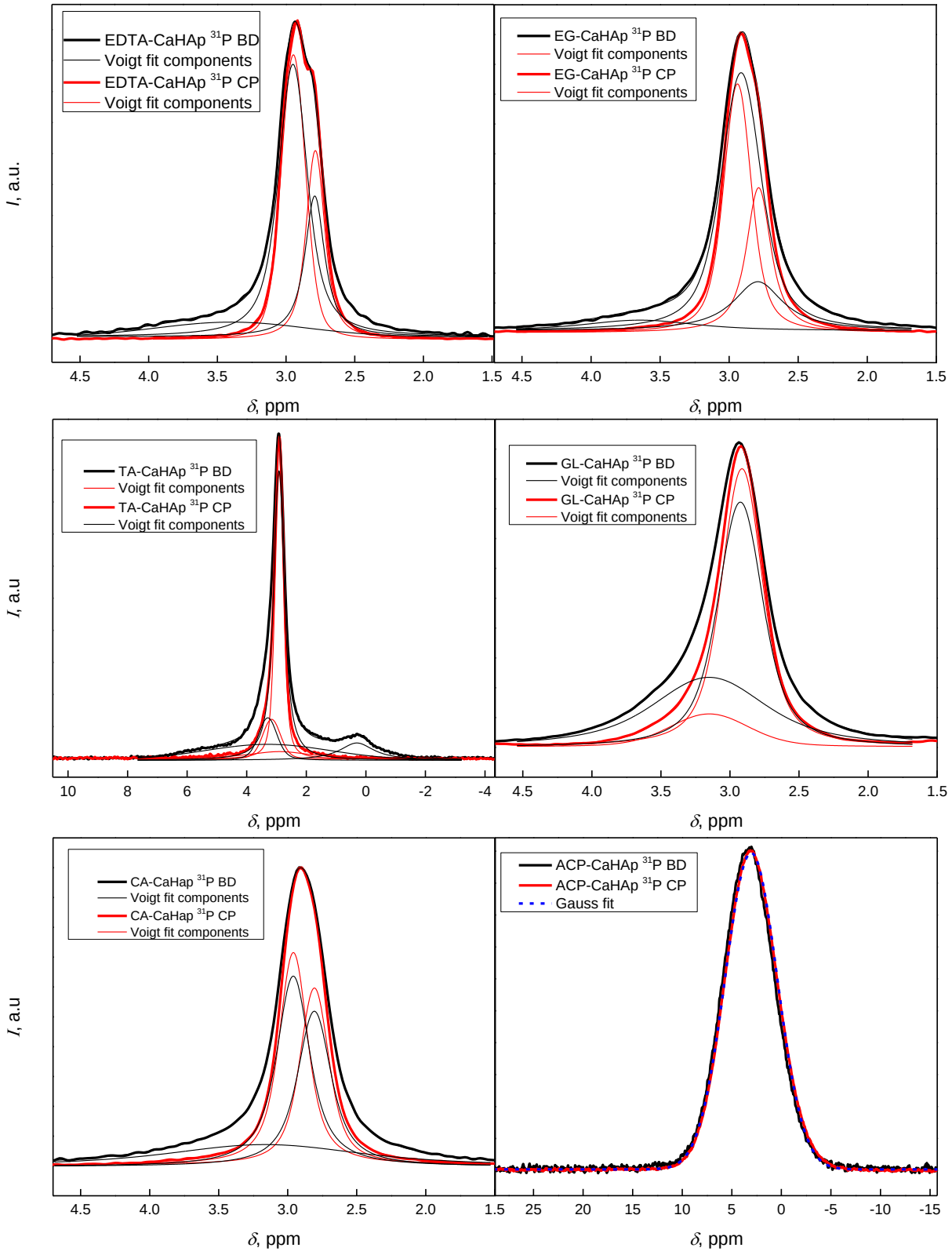

Fig. 4.1.6. ^{31}P BD (black line) and CP (red line) spectra of EDTA/EG/TA/GL/CA/ACP-CaHAps together with Voigt shaped contours fit.

Also the chemical shift values were similar to closely related systems [74]. The narrow peaks originated from bulk PO_4 groups in nano-structured CaHAps seems to be not affected much on the CP. They are found to be Voigt shaped with essential Lorentz contribution. Furthermore, in EDTA/EG/CA-CaHAps the peak consist of two components comparable in intensity while only one major is present in TA/GL- CaHAps. The ratio of the integral intensities of the corresponding peaks are 0.6/0.6/0.8 respectively to ETDA/EG/CA-CaHAps. Such behaviour is not clear yet but two spectral lines might be the consequence of different chemical environment within the HAp based nano/meso-structures. Rather intense peak observed in TA-CaHAp at 0.33 ppm and a shoulder positioning at 6-3 ppm could be attributed to tricalcium phosphate ($Ca_3(PO_4)_2$, TCP) side phase because they are not observed in the CP spectrum (Fig 4.1.7.) [120]. Moreover, such side phase was observed in XRD pattern (see the Appendix).

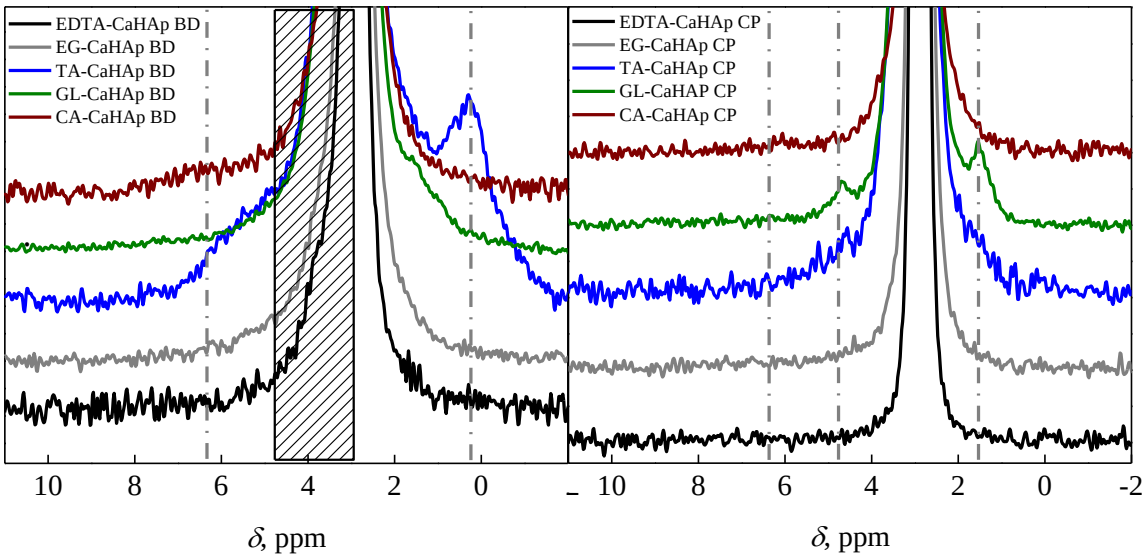

Fig. 4.1.7. ^{31}P BD (left) and CP (right) magnified wing part spectra of EDTA/EG/TA/GL/CA-CaHAps.

In the GL-CaHAp CP spectra two peaks at 4.8 ppm and 1.5 ppm are observed which comes from the bulk disordered HPO_4 or surface H_xPO_4 and protonated HPO_4^{2-} groups respectively [26, 75]. The same tendency but much less expressed is seen in TA-CaHAp. Such behaviour corroborates to ^1H spectra

where only in TA/GL-CaHAps a peak at 0.75 ppm is observed which is not fully resolved (Fig. 4.1.3.), there is a big chance that peak comes from the protonated phosphate groups. A very broad and virtually invisible spectral line at 6.3 pmm which is assigned to the surface PO_4 group is detected in the CA-CaHAp though in other samples it is overlapped with a stronger ones or missing. Nevertheless, having such weak intensity proper implications could not be done. Summing up ^{1}H and ^{31}P NMR spectroscopy is a valuable and powerful tool to investigate the nano-structured materials at a molecular level.

Conclusions of part 4.1

- The effect of MAS rate on the ^{31}P linewidth was studied which proved the optimal of 5 kHz spinning. The magnitude of the inhomogeneous anisotropic broadening of 1220±20Hz for nano-structured CaHAp was determined.

- A precise ^{1}H and ^{31}P MAS NMR spectra analysis was performed which allowed to assign spectral lines for the manifolds of the possible surface species and the bulk in the EDTA/EG/TA/GL/CA/ACP-CaHAps.

- The precise analysis of water spectral line in the CA-CaHAp showed NMR capability to analyse the water organisation within cavities and pores in the nano-structures.

- The contour separation of the spectral line at 0 ppm showed the different organization of the manifold of the structural hydroxyl groups in the EDTA/EG/TA/GL/CA-CaHAps.

- A precise analysis of ^{31}P CP and BD spectra allowed to resolve a side phase of the bulk disordered HPO_4 or surface H_xPO_4 or protonated HPO_4^{2-} groups in GL-CaHAp and TCP side phase in the TA-CaHAp.

4.2. Advanced methods to analyse proximities of nuclear ^{1}H – ^{31}P spins clusters.

The idea to obtain structural information from variable contact time CP kinetics is not new. There are several approaches and theoretical considerations describing the polarization transfer. They were discussed in chapters 2.2 and 3.1. There were variable contact time measurements prepared for all of the samples discussed in chapter 4.1 the results will be discussed in chapter 4.3. In this chapter the modification in the present CP kinetics models will be discussed.

4.2.1. Cut – off averaging of Gaussian distribution.

There will CP behaviour for TA-CaHap (further in this chapter nano-CaHAp) and ACP-CaHap analysed. The reason for such choice is nano-CaHAp possessed only one major spectral line in the CP spectrum and ACP-CaHAp contains amorphous clustered phosphate phase (Fig 4.1.6). For the samples a precise *Hartmann-Hahn* matching profiles we obtained by changing the ^{1}H power for rectangular contact pulse in order fulfil only one matching condition (eqs 3.1.11 and 3.1.12) as the dipolar splitting is dependent on it (Fig. 4.2.1) [27]. As mentioned in the chapter *Experimental Setup* the variable ^{1}H–^{31}P contact time experiments included 498 contact time increments increased by 50 μs which corresponds to the sampling frequency of $5 \cdot 10^{4}$ s^{-1}. According to the Nyquist's theorem this setting allows to reveal all spin interactions having the dipolar splitting $b \leq 25$ kHz. It means that in the case of ^{1}H–^{31}P interaction the structures with the spin distances $r \geq 0.125$ nm could be resolved (4.2.2). Having high data point density in the CP kinetics contour reduces excess degrees of freedom in the non-linear signal contours fitting procedure targeting its flow towards the 'true' (global) minimum on the multi-parameter surface χ^2, i.e. the sum of weighted squares of deviations of the chosen theoretical model curve from the experimental points. It makes possible more rigorous decision

concerning the validity of the hypothetic models (signal shapes) and more fitting parameters can be used and determined unambiguously.

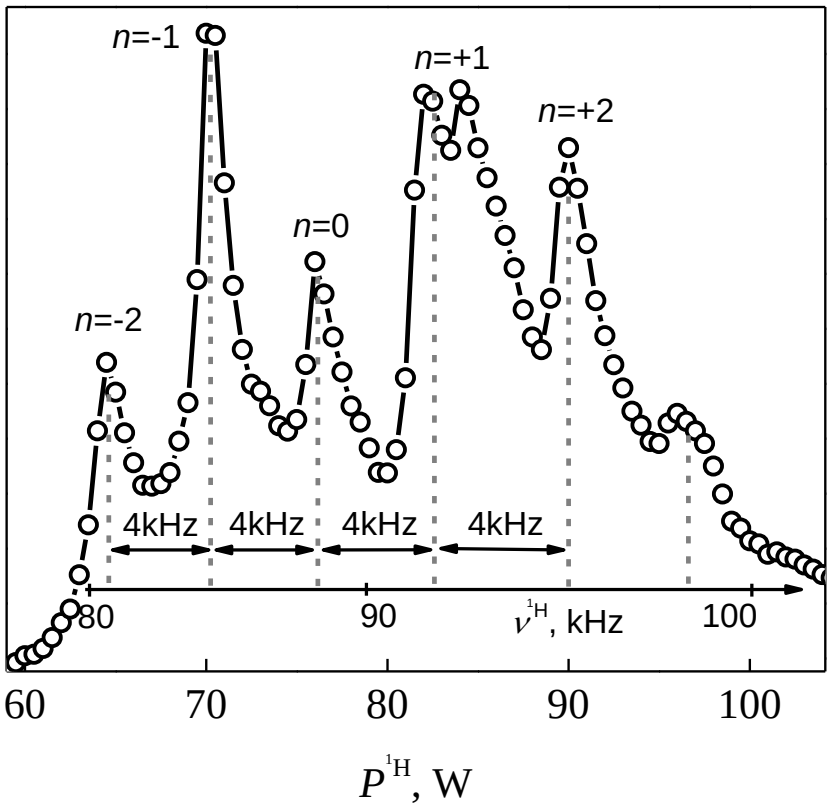

Fig. 4.2.1. Hartmann-Hahn matching profile for nano-CaHAp (ν_{MAS}=4kHz). Open circles – integrated intensity versus ^{1}H contact pulse power (lower scale) and nutation frequency $\nu = {}^{1}/_{4\tau_{90}}$(upper scale). Numbers *n* indicate matching conditions.

The CP kinetics in ACP-CaHAp (Figure 4.2.2 upper) looks very similar to that observed in polycrystalline brushite and some other related systems [94]. This curve consists of three characteristic parts – fast rise, slow rise and decay. The CP kinetics observed in the nano-structured CaHAp exhibit the damped oscillation of intensity in the short contact time range (Figure 4.2.2 lower). As the oscillations of CP intensity have been observed for the first time in ^{1}H -^{13}C CP experiments on single crystals [95, 121]. There was deduced that the frequency of oscillation depends on the orientation of the crystal in the external magnetic field and it is equal to one-half of the dipolar splitting (*b*). Later on, such oscillations have been found for many other systems, including powders,

bilayers and other complex structured solids [94 and references therein]. The oscillatory CP kinetics for an isolated pair of spins 1/2 can described by the equation 3.2.16.

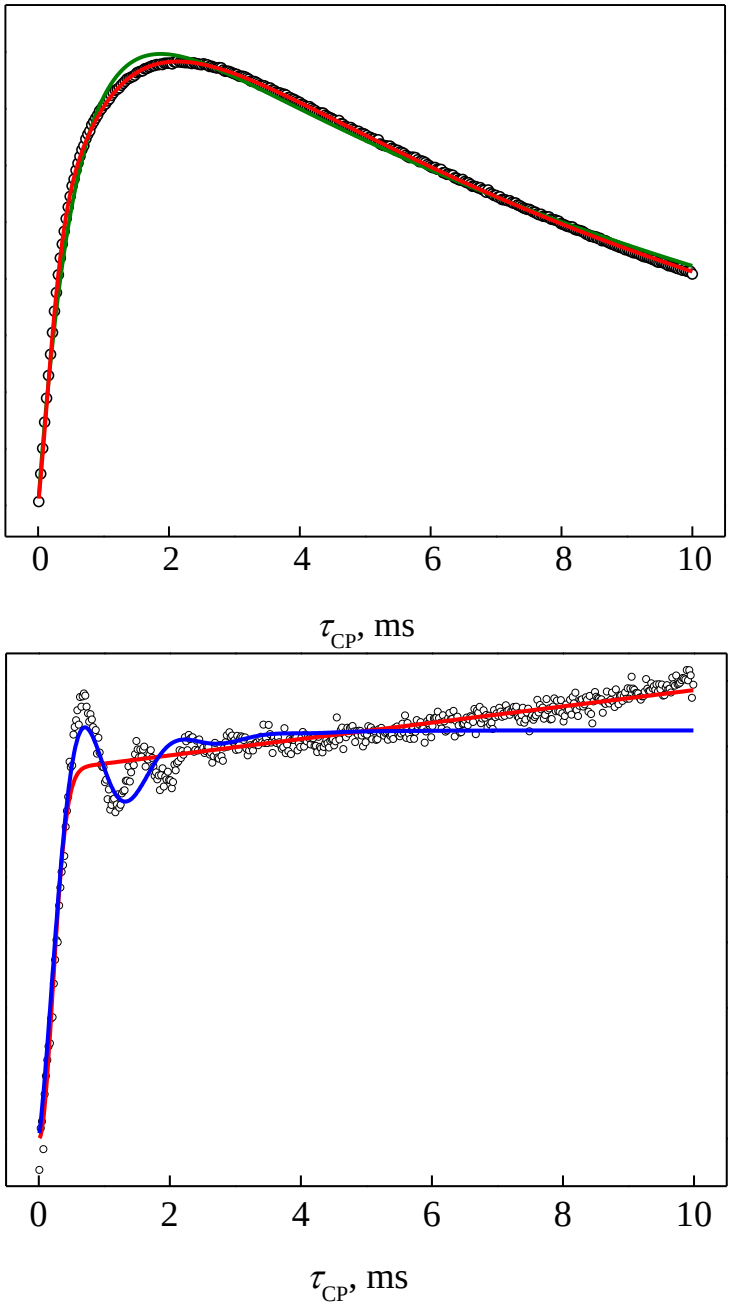

Fig. 4.2.2. ^{1}H -^{31}P CP MAS kinetics (integrated central ^{31}P signal intensities *vs*. variable contact time) in ACP-CaHAp (upper) and in nano-CaHAp (lower). The fitting for ACP-CaHAp was carried out using eq 3.1.18 (red line) and the classical *I-S* model of CP dynamics between two abundant nuclei eq 3.1.15 (green line). The fitting for nano-structured CaHAp was carried out using eq 3.1.16 (blue line) and eq 3.1.18 (red line). The obtained fitting parameters are presented in Table 4.2.1. More comments in the text.

The obtained CP kinetics profiles were analysed by the methods described in the section 3.1., namely the classical *I–S* CP model (eq. 3.2.15) and the non-classical *I-I***-S* ones having the oscillating term (eq. 3.2.16) and the T_2 averaged model (eq. 3.2.18).

Table 4.2.1. Fit data for CP MAS-kinetics in ACP-CaHAp and nano-CaHAp (Figure 4.2.2).

Hydroxyapatite containing amorphous phosphate phase (ACP-CaHAp)					
Model: non-classical *I-I***-S*, eq 3.1.18, R^2 = 0.9997			Model: classical *I-S*, modified eq 3.1.15*, R^2 = 0.993		
Parameter	Value	Standard error	Parameter	Value	Standard error
I_0, a.u.	$2.092\cdot10^{11}$	$2.67\cdot10^{8}$	I_0, a.u.	$2.26\cdot10^{11}$	--
λ	0.698	0.003	T_{is}, s	$7.84\cdot10^{-4}$	$1.212\cdot10^{-5}$
T_{dif}, s	0.00102	$6.83\cdot10^{-6}$	$T_{1\rho}^{I}$, s	0.0089	$1.499\cdot10^{-4}$
$T_{1\rho}$, s	0.01075	$2.162\cdot10^{-5}$	$T_{1\rho}^{S}$, s	∞	--
T_2, s	$2.38\cdot10^{-4}$	$1.98\cdot10^{-6}$	$\varepsilon\alpha^2$	0.22986	0.00605
			I_{00}, a.u.	$6.238\cdot10^{9}$	$1.083\cdot10^{9}$
Nano-structured hydroxyapatite (nano-CaHAp)					
Model: non-classical *I-I***-S*, eq 3.1.18, R^2 = 0.940			Model: non-classical *I-I***-S*, eq 3.1.16 R^2 = 0.950		
Parameter	Value	Standard error	Parameter	Value	Standard error
I_0, a.u.	$2.333\cdot10^{11}$	--	I_0, a.u.	$1.249\cdot10^{10}$	--
λ	0.952	$2.06\cdot10^{-4}$	λ	0.402	0.007
T_{dif}, s	0.884	0.02877	T_{dif}, s	0.001	$1.94717\cdot10^{-5}$
T_2, s	$2.099\cdot10^{-4}$	$3.553\cdot10^{-6}$	*b*, Hz	1365.648	16.79
$T_{1\rho}$, s	∞	--	$T_{1\rho}$, s	∞	--

*) modified eq 3.1.15 including Hartmann-Hahn matching coefficient and spin population factor according to ref 94.

The obtained fitting parameters for ACP/nano-CaHAps are summarised in table 4.2.1. The eqs 3.1.16 and 3.1.18 describe the kinetics of CP in the frame of so called non-classical I-I^*-S model, where the asterisk denotes protons in close neighbourhood to S spins (^{31}P in the present case) [94]. The I^*-S spin pairs or clusters exchange polarization in an oscillatory manner. The oscillations are damped by the subsequent spin-diffusion. This model has been proposed in addition to the more popular classical I-S model, where it is assumed that spin-diffusion is fast enough to force spins to behave as a system at a uniform inverse spin temperature [94, 122]. Comparing both models it is seen that I-I^*-S model is appropriate when the heteronuclear I^*-S spin interactions are strong compared with homonuclear I-I ones. In the case of weak I-S and moderate or strong I-I couplings the CP kinetics is better described using the classical I-S model [94]. Eq 3.1.18 was successfully applied processing the CP kinetic curves of various complex systems. A nice fit to experimental points sampled over a wide range contact time (up to ~ 20 ms) was achieved in many cases [94, 122]. Also for ACP-CaHAp eq 3.1.18 perfectly (R^2 = 0.9997) fits to the experimental points of CP kinetics over the whole contact time range up to 10 ms (Fig. 4.2.2.). In addition, this experimental curve was tried to fit using the classical I-S model (eq 3.1.15) of CP dynamics between two abundant nuclei. A nice coincidence with experiment (R^2 = 0.993) and quite realistic values of the fit parameters have been obtained using this model as well (see Table 4.2.1). However some systematic (non-random) deviations are noticeable in the middle part of curve, i.e. at slow rise (1 - 3 ms), and in the decay part at 8 - 10 ms (Figure 4.2.2) despite more fitting parameters were included. This systematic discrepancies were possible to be revealed only thanks to the high experimental point density. Hence it can be concluded that I-I^*-S model is more preferable to describe the CP kinetics in ACP-CaHAp.

The oscillation of intensity is well expressed in the CP kinetic curve of the nano-CaHAp (Figure 4.2.2). Unfortunately, it was not succeeded to describe the observed kinetics by eq 3.1.16 or 3.1.18 over the whole contact time range.

The initial part of the curve up to ~ 5 ms can be more or less approached by eq 3.1.16 reproducing the oscillation. The fit value b = 1366 ± 17 Hz (see Table 4.1.1) is close to those determined for some synthetic hydroxyapatites doped with carbonate and magnesium ions [75]. Nevertheless, the curve does not reach plateau at the contact time above ~ 5 ms. Such behaviour differs from the kinetics observed there. The discrepancy between experimental and calculated (eq 3.2.16) values diverges getting into the range of longer contact times (Figure 4.2.2). Though the situation looks opposite trying to fit the data using eq 3.1.18. The good fit was achieved over the whole range of contact time, but the oscillation was lost. This occurs as the averaging by summing over a broad spectrum of b values (eq 3.1.17) yields destructive interference that blurs the oscillation pattern. It is undeniable that the new treatment of CP kinetics is required which would be an intermediate to the existing *I*-*I**-*S* models described by relations 3.1.16 and 3.1.18 in order to describe the CP kinetics in the nano-structured systems over a wide dynamic (contact time) range.

This can be done noticing that the summing of the weighted cosine values (eq 3.1.17) can considered as discrete cos-Fourier transform of function $I(b/2)$ from b- to t-domain:

$$\frac{\sum_i I\left(\frac{b_i}{2}\right)\cos\left(\frac{2\pi b_i t}{2}\right)}{\sum_i I\left(\frac{b_i}{2}\right)} \rightarrow \frac{1}{A}\sum_i^{\infty} I\left(\frac{b_i}{2}\right)\cos\left(2\pi\frac{b_i}{2}t\right) = \frac{1}{A}\mathrm{Re}\widehat{\mathrm{FT}}\left\{I\left(\frac{b}{2}\right)\right\}, \quad (4.2.1)$$

where $A = \sum_i I(b_i/2)$ is the normalizing factor. The summing can be formally extended to infinity prolonging $I(b/2)$ by the proper zero-filing.

The ^{31}P NMR signal being perfectly Gauss- or Voigt-shaped with essential Gauss contribution clarifies why the 3.1.18 relation so perfectly describes the experimental points sampled over very wide range of contact time though the averaging described by equation 3.1.17 has been derived in the short time limit [96]. As the Fourier transform of Gauss function produces the Gauss function, the relation (eq 3.1.18) and thus the eq 3.1.18 must be valid in the cases of Gauss-shaped $I(b/2)$ without any limitation in time. To support this, ^{31}P wideline spectra were measured of the corresponding samples (Fig. 4.2.3).

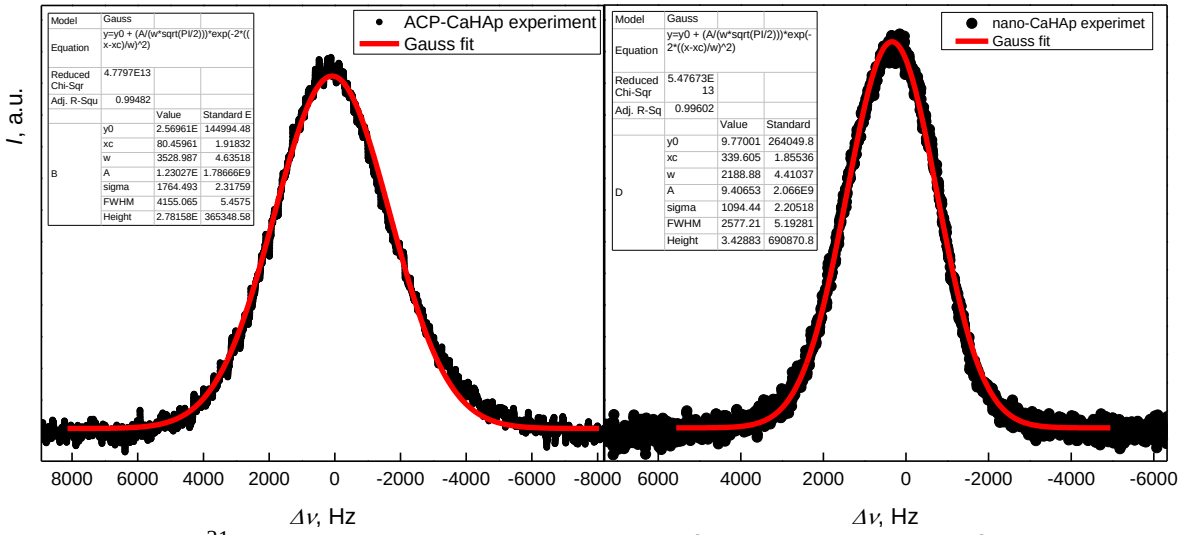

Fig. 4.2.3. ^{31}P BD wideline spectra acquired for ACP-CaHAp (left) and nano-CaHap (right), black dots – experimental points, red line – Gauss fit. Fitting parameters shown in the graphs.

Strictly speaking a powder pattern should be observed (Fig. 3.1.2) but it seems either the CSA is small or the broadening is determined by the dipole-dipole interaction in much greater magnitude. Therefore, a Gauss function fit was performed for both contours. If the signal shape is mainly determined by the dipole-dipole interactions, the full widths at half maximum (FWHM) obtained by fitting of ^{31}P signal shape by Gauss function and T_2 (Table 4.2.1) that follows from the processing of CP kinetic curve using the averaged *I*-I^*-*S* CP kinetics model should obey the relation FWHM·T_2= 0.375 (the case of exact Gauss functions). These parameter were found to be 4155 Hz/2577Hz and $8.8\cdot10^{-5}$ s/ $1.4\cdot10^{-4}$ s for ACP-CaHAp and nano-CaHAp respectively. Namely, FWHM·$T_2 \approx 0.36$ was found to be almost the same for both samples.

Due to spatial structural discontinuities in nano-structured materials the dipole coupling distribution $I(b/2)$ can be rather complex. Its shape cannot be known at the beginning. To determine $I(b/2)$ correctly the Gauss decay (eq 3.1.17) in eq 3.1.18 was replaced by Fourier image (eq 4.2.1) and an inverse Fourier transform from *t*- to *b*-domain performed:

$$I(b/2) \sim \left|\widehat{\mathrm{FT}}^{-1}\frac{1-\lambda f_1-I(t)/(I_0 f_3)}{(1-\lambda)f_2}\right|, \qquad (4.2.2)$$

where $f_1 = \exp(-t/T_{dif})$, $f_2 = \exp(-1.5t/T_{dif})$ and $f_3 = \exp(-t/T_{1\rho})$. In order to apply such trick the values of I_0, λ, T_{dif} and $T_{1\rho}$ have to be known. At the first approach the necessary parameters can be taken from the set of fit parameters obtained using T_2 averaged I-I^*-S model (Table 4.2.1). This equation describes the CP kinetics over the whole range of contact time, only the oscillations are blurred (Figure 4.2.2). By using this fit the most accurate parameters of the relation 4.2.2 are obtained. Later these values can be refined.

The experimental data of ACP/nano-CaHAp was processed using the above described method (Fig. 4.2.4). A distinct difference between $I(b)$ of both samples is that the for the nano-CaHAp a pake-like patern having pakes centered at ~ ±1.5 kHz is observed, whereas the monotonic Gauss shaped decay is observed for ACP-CaHAp.

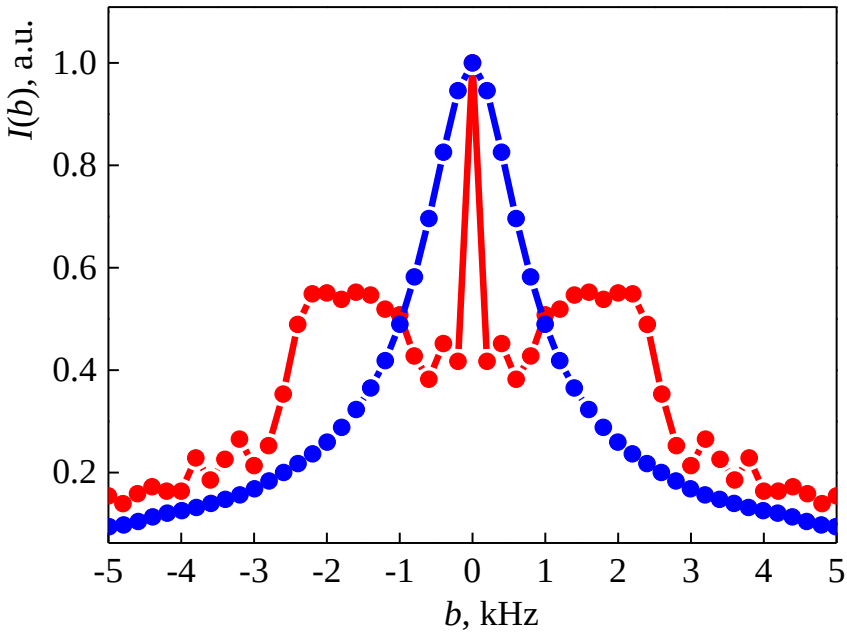

Fig. 4.2.4. Dipole-dipole coupling distribution *I(b)* in ACP-CaHAp –blue dots and nano-CaHAp – red dots.

The most convenient choice is to approximate the top part of the broad band is the Gauss function $G(b_i) = \exp(-(b_i - b_0)^2/2w^2)$ with the adjustable parameters b_0 and w. However its 'long tails' have to be cut off at the certain b values (Fig 4.2.5). For this purpose the parameter $\Delta b_{\text{cut-off}}$ was introduced. It is easy to

realize that $\Delta b_{\text{cut-off}}$ value is characteristic for each nano-structured system and must be also optimized during the CP kinetic curve fitting:

$$I(t) = I_0 e^{-t/T_{1\rho}} \left[1 - \lambda e^{-\frac{t}{T_{dif}}} - (1-\lambda) e^{-\frac{3t}{2T_{dif}}} \frac{\sum_i^{\Delta b_{\text{cut-off}}} G(b_i) \cos(2\pi b_i t/2)}{\sum_i^{\Delta b_{\text{cut-off}}} G(b_i)} \right].$$

(4.2.3)

This relation can be considered as an intermediate one to equations 3.1.16 and 3.1.18: asymptotically if $G(b) \rightarrow \delta(b - b_0)$ it becomes 3.1.16 and one becomes eq 3.1.18, if $G(b)$ is pure Gauss function.

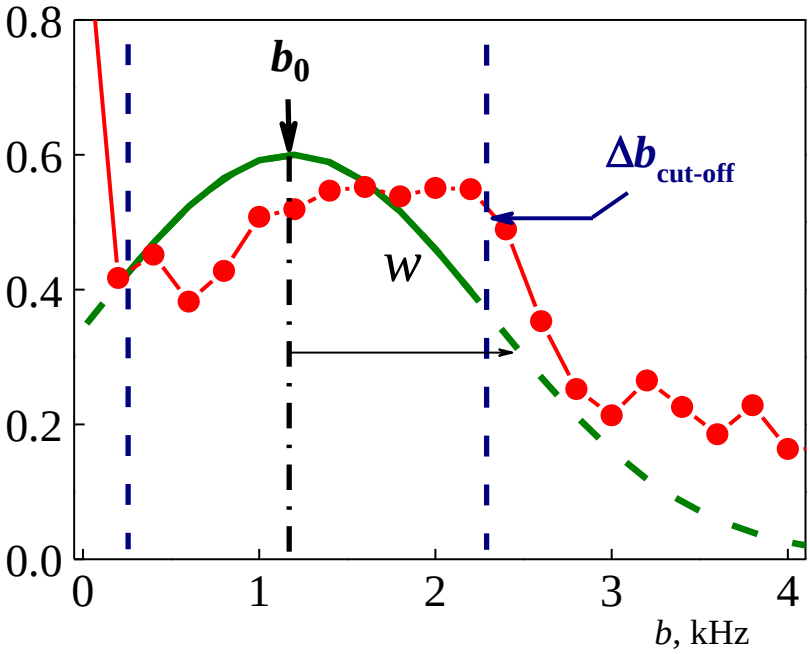

Fig. 4.2.5. Cut-off averaging of dipole-dipole coupling distribution in nano-CaHAp. Red dots – experiment, green line – theoretical Gauss function. More comments in the text.

The fitting of CP kinetics in the nano-structured CaHAp using cut-off averaging Gauss distribution approach with the whole set of parameters has been carried out (Fig 4.2.6). This fitting refines the values of the parameters that initially were taken from the set obtained using averaged Gaussian distribution for dipole-dipole coupling (Eq 3.1.18), which, unfortunately, does not reproduce the oscillation part in the CP kinetics. Much better fit and more

realistic vales of the used parameters have been obtained. For example, the spin-diffusion time constant T_{dif} = 0.88 s (eq 3.1.18) (Table 4.2.1) drops to 7.6 ms. This value gets into the same time scale deduced for the related nanocrystalline HAps [75, 79]. Moreover, the infinitely long $T_{1\rho}$ came out even without the presence of plateau in the kinetics curve.

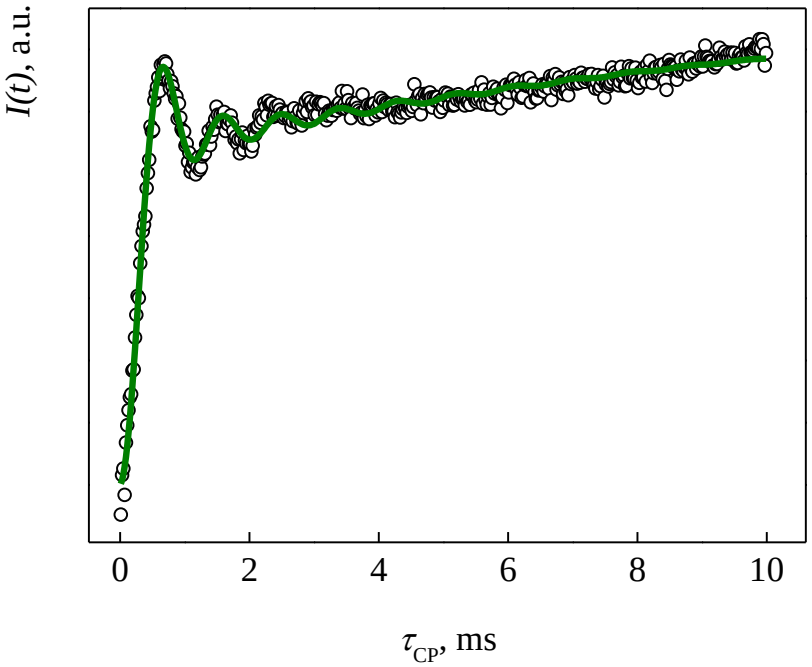

Fig. 4.2.6. ^{1}H–^{31}P CP MAS kinetics in the nano-CaHAp. The fitting was carried out using the complete set of parameters and 4.2.3 equation. The fit parameters values are: $\Delta b_{\text{cut-off}}$ = 2050 Hz, b_0 = 1185 Hz, w = 1115 Hz, I_0 = $1.5 \cdot 10^{10}$, λ = 0.348, T_{dif} = 7.6 ms, $T_{1\rho} \rightarrow \infty$. The value of R^2 = 0.989 was achieved.

The λ value has been changed also significantly. According to ref. 94, the parameter $\lambda = 1/(n+1)$ for rigid structures, where n is the number of protons in the spin cluster interacting with ^{31}P nucleus in the HAp structure. Using the refined value of λ = 0.348 the number of protons can be evaluated n = 1.87, which is lower than that would follow from the general formula ($Ca_{10}(PO_4)_6(OH)_2$). This can be caused by the discussed above different MAS effect on the ^{31}P interaction with protons in the structural hydroxyls and adsorbed water.

The λ value was determined using the *b*-averaged CP kinetics (eq 4.2.3). The major contribution in the averaging comes from $I(b)$ at b_0 = 1185 Hz within $\Delta b_{\text{cut-off}}$ = 2050 Hz (Figure 4.2.6). This part of $I(b)$ is mainly contributed from incompletely averaged dipolar couplings, i.e. from ^{31}P interactions with more mobile protons.

The MAS technique fails to suppress anisotropic spin interactions fully if intensive reorientational dynamics is present [115]. The interactions of ^{31}P spins with the protons in structural hydroxyl groups, i.e. more tightly bonded to phosphorus, are essentially averaged by MAS. It contributes the increase of the peak in the distribution $I(b)$ at b = 0. The molecules of adsorbed water possess much higher degree of motional freedom. In the presence of reorientational motion the MAS line shape and width become dependent on the spin interaction strength, the time scale of the motion and the spinning rate [115]. This effect was noticed and mentioned in chapter 4.1 discussing about the optimal MAS rate. Hence, despite the λ value was optimized, it is still likely that λ can be considered only as a certain qualitative (not quantitative) parameter that can be useful comparing the cluster composition in series of related systems.

The obtained dipole coupling distribution (Figure 4.2.5) can be used deducing some structural aspects of the studied systems. If the dipolar coupling constants are known the inter-nuclear distances can be calculated from the oscillations frequencies:

$$b = \frac{\mu_0}{4\pi}\frac{\gamma_I\gamma_S\hbar}{r^3}\frac{\left(1-3\cos^2\theta\right)}{2} = D_{\text{IS}}\frac{\left(1-3\cos^2\theta\right)}{2}, \qquad (4.2.4)$$

where μ_0 is the magnetic constant, γ_I, γ_S corresponding magnetogyric ratios, r internuclear distance at the orientation θ in the magnetic field. In the case of isolated spin pairs the magnitude of the coupling constant is directly deduced from the Pake-like pattern obtained by Fourier transform of the oscillatory polarization transfer [80]. For a powder sample under MAS the dipolar coupling (4.2.4) becomes dependant on the *HH* matching condition [80,123]:

$$b_0 = \frac{D_{\text{IS}}}{2}(1-3\cos^2\theta)\frac{\left(3cos^2\beta-1\right)}{2} \to 0,$$

$$b_{\pm 1} = \frac{D_{IS}}{2\sqrt{2}} \sin 2\beta \exp(\pm i\gamma), \qquad (4.2.5)$$

$$b_{\pm 2} = \frac{D_{IS}}{4} \sin^2\beta \exp(\pm i2\gamma),$$

where indexes below b shows sideband matching condition (present case n=±2), β and γ are the polar angles of r vector respect to MAS rotor-fixed coordinate system with z axis along the spinning axis. The maximum splitting that corresponds to $\beta = \pi/2$ is the half of the splitting between the intense singularities in a Pake pattern [80]. In presence of nano-structuring effects the Pake-like pattern is partially blurred due to disorder in the internuclear distances. The complex-shaped contour $I(b)$ which was found for nano-CaHAp (Figs. 4.2.4 and 4.2.5) can be considered as the envelope of the superposition of Pake singularities from the pairs of spins having different internuclear distances. The obtained dipole coupling distribution allows to determine the characteristic size profile of the spin clusters in ACP-CaHAp and in nano-CaHAp (Fig 4.2.7). For this experimental dataset an equation 4.2.5 which corresponds to the second matching condition was used.

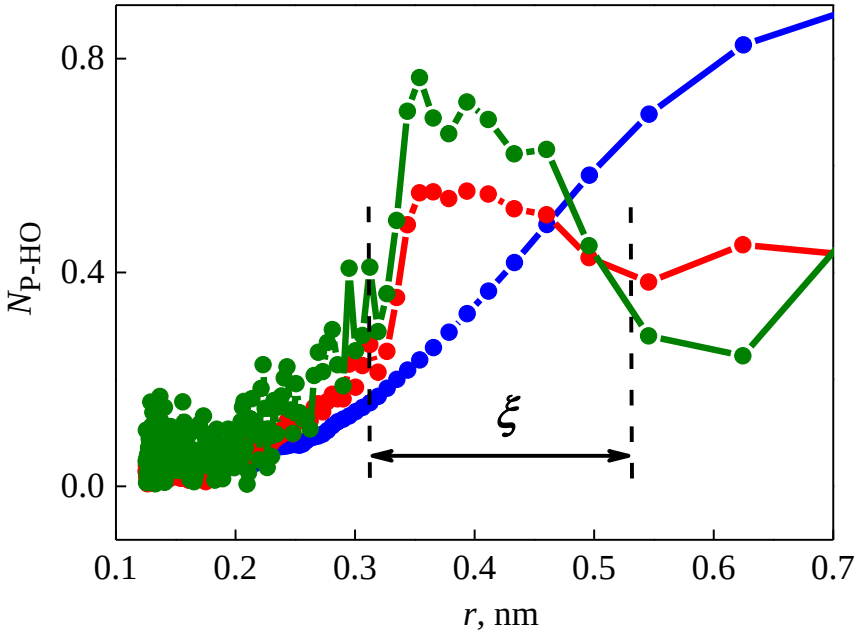

Fig. 4.2.7. Spatial distribution of protons surround ^{31}P nuclei in ACP-CaHAp (blue) and nano-CaHAp (red – obtained using the first approach parameter values, green – using the refined values). The characteristic size of ^{31}P–(^{1}H)$_n$ spin nano-cluster is denoted as ξ.

The characteristic size of $^{31}P–(^{1}H)_n$ spin nano-cluster being within ξ = 0.3÷0.5 nm has been determined for the nano-CaHAp. It should be noted that the size profile is not crucially influenced by the refinement of the parameters I_0, λ, T_{dif} and $T_{1\rho}$ (Fig 4.2.7). It is also rather interesting that the initial slope of CP dynamics in biomimetic hydroxyapatite - gelatin nanocomposites was well described using the average $^{31}P–^{1}H$ distance of 0.53 nm (concerning that two protons are ~ 0.4 nm apart and four other are at ~ 0.6 nm) [124].

4.2.2. Radial distribution approach

In chapter 4.2.1 an approach which employs of cut-off averaging Gaussian spin coupling distribution in order to describe CP dynamics in the whole measured range for nano-CaHAp (Fig 4.2.6) was introduced. The reasoning for such choice was rather logic, the lineshapes in ^{31}P NMR spectra were found being in many cases Gauss- or Voigt-shaped with substantial Gauss contribution. Though the question if only the cut-off Gaussian dipolar coupling profile approximation is eligible for such HAp systems is still open. For this reason two samples, namely ACP-CaHAp and CA-HAp (further in this chapter nano-CaHAp) will be discussed more in details. There will be shown other possible distribution profiles for describing dipolar coupling. Moreover, the effect of spin diffusion will be analysed.

The CP kinetics in the ACP/nano-CaHaps were measured using the same experimental settings used in Chapter 4.2.1 and described in chapter Experimental setup. The corresponding CP kinetics are shown in figure 4.2.8. In order to apply different dipolar coupling distribution profiles equation 3.1.18 needs to be modified:

$$I(t) = I_0 e^{-t/T_{1\rho}} \left[1 - \lambda e^{-\frac{t}{T_{dif}}} - (1-\lambda) e^{-\frac{3t}{2T_{dif}}} \sum_i P(b_i/2) \cos(2\pi b_i t/2) \right]. \quad (4.2.6)$$

Spin coupling distribution profile $P(b/2)$ is introduced. The averaging of $\cos(2\pi b_i t/2)$is performed by summing its values weighted by the fraction of spin pairs with a set of special parameters that corresponds to the oscillation frequency $b_i/2$. Its shape for disordered solids is complex. $P(b/2)$ can be considered as the envelope of the superposition of Pake singularities from the spin pairs having different internuclear distances (Fig 4.2.8). Actually, similar spin pairs Pake singularities superposition is clearly seen in the previous chapter (Fig. 4.2.4) where cut-off averaging Gauss distribution was utilized for *P(b/2)*. Hence, now the Gauss ($G \sim \exp(-(b_i - b_0)^2/2w^2)$), Lorentz ($L \sim w/((b_i -$

$b_0)^2+w^2$) and Radial ($R \sim 4\pi g(r)r^2dr$)functions were used for describing spin coupling distribution profile, as well as T_2 averaging model (3.1.18). The shape of $P(b/2)$ is in generally unknown. Moreover, it is different at various length scales. However the blurring of CP signal oscillations due to the increase of structural disorder and spin-diffusion rate can be demonstrated roughly taking $P(b/2)$ to be Gauss function $G \sim \exp(-(b_i - b_0)^2/2w^2)$.

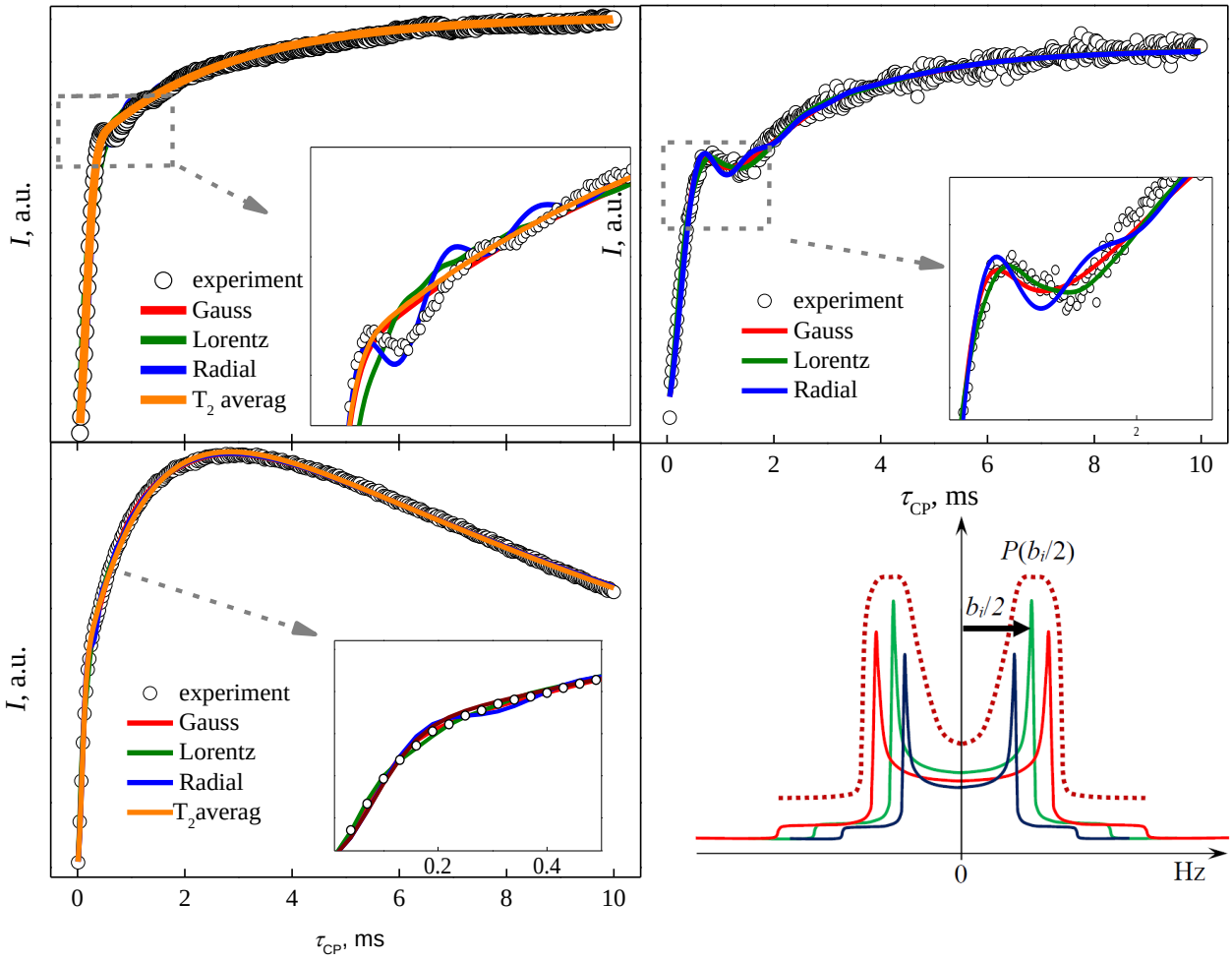

Fig. 4.2.8. ^{1}H -^{31}P CP kinetics (integrated signal intensity *vs.* variable contact time) in the sample containing nano-CaHAp (upper left – static, upper right – MAS 9kHz) and ACP-CaHAp (lower left). The fitting was carried out using Eq 4.2.6 taking $P(b_i/2)$ to be Gauss, Lorentz and Radial functions and using T_2-averaging (Eq 3.1.8). The fit parameters are given in Table 4.2.2. More comments in text. Dipolar splitting and spin coupling distribution profile for disordered solids – lower right.

This choice can be supported by the fact that the ^{31}P NMR signals were found being in many cases Gauss as mentioned before. The width parameter (w) reflects the extent of the overall spin coupling distribution and the relaxation rates. The results of simulation are shown in figure 4.2.9.

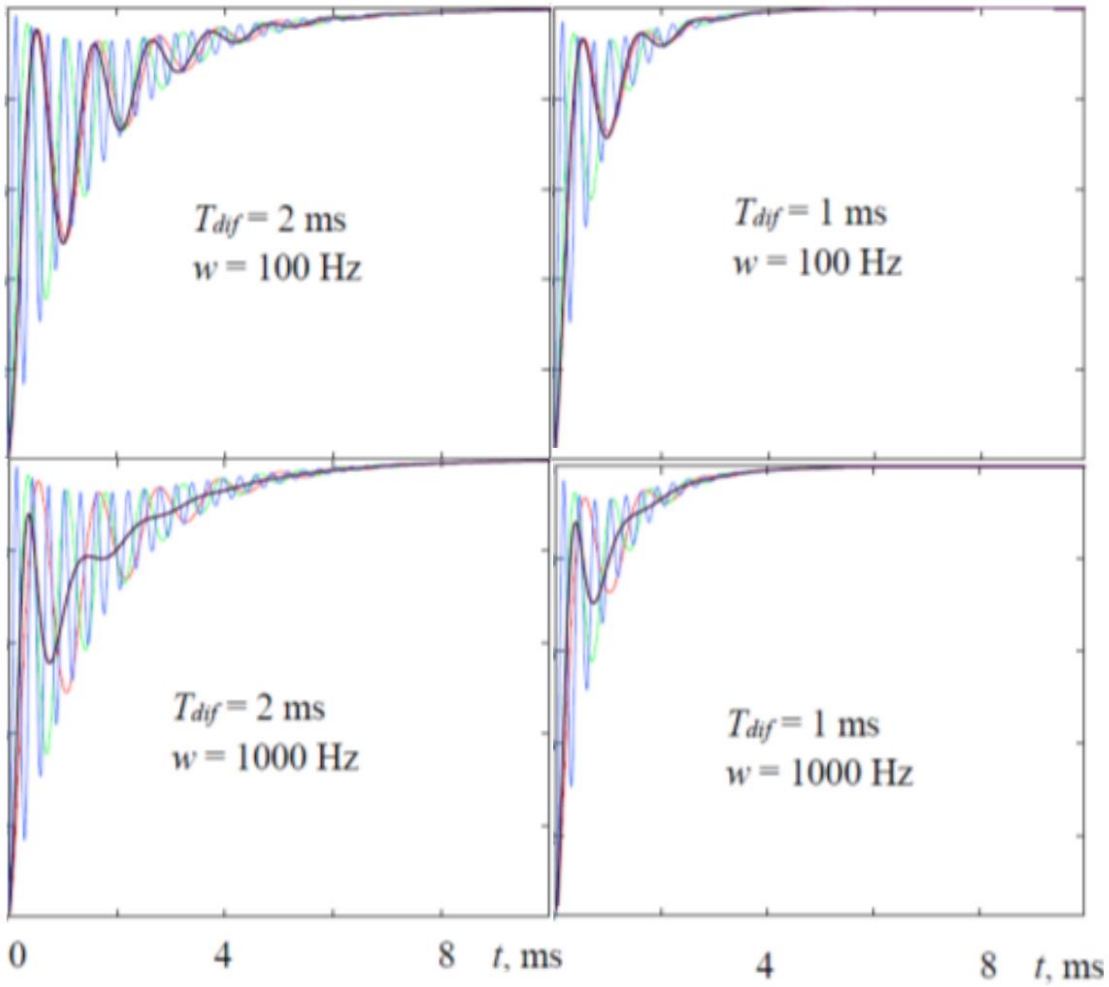

Fig. 4.2.9. The oscillation blurring in CP kinetics upon increase of structural disorder (w) and spin-diffusion rate (T_{dif}). The averaged intensity $I(t)$ (Eq 4.2.6) is shown by bold line in each graphs. The spin coupling distribution profile $P(b/2)$ was modelled by Gauss function centered at b_0 = 1800 Hz and $T_{1\rho} \to \infty$ in all cases.

The observed evolution of $I(t)$ upon changing T_{dif} and w means that the information about the dynamic features (spin diffusion and relaxation) as well as about the structural organization can be obtained by the proper processing of the experimental CP kinetic curves. To corroborate this in

chapter 4.2.1 the T_{dif} was found being 7.6 ms and longer lasting oscillations (Fig 4.2.6) was observed compared to figure 4.2.8. This hints that such drastic change in the spin diffusion time could be a sensitive probe for studying complex innovative materials as the nano-structured HAps analysing the manifold of the structural hydroxyl group communication between phosphate groups via CP transfer.

The experimental kinetic curves (Fig 4.2.8) were processed applying equations 4.2.6 and 3.1.18. The spin coupling distribution profile $P(b/2)$ that is necessary for equation 4.2.6 was modelled by various simple functions. Beside Gauss ($G(b) \sim \exp(-(b/w)\text{^}2)$) and Lorentz ($L(b) \sim 1/(1 + (b/w)\text{^}2)$) profiles the radial distribution function approach was probed in addition. It is based on some ideas of atomic distribution functions developed to describe disordered (polycrystalline and amorphous) systems [125]. Namely, the atomic radial distribution function $g(r)$ contains several sharp peaks close to $r = 0$ that correspond to the first- and the second coordination shells (Fig 4.2.10). The number of atoms in the spherical shell having the radius r and the thickness dr is proportional to $4\pi g(r)r^2\mathrm{d}r$. In order to apply it constructing the spin coupling distribution profile the number of atoms have to be considered as the number of spins I concentrated in the sphere shell surround the spin S, i.e. $N_I(r) \sim 4\pi g(r)r^2\mathrm{d}r$. The profile $P(b)$ is then proportional to N_I, expressed as the function of the dipolar splitting b. According to equation 4.2.4 is known that $b \sim 1/r^3$. On the other hand $g(r) \rightarrow 1$, if $r \rightarrow \infty$. Hence, asymptotically $N_I(r) \sim r^2$. Then the shape of spin coupling distribution $P(b)$ can be approximated by the radial distribution $R(b) \sim b^{-2/3}$ that should work well in the far range, i.e. at low b values (Fig. 4.2.10).

The perfect global fit (the fit over the all experimental points) was achieved in all cases ($R^2 \sim 0.993 - 1$ and $\sqrt{\overline{\chi^2}}/I_{max} \sim 0.3 - 1.6$ %, see Table 4.2.2), independently on the spin coupling distribution profile was used.

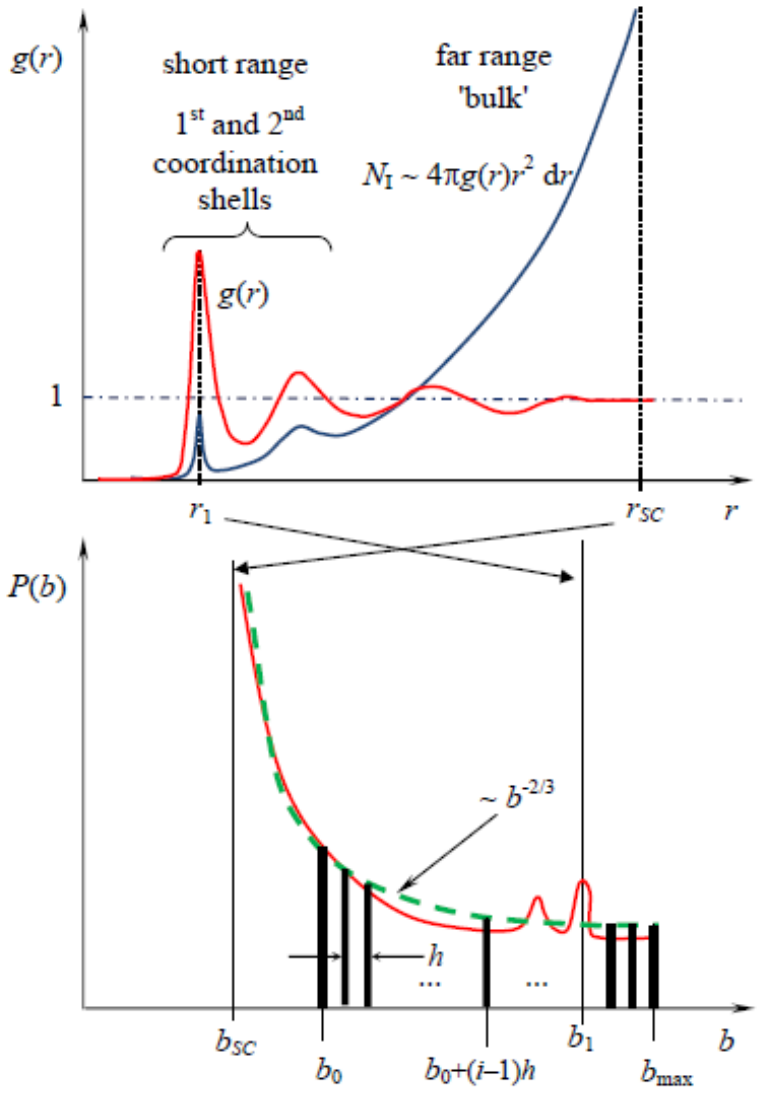

Fig. 4.2.10.Radial distribution function approach. The optimal step for discrete treatment h and the spin coupling extent (from b_{SC} to b_{max}) were determined in each cases adjusting them during the curve fitting routine (see Table 4.2.2).

However, no one of the used profiles can reproduces the CP kinetics in the range of short contact time 0 ÷ 2 ms (Fig. 4.2.8). It means the information concerning the short range order structures (over 1st and 2nd coordination shells, Fig 4.2.10) is lost if any of G, L and R profiles as well as the overall T_2 averaging (3.1.18) are applied. This becomes particularly obvious in the case of the radial distribution function $R(b) \sim b^{-2/3}$ that was derived taking $g(r) \to 1$, $r \to \infty$. The steepness of G, L and R are similar at $b \to 0$, i.e. moving to the far range. Therefore it was not surprising that for each studied systems the values

of 'bulk' parameters (I_0, λ, T_{dif} and $T_{1\rho}$) that were determined by the global fitting, are practically the same (Table 4.2.2).

Table 4.2.2. The fit parameters of CP kinetic curves presented in Figure 4.2.8.

nano-CaHAp							
	static sample				MAS, 9 kHz		
$P(b) \Rightarrow$	*G*	*L*	*R*	T2averag	*G*	*L*	*R*
I_0, a.u.	1.000 ± 0.003				$(1.07 \pm 0.01)\cdot 10^{10}$		
λ	0.30	0.39	0.39	0.33	0.60	0.60	0.61
T_{dif}, ms	2.6	2.2	2.2	2.5	2.2	2.2	2.1
$T_{1\rho}$, s	∞				∞		
b_0, Hz	0	320			800	885	
w, Hz	1920	1290			850	590	
T_2, ms				0.24			
b_{max}, Hz			3500				2200
b_{SC}, Hz			330				740
R^2	0.998	0.994	0.998	0.998	0.994	0.995	0.993
$\sqrt{\overline{\chi^2}}/I_{max}$, %	0.7	1.4	0.7	0.8	1.6	1.5	1.8
ACP-CaHAp							
	static sample				MAS, 5 kHz		
$P(b) \Rightarrow$	*G*	*L*	*R*	T2averag	*G*	*L*	T2averag
I_0, a.u.	$(8.47 \pm 0.03)\cdot 10^{11}$				$(2.07 \pm 0.02)\cdot 10^{11}$		
λ	0.64	0.65	0.69	0.69	0.73	0.75	0.70
T_{dif}, ms	1.4	1.4	1.3	1.4	0.9	0.9	1.0
$T_{1\rho}$, s	0.015				0.011		
b_0, Hz	0	0			0	0	
w, Hz	4600	2500			2500	1400	
T_2, ms				0.12			0.34
b_{max}, Hz			7600				
b_{SC}, Hz			470				
R^2	0.999	0.999	0.999	0.999	1	1	1
$\sqrt{\overline{\chi^2}}/I_{max}$, %	0.5	0.6	0.7	0.7	0.3	0.3	0.3

The challenge to recover the lost information pushes to the idea which was applied in previous chapter (chapter 4.2.1). Where the reconstruction of a ‘true’ *P(b/2)*is performed by the inverse Fourier transform

from t- to b- domain. The relation 4.2.2 is modified to implicate spin coupling distribution profile:

$$P(b/2) \sim \left| \widehat{\mathrm{FT}}^{-1} \frac{1-\lambda f_1 - I(t)/(I_0 f_2)}{(1-\lambda) f_1^{3/2}} \right|, \qquad (4.2.7)$$

where, however, two dynamic factors of spin-diffusion $f_1 = \exp(-t/T_{dif})$ and spin-lattice relaxation in the rotating frame $f_2 = \exp(-t/T_{1\rho})$ as well as the parameter λ that characterizes the cluster structure have to be known. Those quantities describe the CP kinetics over the long contact time. The values of I_0, λ, T_{dif} and $T_{1\rho}$ were taken as the averages over the set of profiles (*G*, *L*, *R*) for each curves (Table 4.2.2) and used in the actions of Eq 4.2.7. The profile $P(b/2)$ obtained in this way can be considered as a goal. The final results of this processing of experimental data including the recalculation of $P(b/2)$ from *b*-variable to internuclear distances (*r*) are presented in Figure 4.2.11. There are seen essential differences between spatial distributions of protons surround ^{31}P nuclei in the studied nano- and amorph-CaHAs in the short range.

The spatial distribution profiles consist of 3 maxima at 0.24 - 0.27 nm, 0.30 - 0.34 nm and at ca 0.5 nm. The differences are seen in their relative heights and in the resolution of the peaks. Particularly interesting is the clear presence of the peak at 0.24 - 0.27 nm in nano-CaHAp under static condition (Fig. 4.2.11). The distances of 0.21 - 0.25 nm are typical for P–O–H structures that are found in some related systems, as calcium phosphate gelatin nano-composites, sol-gel derived SnO_2 nano-particles capped by phosphonic acids, potassium- and ammonium dihydrogen phosphates (KDP and ADP) [103, 124, 126,]. In CaHAp the protons are not part of the phosphate group, and thus such short P···H contacts should not be met. In pure crystalline CaHAp each P atom has two protons distanced at 0.385 nm, further two at 0.42 nm, while others are 0.6 nm or more away [127]. Nevertheless some observations using FTIR and NMR techniques suggest or even confirm the presence of hydrogen phosphate units in the nano-structured samples. It is a hard task because the manifestation of hydrogen phosphate groups are often hidden under other

spectral features. E.g. the FTIR band of HPO_4^{2-} at ca 540 cm^{-1} is strongly overlapped by the intensive modes of PO_4^{3-} in the regular apatitic environment [75].

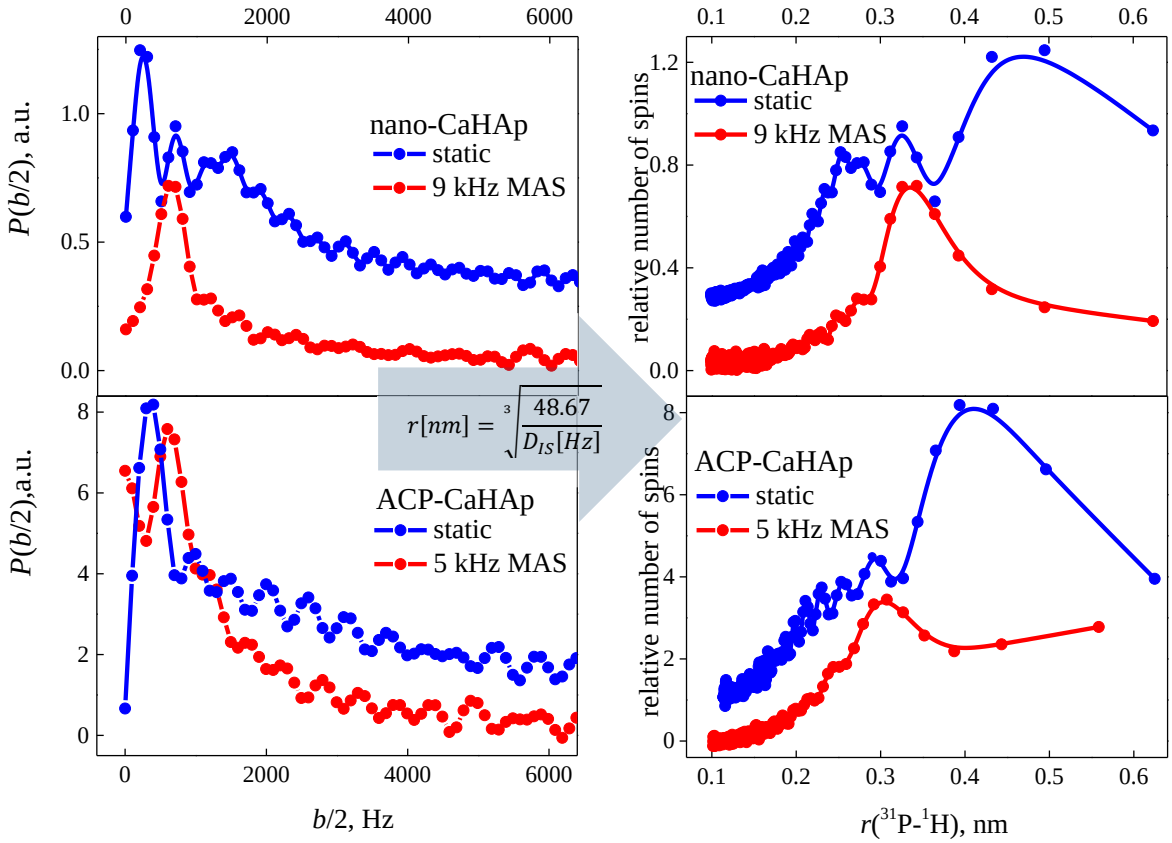

Fig. 4.2.11. The spin coupling distribution profiles $P(b/2)$ (nano-CaHAp – top, ACP-CaHAp - bottom), spatial distributions of protons surround ^{31}P nuclei (nano-CaHAp – top, ACP-CaHAp – bottom) and the MAS effect (more comments in the graph and text). In the cases of CP MAS, D_{IS} were rescaled (see comment in text).

In NMR spectra, i.e. ^{1}H signal at ~ 11 ppm is very broad and ^{31}P at ca 0.45 - 1.3 ppm, look like to be the shoulders of the strong central dominant peaks from the bulk [26, 69, 74, 75]. Hence, in all these cases HPO_4^{2-} signal/band to be resolved it requires rather precise band separation procedures with *a priory* knowing that this band is present indeed. More clearly the presence of HPO_4^{2-} can be extracted from 2D HETCOR experiments [69]. Also note the possible presence ^{31}P–^{1}H spin pairs with the closest distance 0.22 - 0.25 nm in calcium phosphate gelatin nano-composites has been deduced from the simulation of

CP kinetics [124]. The P–O–H structural motifs with P...H distances of 0.2 - 0.25 nm are present mainly on the surface layer that is not seen in XRD because of its disordered nature [69]. Therefore the fact that the peak at 0.24 - 0.27 nm is clearly resolved in the spatial distribution profile of the nano-CaHAp sample and hardly noticeable in the case of ACP-CaHAp (Fig. 4.2.11) is easily understood taking into account the differences in surface organization in nano-structured and amorphous materials. Contrary to this, in the ^{1}H MAS spectrum of ACP-CaHAp a peak attributed to surface H_xPO_4 was resolved (Fig 4.1.5) while it was not observed for nano-CaHAp. Probably this happened because of the lack of the structural OH groups which enabled the peak to be noticeable. Nevertheless, as mentioned before the peak at 0.24 - 0.27 nm under MAS condition is noticeable in the ACP-CaHAp.

These two differently structured systems are interesting to compare according to the remote P···H contacts. It is seen that the relative amount of the remote P···H contacts ($r(^{31}P–^{1}H)$ > 0.5 nm) in ACP-CaHAp is much higher than in nano-CaHAp (Fig 4.2.11). Both materials were already compared respect to the presence of structural manifolds of hydroxyl groups by mean of ^{1}H NMR in chapter 4.1. It was deduced that the amount of structural –OH groups in nano-CaHAp is significantly higher than that from adsorbed water and *vice-verse* in ACP-CaHAp. The ^{1}H and ^{31}P spin-lattice T_1 and spin-spin relaxation T_2 time measurements have revealed that the fast spin motion with the correlation time $\tau = 6.9 \cdot 10^{-6}$ s at ~ 300 K takes place in ACP-CaHAp [119]. The effect of MAS rate on the ^{31}P signal shape supports that the correlation time of this motion gets into the time scale of microseconds or even nanoseconds. Such fast dynamics can be attributed to the rotational diffusion of water molecules. The spin dynamics in nano-structured CaHAp is much slower ($\tau \sim 3.3 \cdot 10^{-5}$ s) [119]. Without discussing the true origin of these protons (adsorbed water [77]/ deviation of the H atom of the –OH ions with sequent displacements of corresponding oxygen atoms that lead to the appearance of distances typical for H-bonds [54]) and correlating all these data with the

profiles presented in Fig. 4.2.11 it can be stated that the remote protons are certainly involved in the H-bond network.

More comments concerning the MAS effect on the obtained spin distribution profiles are necessary. If the spin diffusion processes are slow enough the assumption of isolated $^{31}P–^{1}H$ spin pairs becomes more realistic [128]. The CP kinetics should exhibit then more pronounced oscillations of intensity (Fig. 4.2.9). The dominant dipolar coupling can be then revealed and the P···H distance values can be extracted either performing Fourier transform of the magnetization curves [80, 84, 128] or from CP kinetic curves by a single cosine treatment (Eq 3.1.16) [75, 126]. It means no reducing of the far range order effects through the developed treatment, i.e. applying Eq 4.2.7, is necessary. However for the studied nano-CaHAp the value of T_{dif} is practically not changing getting from the static regime to MAS, whereas for ACP-CaHAp it even slightly decreases (Table 4.2.2). On the other hand it is known that MAS technique fails to suppress anisotropic spin interactions fully, if intensive reorientational dynamics is present [115]. The MAS line width becomes dependent on the spin interaction strength, the time scale of the motion and the spinning rate [115, 119]. Thus, certain dipolar interactions are decimated which is reflected in the changes of NMR signal widths and in the spatial distribution of interacting spins (Fig. 4.2.11.). It follows that ^{31}P interactions with the protons on the surface layers (the peak at 0.24 - 0.27 nm) or with remote protons ($r(^{31}P–^{1}H) > 0.5$ nm) are affected by MAS most dramatically. Moreover, the decimation of spin interactions upon MAS is pronounced also on the structural parameter λ. Its change from $\lambda \approx 0.35$ (static sample) to 0.6 (MAS, see Table 4.2.2), that means that the effective number of interacting spins in the $^{31}P–(^{1}H)_n$ spin cluster in nano-CaHAp changes when MAS is applied.

The weak point of the above treatment has to be recognized. Namely, it starts from the expression (eq 3.1.16) that is valid for one particular orientation of the dipolar tensor with respect to the external magnetic field (eq 4.2.4). The

averaging in eq 4.2.6 using *P(b/2)* covers the *b*-distribution over the distances as well as over the orientations. This can mask or distort the true distribution of the internuclear distances alone. On the other hand, the peaks in the fine structure of *P(b/2)*, if it is succeeded to resolve experimentally (Fig. 4.2.11), correspond to the edges of Pake-like doublets, that is, they are valid for one particular orientation (θ_i, as it is shown in 4.2.8 right bottom). Purely distance-depending distribution *P(D)* can be determined by removing the angular effects. Such treatment can be carried out starting from the expressions for CP kinetics derived for a powdered sample [28, 86] However, a rather complicated mathematical problem appears in this case; instead of routine Fourier transform determining *P(b/2)* (eq 4.2.7), the distribution *P(D)* is extracted processing CP kinetic data either by applying nontrivial Hankel transform or solving the equation of convolution that gets into the class of so-called ill-posed problems. The elimination of the angular effects will be discussed in chapter 4.2.4.

4.2.3 CP beating effect

Another observed but not yet explained effect in this nano-CaHAp sample is the CP kinetics beating (4.2.12). According to classical mechanics, if two harmonic signals interfere which differ in frequency much less than initial frequency, beatings are observed. Under sufficient high MAS rate (>5 kHz) beatings appear in the CP kinetics profile (4.2.12). It is important to note that in chapter 4.1 it was shown that there are no significant line narrowing above 5 kHz of MAS, in other words the dipolar coupling is fully averaged out. The reasoning for beating effect is still not clear, therefore experimental systematic errors that may coherently interfere have to be taken into account, namely RF inhomogeneity of the NMR coil or the decoupling pulse sequences used during the FID observation. The RF inhomogeneity in the NMR coil is always present at some extent. Nevertheless, it was proved that rather high RF inhomogeneity in the NMR coil has little impact to observed spectral parameters though the use of samples that are space-restricted within MAS rotor to the homogeneous

region of the coil is highly advantageous [136]. For this reason a reduced volume sample was prepared, the sample was placed in the centre of the MAS rotor, where RF field is the most homogeneous.

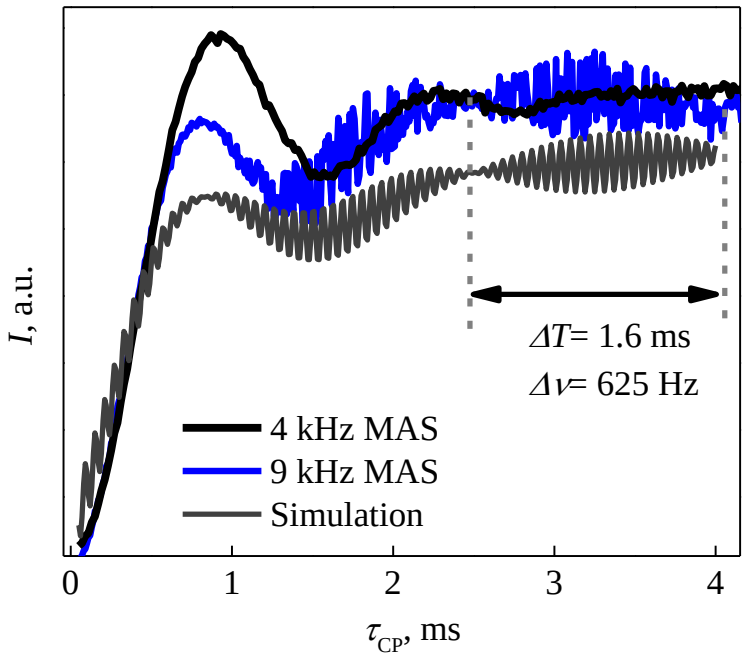

Fig. 4.2.12. CP beating effect in the reduced volume nano-CaHap sample. Black line – 4 kHz MAS, n_{HH}=-1; blue line – 9kHz MAS n_{HH}=-1, Grey line – Simulation. More details in the text.

After this improvement the observed beatings were even more pronounced. Moreover, a decoupling sequences where investigated as target for the cause, namely *CW* and *Spinal64* which showed absolutely no impact to the beating effect. Therefore there were a simulation performed which showed that the beating carrier frequency is at the order of 10^4 Hz and the difference in both frequencies is 625 Hz. It is hard to assess carrier frequency exactly due to a present noise level. If we recalculate from frequency to distance domain (from *b* to *r*) using methods described before, value of ~ 0.12 nm is obtained which is similar to P–H bond length ~ 0.14 nm which was determined for phosphite anion [129]. Nevertheless, the presence of phoshite anions, which could cause CP beating cannot be proved. What is more, the complementary analysis of FTIR spectra did not rigorously confirm the presence of phosphite anion because the band of CO_2 traces from the air is usually present at the same wavenumbers. Another reasoning could be the accomplishment of quasi-

equilibrium (this term will be used in the forthcoming chapters, therefore no explanation will be given here regarding it). Sakellariou et al showed that the system is driven to the periodic state which is synchronised to the rotation after transient oscillations are damped in ferrocene and alanine samples [134]. The evaluated beating carrier frequency being at the order of 10^4 Hz seems comparable to 5-9 kHz of MAS spinning, so the periodic oscillation, after the dipolar oscillation is damped due to spin diffusion, might be possible. Moreover it was theoretically calculated that beatings may appear in six-spin system applying Lee-Goldburg CP pulse sequence for α-alanine [135]. As the nano-CaHAp system is not an isolated system consisting of two spins, beatings may be very plausible. It is important to note, that this is only an initial hypothesis. Therefore this phenomenon should be investigated more in details employing precise theoretical approach. This is a stimulating topic and certainly will be analysed in a near future.

4.2.4. Angular averaging

The elimination of the angular effects for the dipolar tensor is important without a doubt. For this reason a much more simple system was chosen, namely ammonium dihydrogen phosphate ($NH_4H_2PO_4$) which was extensively investigated by means of XRD and ND. Therefore a numerous literature sources are available describing crystal structure and proximities between various atoms in the crystal structure (Fig 4.2.13) [101-110]. The spin-lattice relaxation time T_1 of ^{1}H nuclei in ADP is much smaller compared to CaHAps therefore a CP kinetics profile containing more data points to perform non trivial processing unambiguously is obtained within more acceptable period of time [119, 137]. Similarly as before, ^{1}H-^{31}P CP kinetics measurements were performed.

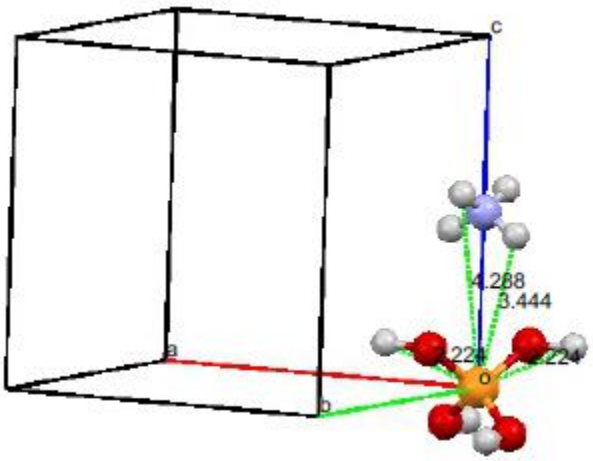

Fig. 4.2.13. Crystal unit cell of ADP and the essential internuclear distances between P and H atoms according to the neutron diffraction data [108].

The CP kinetics observed in powdered ADP exhibit the blurred oscillation of intensity in the short- and moderate contact time range (Fig 4.2.14) similar to previously studied systems (chapter 4.2.1/2). Firstly, equation 3.1.16 is modified [28, 86 and refs cited therein]:

$$I(t) = I_0 \left\{ \frac{1}{2} \left[e^{-\frac{t}{T_{1\rho}}} - e^{-k_1 t} g(t) \right] + \left(\frac{\langle S \rangle_{qe}}{\omega_{0I}} - \frac{1}{2} \right) \left[e^{-\frac{t}{T_{1\rho}}} - e^{-k_2 t} \right] \right\}, \quad (4.2.8)$$

where ω_{0I} is the Larmor frequency of I spins, $\langle S \rangle_{qe}$ is the quasi-equilibrium polarization of S spin inside the extended spin-system S–I_N that can be expressed by:

$$\langle S \rangle_{qe} = \frac{N}{N+1} \omega_{0I} \,, \quad (4.2.9)$$

and the function $g(t)$ describes the oscillatory behaviour of polarization averaged over a set of θ:

$$g(t) = \frac{1}{2} \int_0^{\pi} \cos(2\pi b t/2) \sin(\theta)\, d\theta. \quad (4.2.10)$$

In the case of S–I_N systems containing non-equidistant pairs of interacting spins the oscillatory term in the CP intensity behaviour:

$$I_{osc}(t) = \overline{\cos\left(\frac{2\pi b t}{2}\right)} = \sum_i P(b_i/2) \cos(2\pi b_i t/2), \quad (4.2.11)$$

has to be averaged not only over the angular distribution (Eq4.2.10) but as well as additionally over the set of internuclear distances. Both operations could be carried out in one step if the spin coupling distribution profiles $P(b/2)$ were known. Assuming that at the long contact time and long-distances $P(b/2)$ and its Fourier image can be approached by the Gauss functions (Eq 3.1.17), the function $g(t)$ in Eq 4.2.8 can be simply replaced by the Gauss decay $I_{osc}(t) = \exp(-t^2/2T_2^2)$. Processing experimental data instead of the quasi-equilibrium polarization of S spin it is more convenient to use the spin number N (Eq 4.2.9) that contains the information on the relative size of the spin-system. All these simplify Eq 4.2.8 essentially:

$$I(t) = I_0/2 \left\{ \left[e^{-\frac{t}{T_{1\rho}}} - e^{-k_1 t} e^{-\frac{t^2}{2T_2^2}} \right] + \left(\frac{N-1}{N+1} \right) \left[e^{-\frac{t}{T_{1\rho}}} - e^{-k_2 t} \right] \right\}, \quad (4.2.12)$$

making it simply to apply in the processing of experimental data (Fig 4.2.14). The perfect global fit (the fit using all experimental points over 0 ÷ 10 ms) was achieved getting the nice values of the correlation coefficient $R^2 \sim 0.990$ and the standard least-square deviation $\sqrt{\overline{\chi^2}}/I_0 \sim 1.2$ %. Note, in order better to

reproduce the long-time behaviour the rate constants k_1 and k_2 were treated as independent quantities [28, 86].

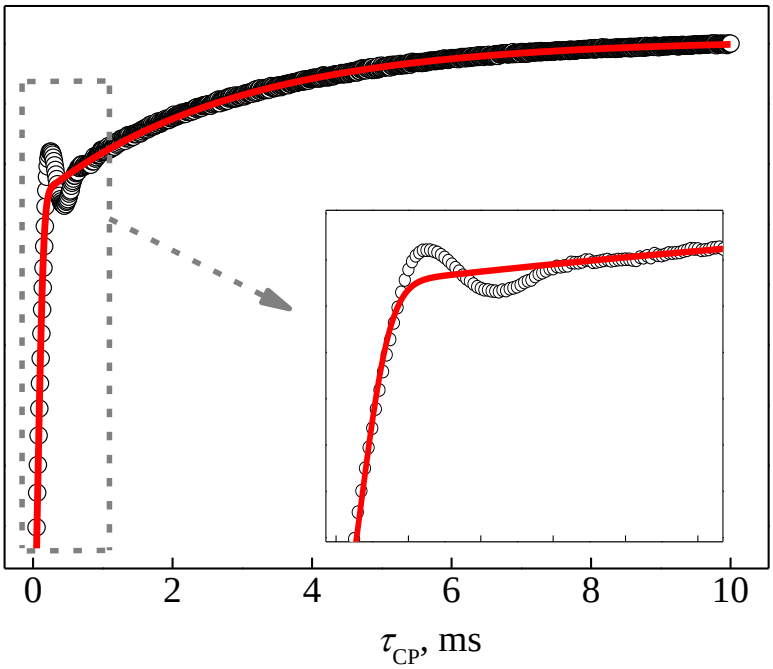

Fig. 4.2.14. ^{1}H -^{31}P CP MAS kinetics (integrated ^{31}P signal intensities *versus* variable contact time) in powdered ADP (7 kHz MAS, Hartmann-Hahn matching for $n = -1$, room temperature). The fit parameter values in Eq 4.2.12 are: $I_0 = (3.181 \pm 0.006)\ 10^9$ a. u.; $k_1 = 539 \pm 7\ s^{-1}$, $(N - 1)/(N + 1) = 0.362 \pm 0.002$; $T_2 = (7.65 \pm 0.05)\ 10^{-5}$ s; $T_{1\rho} \rightarrow \infty$; $k_1 = 3k_2/2$ was kept fixed (more comments in text).

However, it had no sense in the present case. The perfect fit over the whole time range was obtained using the fixed ratio $k_1/k_2 = 3/2$ as it is sequent from the definition of the isotropic spin-diffusion superoperator [95]. Moreover, the fitting allowing to vary k_1 and k_2 independently led to the nonsensical situation - the values of these parameters were determined with the margins of error up to ± 100 %, without any significant improvement in R^2 and χ^2 values. This means either the experimental data set was not ample to reveal the deviations from the isotropic model (despite each kinetic curve contained ~ 1000 points) or the isotropic spin-diffusion model is indeed adequate for the studied system.

Despite the perfect global fit, the run of CP transfer cannot be reproduced in the short contact time range, namely, within 0 ÷ 2 ms (see the insert in Fig 4.2.14). This means the information about the short range order structure

details is lost, similarly as in chapters 4.2.1 and 4.2.2, if Gauss decay function (3.1.17) is applied.

In previous chapters the internuclear distances in the nano-CaHAps were obtained by the reverse processing the CP kinetics. The oscillatory term was extracted from the CP kinetics cleaning out the incoherent contributions. The shape of $P(b/2)$ was determined by performing an inverse Fourier transform of the oscillatory term from *t*- to *b*-domain. However it was carried out only for the 'edges' of Pake-like doublets. The purely distance-depending distribution $P(D)$ can be determined by removing incoherent far-range order contributions and carrying out the angular averaging.

The Eq 4.2.12 was applied at the starting point to process the experimental CP MAS kinetics. Taking into account the above remark that $k_1/k_2 = 3/2$, then $I_{osc}(t)$ can be expressed as:

$$I_{osc}(t) = \frac{f_2}{f_1} + \frac{N-1}{N+1}\left(\frac{f_2}{f_1} - f_1^{-1/3}\right) - \frac{I(t)}{I_0 \cdot f_1}. \qquad (4.2.13)$$

In order to be able to apply this equation two factors of spin-diffusion $f_1 = \exp(-k_1 t)$ and spin-lattice relaxation in the rotating frame $f_2 = \exp(-t/T_{1\rho})$ as well as the parameter N that characterizes the relative cluster size have to be known. Similarly as in the previous approaches (Chapters 4.2.1 and 4.2.2) the values of I_0, k_1, N and $T_{1\rho}$ were taken as they were determined processing the experimental data using Eq 4.2.12 (Figure 4.2.14). The extracted $I_{osc}(t)$ is shown in the Figure 4.2.15.

In the next steps the purely angular averaging (Eq 4.2.10) has to be extended including the averaging over the distances (r). Since the internuclear distance are directly related to the dipolar coupling constant (D) (Eq 4.2.4) the purely distance-depending distribution $P(D)$ is introduced for this purpose. Then the complete averaging can be written as

$$I_{osc}(t) = \int_0^{\infty} P(D) \int_0^{\pi} \cos(2\pi bt/2) \sin(\theta)\, \mathrm{d}\theta \mathrm{d}D. \qquad (4.2.14)$$

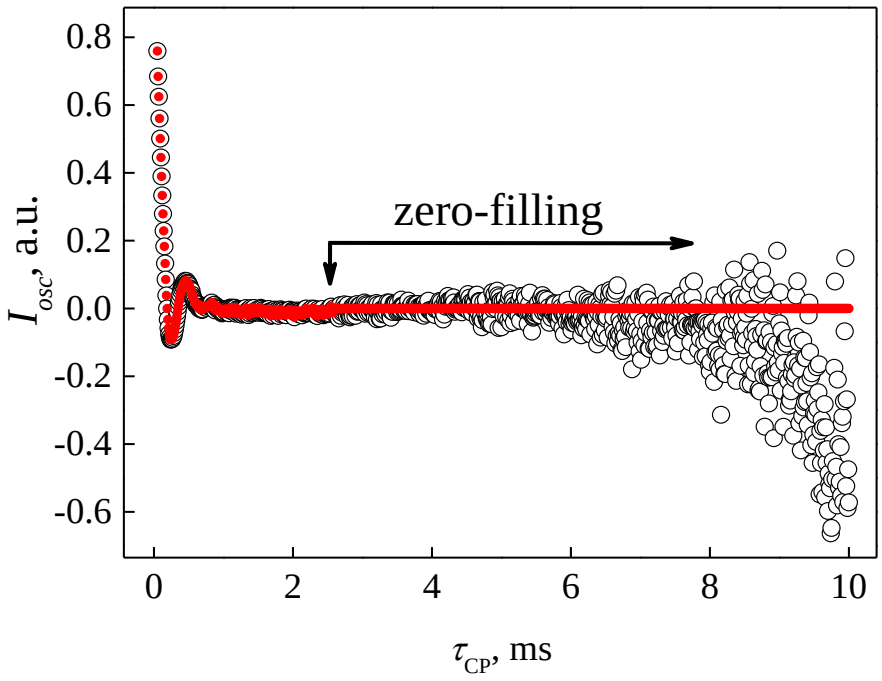

Fig. 4.2.15. CP oscillatory term extracted using relation 4.2.13 with the fit parameter values given in the caption of Figure 4.2.14. The 'noisy' part of the curve with noise level that exceeds the experimental margin of error of CP intensity was smoothed applying the zero-filling.

The angular averaging part in Eq 4.2.14 can be expressed in terms of series of Bessel functions of the first kind $J_k(x)$. These expressions depend on which one of the Hartmann – Hahn sideband matching conditions ($\omega_{\mathrm{II}} - \omega_{\mathrm{IS}} = n\ \omega_{\mathrm{MAS}}$) is fulfilled [28, 89, 130]. The equation describing $g(t)$ at $n = \pm 1$ matching, i.e. the condition fulfilled in the present work, is written:

$$g_{\pm 1}(D,t) = J_0\left(\frac{\pi D t}{\sqrt{2}}\right) + 2\sum_{k=1}^{\infty}\left[\frac{1}{(1-4(2k)^2)}\right] J_{2k}\left(\frac{\pi D t}{\sqrt{2}}\right) \qquad (4.2.15)$$

and then:

$$I_{osc}(t) = \int_0^{\infty} P(D)\, g_{\pm 1}(D,t)\mathrm{d}D. \qquad (4.2.16)$$

Any successful attempt to construct a proper replica for the exact series $g_{\pm 1}(D, t)$, i.e. the kernel function in the integral equation (Eq 4.2.16), would be extremely welcome. It would let to avoid certain mathematical difficulties, like the solution of so-called 'ill-posed' Fredholm equation [89]. Searching for such replica the truncation of Eq 4.2.15 restricting the series by the first member J_0(x) only seems to be quite acceptable (Figure 4.2.16). The statistical

evaluation of deviations from the exact series provides the values R^2 = 0.997, χ^2 = 0.015 over the whole x range 0 - 100 a. u. This is comparable with the experimental precision of CP intensities and can be understood due to very steep suppression (~ $1/(2k)^2$) of the contributions from $J_{2k}(x)$ of higher order. The Eq 4.2.16 can be then rewritten:

$$I_{osc}(t) = \int_0^\infty P(D)\, J_0\left(\frac{\pi D t}{\sqrt{2}}\right) dD \sim \int_0^\infty \frac{P(D)}{D} J_0\left(\frac{\pi D t}{\sqrt{2}}\right) D\mathrm{d}D. \qquad (4.2.17)$$

This means that the functions $I_{osc}(t)$ and $P(D)/D$ are now related by Fourier - Bessel (Hankel) transform [131]. Hence, $P(D)$ can be determined from $I_{osc}(t)$ carrying out the inverse operation:

$$P(D) = \sim D \int_0^\infty I_{osc}(t)\, J_0\left(\frac{\pi D t}{\sqrt{2}}\right) t\mathrm{d}t. \qquad (4.2.18)$$

Moreover, it is also known that the Bessel function $J_n(x)$ at $x \to \infty$ has the following asymptotic form [130]:

$$J_n(x) \sim \sqrt{\frac{2}{\pi x}} \cos\left(x - \frac{n\pi}{2} - \frac{\pi}{4}\right). \qquad (4.2.19)$$

Indeed, the function in this form emulates the track of the exact Bessel series (Eq4.2.15) at the larger x values rather satisfactorily with R^2 = 0.973 and χ^2 = 0.04, respectively. Significant deviations start to appear at $x < 1$, i.e. at $\pi Dt \approx 1$ (Figure 4.2.16). Thus, $J_0(x)$ can be replaced by its asymptotic form, however, with some limitations for very short contact time range and weak dipolar couplings. Such replacement of $J_0(x)$ simplifies Eq 4.2.19 crucially:

$$P(D) = \sim D \int_0^\infty I_{osc}(t) \frac{\cos\left(\frac{\pi D t}{\sqrt{2}} - \frac{\pi}{4}\right)}{\sqrt{\frac{\pi D t}{\sqrt{2}}}} t\mathrm{d}t, \qquad (4.2.20)$$

that means that the goal distribution (purely distance-depending) $P(D)$ can be obtained by routine Fourier transform of $I_{osc}(t) \cdot \sqrt{t}$ from t- to D-domain with the proper rescaling:

$$P\left(\frac{D/\sqrt{2}}{2}\right) = \sim \sqrt{D} \int_0^\infty [I_{osc}(t) \cdot \sqrt{t}] \cos\left(2\pi \frac{D/\sqrt{2}}{2} t\right) \mathrm{d}t. \qquad (4.2.21)$$

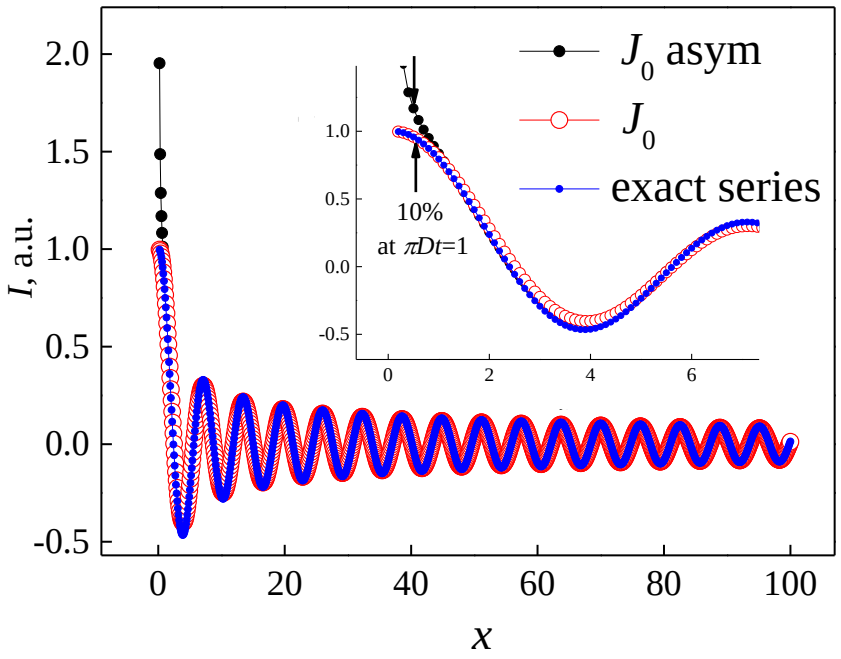

Fig. 4.2.16. Constructing the replica for the exact Bessel series (Eq4.2.15).

As mentioned before (eq 4.2.5), in the presence of MAS the dipolar coupling constant D has to be rescaled depending on the Hartmann-Hahn matching condition, namely in this case $n = \pm 1$ it has to be multiplied by $\sqrt{2}$. The results of this processing of experimental CP MAS kinetics (Figure 4.2.14) including the recalculation of $P(D)$ from D-variable to internuclear distances (r) using eq 4.2.4 are presented in Figure 4.2.17. The spatial distribution profiles consist of 3 maxima at 0.234 - 0.239 nm, 0.357 - 0.376 nm and at 0.476 - 0507 nm, depending on MAS rate and the method of processing. The distance values are given in Table 4.2.3 and compared with the available conventional crystallographic data.

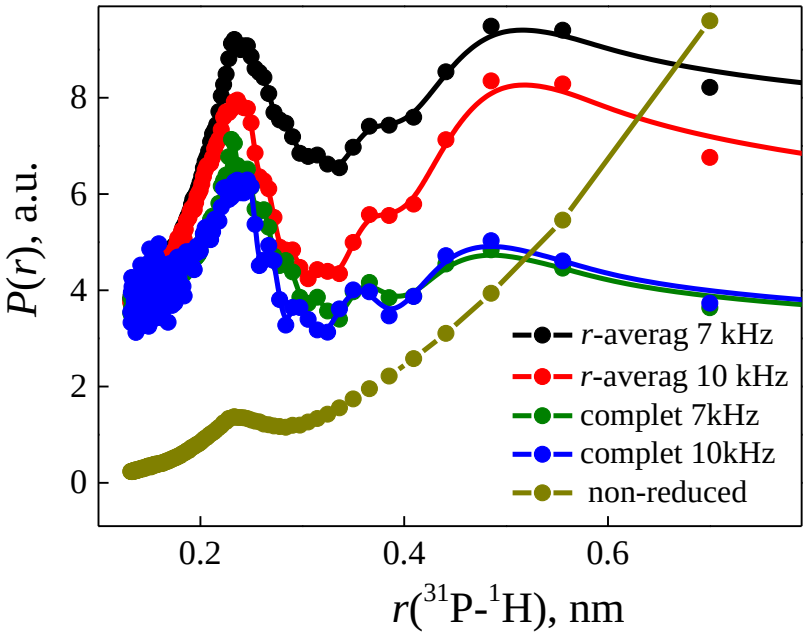

Fig. 4.2.17. Spatial distributions of protons surrounding ^{31}P nuclei in the powdered ADP at 7 and 10 kHz MAS. Besides the results of the complete averaging over the distances and angles (r and θ) obtained applying Eq. 4.2.21, the distributions obtained carrying out only the r-averaging with the fixed $|(1-3\cos^2\theta)/2| \rightarrow 1$ value as well as the simplified treatment applying Fourier transform directly on the kinetic curve with non-reduced incoherent contributions from the remote protons are presented for comparison.

The distances of ~ 0.21 - 0.25 nm which typical for P–O–H structures were determined in previous chapter as well. Similar distances were determined for other systems, namely gelatin nano-composites, aluminophosphates, sol-gel derived SnO_2 nano-particles capped by phosphonic acids , etc [84, 86, 124, 126]. The shortest P···H distance in P–O–H can be considered to be determined most precisely for the following reasons: i) this peak is well-resolved (Fig 4.2.17); ii) it corresponds to the strongest dipolar ^{31}P–^{1}H coupling (D ~ 4000 Hz) and thus the limitation for the replica use $\pi Dt \geq 1$ (Fig. 4.2.16) is certainly fulfilled.

Table 4.2.3. Maxima positions (nm) of the spatial distribution of protons surround ^{31}P nuclei in powdered ADP and comparison with ND and XRD data.

Method	Peak 1	Peak 2	Peak 3
7 kHz MAS *r*-averaging	0.239	0.376	0.507
10 kHz MAS *r*-averaging	0.237	0.376	0.507
7 kHz MAS Complete averaging	0.234	0.364	0.476
10 kHz MAS Complete averaging	0.236	0.357	0.479
Neutron diffraction [108-110], see Figure 4.213	0.219 - 0.222	0.330 - 0.344	0.429 -0.444
X-ray diffraction [103-107]	0.235 - 0.244 0.218 and 0.220*	0.329 - 0.335	0.430-0.441

*- predicted by the calculation using the extended electrostatic valence rule. The hydrogen-atom positions were calculated for the least electrostatic energy in the local environments [104]

The shortest $^{31}P–^{1}H$ distances determined by NMR using CP MAS kinetics get between ND and XRD values (peak 1, Table 4.2.3), whereas those for more remote protons are slightly larger. The differences in the relative peak heights and in the resolution are clearly seen comparing the spatial distributions in Figure 4.2.17. It can be stated that the angular averaging leads to better resolution of the peak 2 that corresponds to P···H contacts with two protons in NH_4^- anion (Fig. 4.2.13). Also the values of the distances between phosphorus and other two remote protons are slightly improved (peak 3, Table 4.2.3).

4.2.5 Noise effects

Nevertheless high amount of variables in theoretical model described in chapter 4.2.4 is reason for doubts in its validity. The computing routine applied is based on the Levenberg-Marquardt algorithm, which is the most widely used algorithm in nonlinear least squares fitting. It is implemented in many packages, e.g., Microcal Origin and Mathcad. The main problem which is met working with the nonlinear fitting arises trying to ensure its convergence towards the "true" (global) minimum on the multi-parameter surface χ^2, i.e., the sum of weighted squares of deviations of the chosen theoretical model curve from the experimental points. Several or even a forest of local "false" minima can be present on χ^2 surface depending on complexity of the model, precision, and completeness of the experimental data set. The path of the flow $\chi^2 \rightarrow$ min depends on the choice of the initial (zero-order) parameter set. Starting with some non-properly chosen parameters the procedure can converge towards "false" local minima (Fig.4.2.18).

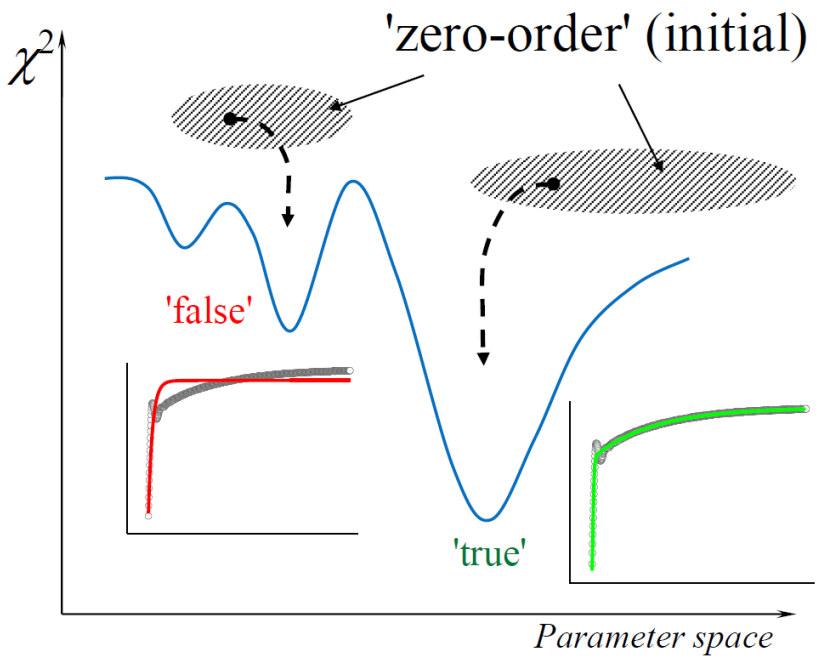

Fig. 4.2.18. Non-linear multi-parameter fitting: the problem of flow towards the "true" (global) minimum. More comments in the text.

The acquired experience in the fitting of CP kinetic curves allows to give some criteria and recommendations to recognize the false minima and searching for the proper zero-order parameter set. The false minimum can be easily recognized by following: (i) apparent systematic (non-random) deviations (see "red curve" in Fig. 4.2.18); (ii) relatively low values of R^2; (iii) the values of some adjusted parameters are beyond their physical sense (e.g., $T_2 < 0$). In order to find the right path towards the global minimum for the first iteration it is recommended to keep fixed some parameters that can be *a priori* approximately evaluated from other experimental data. For instance, the spin-spin relaxation time T_2 can be determined from the full width at half maximum (FWHM) of ^{31}P signal for the static sample using the "uncertainty" relation FWHM·T_2 = 0.375 that is valid for the "true" Gauss functions. Another parameter in Eq 4.2.12 – I_0 can be roughly taken as 0.7-0.9 of maximal *I(t)* value and $\exp(-t/T_{1\rho}) = 1$ can be set. Keeping these values fixed the remaining parameters are refined during the first iteration and then taken as zero-order set in the next run. If the correct minimization path is found then all parameters can be varied getting the stable flow to the same minimum without any constraints. In order to study the effect of random errors on the stability of flow and on the values of adjusted parameters the CP kinetic curve (Fig. 4.2.14) was artificially disturbed adding the noise of various levels (Fig 4.2.19) with the sequent repeat of all steps of processing (4.2.20).

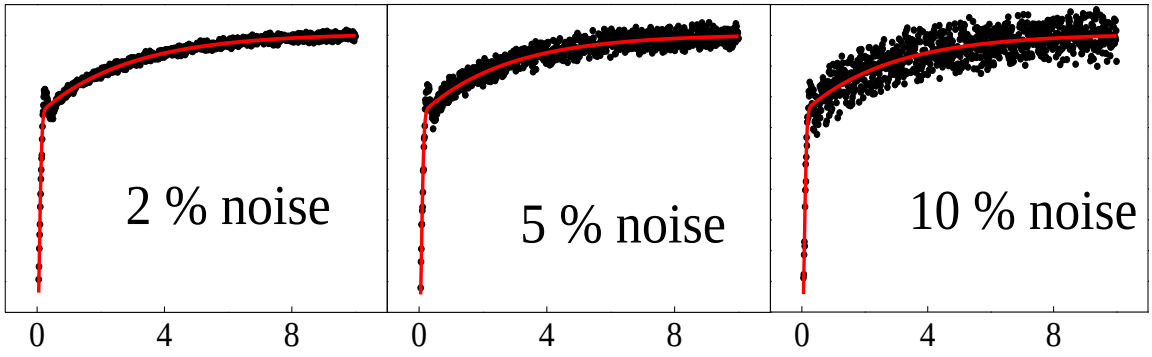

Fig. 4.2.19. Effect of random noise on the CP kinetics.

It is clearly seen (Fig 4.2.20) that the most sensitive parameters to the noise level are k_1, and $p_1 = (N - 1)/(N + 1)$. The effect of noise on the spatial distribution of protons surrounding ^{31}P nuclei $P(r)$ is of particular interest. It can be concluded that the random errors can affect $P(r)$ at longer distances ($r >$ 0.3 nm) significantly if the noise level exceeds 5% whereas the position of the first peak remains to be quite stable.

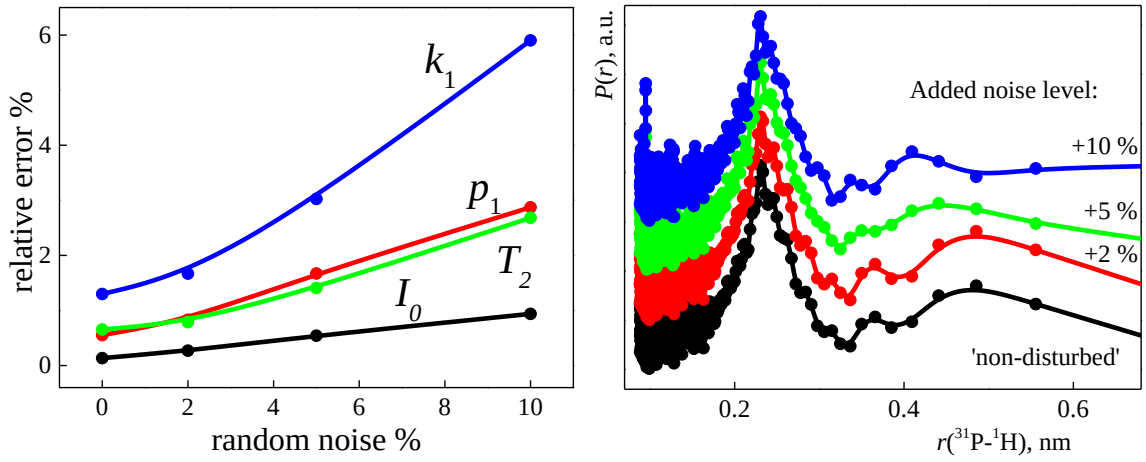

Fig. 4.2.20. Effect on the precision of adjusted parameters (left): I_0, k_1, $p_1 = (N - 1)/(N + 1)$, T_2 (Eq.4.2.12) (the relative error (%) means the standard error put out by the computing routine divided by the value of the corresponding parameter obtained processing dataset without added noise); and on the spatial distribution of protons surrounding ^{31}P nuclei (right).

Resuming, the high experimental data point density on CP kinetic curves makes the minimization procedure quite stable with respect to the random errors. This large data set reduces the excess degrees of freedom in the non-linear fitting procedure targeting its flow towards the global minimum on the multi-parameter surface χ^2. It makes possible more rigorous decision concerning the validity of the hypothetic models and more fitting parameters can be used and determined unambiguously.

4.2.6. Non-Classical CP transfer model's convergence to the classical one.

To choose an appropriate CP transfer model is not an easy task and in most cases it cannot be chosen unambiguously [94]. As it was shown in chapter 4.2.1, even if the CP kinetics looks typical for the classical *I*-*S* transfer model, the non-classical *I*-*I**-*S* describes the experimental observations in the whole dynamic range better (without non-random deviations) (Fig.4.2.2). It seems that the more complicated model should be used in all cases. Therefore, the possibility of the convergence of the non-classical model to the classical one should be analysed. In other words, the conditions when the non-classical model describes the CP behaviour correctly should be pointed out.

In order to do it, the starting point is the equation 4.2.12 which was used to analyse the ADP CP behaviour in chapter 4.2.4. It can be rewritten in a following way:

$$I(t) = \frac{I_0}{2} e^{-\frac{t}{T_{1\rho}}} \frac{N}{N+1} \left\{ 1 - \frac{N-1}{2N} e^{-(k_2 - 1/T_{1\rho})t} - \frac{N+1}{2N} e^{-(k_1 - 1/T_{1\rho})t} e^{-\frac{t^2}{2T_2^2}} \right\}. \quad (4.2.22)$$

In the case when k_1, k_2 >> $1/T_{1\rho}$ and after renormalizing $I_0 \rightarrow I_0 N/(N+1)$ the relation 4.2.22 converts to Eq. 3.1.18, i.e. to the most often used equation of *I*–*I**–*S* model. If the quasi-equilibrium polarization of S spin inside the spin-system S–I_N is realized, in other words the equation 4.2.9 is valid, the parameter λ is then related to the spin cluster size *N*:

$$\lambda = \frac{N-1}{2N}. \quad (4.2.23)$$

Previously this parameter was equal $\lambda = 1/(N+1)$ that was stated maybe more intuitively [79, 94]. It becomes obvious that λ cannot overstep $\lambda \leq 1/2$ if the quasi-equilibrium polarization transfer is present. It provides an additional constraint on the processing of CP kinetic curves. Namely, the results of the

non-linear curve fitting of the model and experimental data set have to be rejected, revised or some assumptions should be taken into account, if the minimization routine leads to $\lambda > 1/2$. In this case the possible physical reasons why the spin quasi-equilibrium was not reached should be carefully analysed.

The Eq. 4.2.12 has the advantage not only because it elucidates the physical sense of the parameter λ, but also because it provides the way to follow the convergence between non-classical and classical spin coupling models without any *a priori* discrimination, which of those should be valid for the system under study. It is quite logical to suppose that at the infinite enlargement of the spin cluster size the non-classical *I*–*I**–*S* model has to convert to the classical *I*–*S* one. And indeed, in this case $N \to \infty$ the requirement for the high dilution of spin S among spins I is certainly fulfilled, i.e. $N_S/N_I \to 0$. Furthermore, if the *I*–*S* heteronuclear coupling is sufficiently reduced by high spin mobility, the CP kinetics should obey the classical *I*–*S* model (eq 3.1.15). In order to follow this conversion eq. 4.2.12 is rewritten inserting $N \to \infty$. Then it turns to:

$$I(t) = I_0 \left\{ e^{-\frac{t}{T_{1\rho}}} - \frac{1}{2}\left(e^{-\left(k_1 t + \frac{t^2}{2T_2^2}\right)} + e^{-k_2 t} \right) \right\}. \qquad (4.2.24)$$

The principal question that arises during the non-linear curve fitting is - whether the expression in the internal brackets (...) could be recognized by the computing as the sum of two exponents, or such behaviour is merged to a single exponential decay:

$$\frac{1}{2}\left(e^{-\left(k_1 t + \frac{t^2}{2T_2^2}\right)} + e^{-k_2 t} \right) \to e^{-a k_2 t}, \qquad (4.2.25)$$

where *a* is the adjustable parameter introduced for rescaling the 'true' spin diffusion rate $k_2 = 1/T_{dif}$. The answer certainly depends on the experimental precision as well as on the parameters k_2, $k_1 = 3k_2/2$ and T_2. This might be

checked by taking the set of some 'realistic' k_2 and T_2. The results are presented in Fig. 4.2.21. The perfect fit (R^2 = 0.997 ÷ 0.999) the was obtained in the case of 'narrow' as well as 'broad' *b*-spectrum, i.e. short- and long T_2, varying only one parameter – the rescaling factor *a* (Fig. 4.2.21). This means that at the present CP transfer regime, which is determined by k_2 and T_2 values, the two- and single exponential decay functions (Eq. 4.2.25) are indistinguishable even when relatively huge data sets of very high precision (computer generated curves with no random noise, 128 points per curve) are processed. Thus it can be stated that for the large spin clusters at the present conditions the 'classical' and 'non-classical' regimes are practically undistinguishable. The eqs 3.1.15 and 4.2.24 become more or less equivalent. What is more, the CP rate constants $1/T_{IS}$ and $1/T_{dif}$ used in those equations are bridged by the relation:

$$\frac{1}{T_{IS}} \rightarrow a\, k_2 = \frac{a}{T_{dif}} \qquad (4.2.26)$$

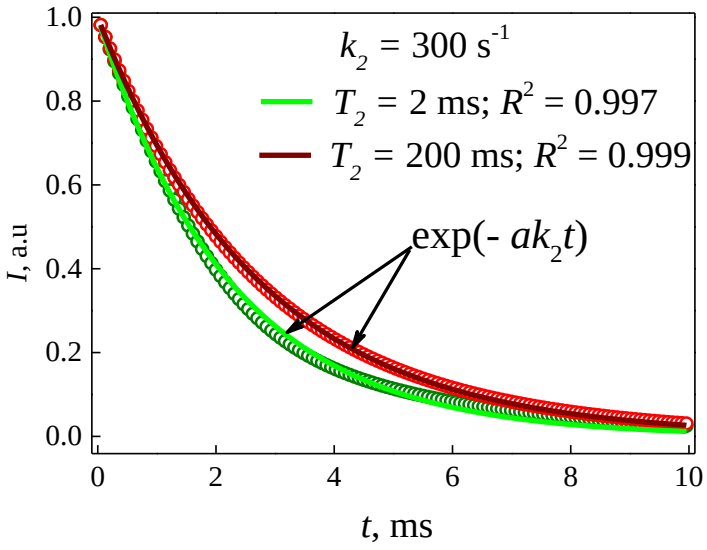

Fig. 4.2.21. The imitation of two exponential terms in Eq. 4.2.25 (computer generated points shown by open circles) by the single exponent with the rescaled spin diffusion rate ak_2 (solid lines). The different T_2 values correspond to 'broad' and 'narrow' distributions of the dipolar splitting. The adjusted *a* values are within 1.2 - 1.5.

It is worth pointing out that the calculated parameter *a* for the ACP-CaHAp analysed in the chapter 4.2.1 using relation 4.2.26 and parameters T_{IS} and T_{dif} obtained there is equal to 1.3 which coincide with above mentioned values. Moreover, the validity of the suggested model in the novel complex composites consisting of the amorphous silicas, namely SBA-15 and MCM-41, and the room temperature ionic liquid (RTIL) 1-butyl-3-methyl-imidazolium tetrafluoroborate [bmim][BF_4] was proven [133].

Conclusions of part 4.2

- High data point density measurements carried out for the ACP/nano-CaHAps and ADP allowed to resolve spin clusters structures within internuclear distances $r \geq 0.125$ nm.

- An apparent difference in the CP kinetics profiles for the nano-structured and the containing the amorphous clustered phosphate phase CaHAps have been revealed.

- The advanced processing of CP MAS data has been developed introducing the variable cut-off Gaussian distribution of the dipolar coupling. The characteristic size of $^{31}P–(^{1}H)_n$ spin cluster being within 0.3÷0.5 nm has been determined for nano-structured CaHAp.

- The far range order effects have been reduced by introducing radial distribution of interacting spins in the processing the CP kinetics

- The short $^{31}P–^{1}H$ contact peak at 0.24 - 0.27 nm resolved in the spatial distribution profile of the nano-CaHAp sample is hardly noticeable in

the case of ACP-CaHAp which reflects the differences in surface organization in the nano-structured and amorphous materials.

- The spin diffusion process in nano/ACP-CaHaps are practically unaffected by MAS (9 kHz). The MAS decimates ^{31}P interactions with the protons on the surface layers and with the remote protons (> 0.5 nm) that are plausibly involved in the H-bond network and thus are highly mobile.

- CP beating effect was experimentally observed for the first time. Hypothesis of the accomplished quasi-equilibrium polarization which leads the beating of the signal intensity was proposed.

- The advanced CP MAS kinetic processing which is based on the reducing the incoherent far range order spin couplings and extracting the CP oscillatory term and sequent mathematical treatment has been introduced. The proper replica has been found that allowed to reduce the Fourier - Bessel (Hankel) transform calculating the angularly-averaged and purely distance-depending spin distribution to the routine Fourier transform.

- The added noise level in the CP kinetics for powdered ADP has little impact to the ^{1}H-^{31}P spin coupling distribution profile which confirms that the applied processing route is reliable method to obtain structural information in the complex solids.

- A tight convergence of 'classical' and 'non-classical' spin coupling models has been deduced. Its validity was proved for the ACP-CaHAp. However, the non-classical model seems to be more preferable because

it directly provides the information on the spin diffusion rate that is originated from the exact microscopic quantum mechanical model.

4.3. An impact of complexing agent to structural aspects of complex CaHAp materials

The advanced methods developed for characterising the spin cluster composition (chapters 4.2.1 – 4.2.6) is a powerful tool to distinguish the structural difference in a very similar compounds at the first glance. Therefore the same specimens discussed in the chapter 4.1, namely EDTA/EG/TA/GL-CaHAps were analysed. It was chosen to apply the processing protocol described in the chapters 4.2.2/4. The reasoning for such choice is that the 'radial distribution' approach together with angular averaging is powerful to distinguish surface and bulk species as well as reduce far range incoherent effects in the nano-structures. The ratio of the surface and the bulk species as well as the relaxation in the rotating frame $T_{1\rho}$, spin diffusion T_{dif} or spin cluster composition λ could be a sensitive probe describing structural differences within various nano-structures. Similarly as in the chapters 4.1.1/4.1.2 the obtained parameters will compared with the ones obtained for the commercially available stoichiometric CA-CaHAp.

The observed CP-kinetic curve for the CA-CaHAp was similar to discussed in chapter 4.2.2 (Fig 4.3.1). Firstly, it was processed using theoretical models discussed in chapters 4.2.4 (eq 4.2.12) and 4.2.6 (eqs 4.2.22 and 4.2.23) employing T_2 averaging approach. The obtained fitting parameters are shown in Table 4.3.1. It is important to note that the adjusted R^2 = 0.98 was calculated in all cases which seems very logical as these models are not capable to mimic transient oscillations. All fitting parameters, namely T_{df}, T_2 were calculated to be similar. Even the introduction of parameter λ did not lead to improper values. It was calculated to be equal to 0.47 which corresponds to the N = 14.71 of interacting spins while using eq 4.2.12 the corresponding parameter was calculated 14.77. Such apparent coincidence is very welcome as it shows that the quasi-equilibrium with the lattice was met in the CA-CaHAp CP kinetics.

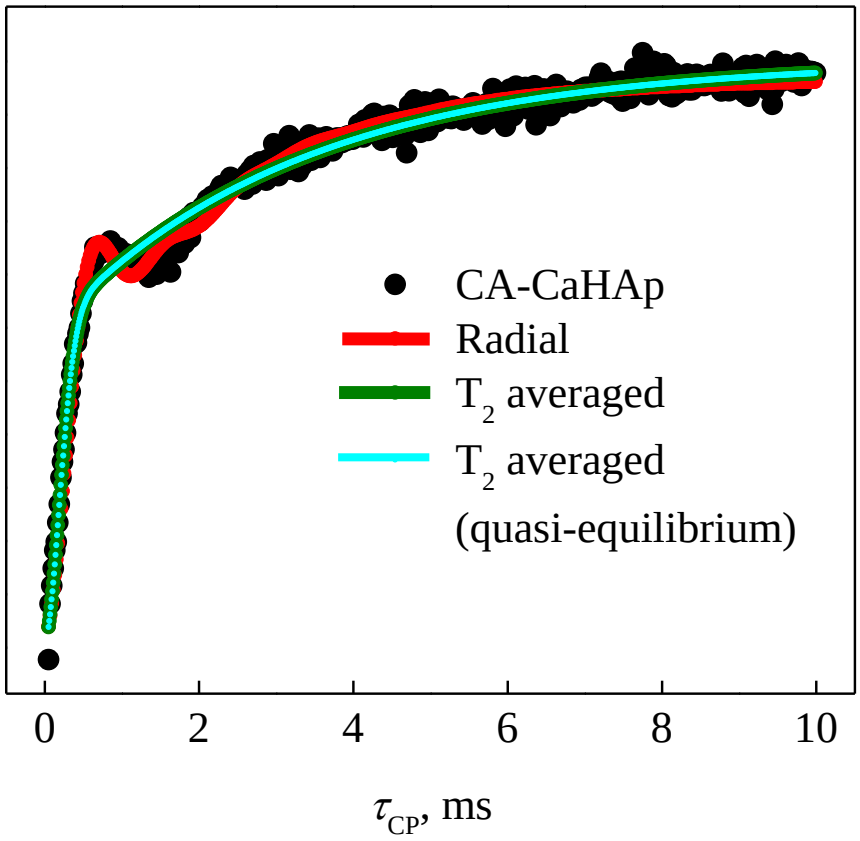

Fig. 4.3.1. ^{1}H-^{31}P CP kinetics in CA-CaHAp together with theoretical fittings: Green line – eqs 4.2.22 and 4.2.23, Cyan line- eq 4.2.12, Red line - eqs 4.2.22 and 4.2.23 using radial distribution instead of T_2 averaging approach. Obtained fitting parameters are shown in Table 4.3.1. More comments in the text.

The introduction of the radial distribution allowed to describe the ^{1}H-^{31}P CP behaviour almost ideal achieving parameter R^2 = 0.99. Nevertheless, this leads the parameter λ to become larger than 1/2, namely 0.61. According to the arguments given in the chapter 4.2.6 parameter λ could not overstep 1/2 if the quasi-equilibrium is met. Most probably in CA-CaHAp system quasi-equilibrium is just or nearly met, therefore parameter λ is around 1/2 using all theoretical approaches. What is more, the maximum dipolar frequency was calculated to be b_{max} = 2124 Hz and the minimum b_{sc} = 694 Hz in the dipolar coupling profile (Table 4.3.1). The calculated spatial distribution using angular averaging (chapter 4.2.4) of protons surround ^{31}P nuclei is shown in Figure 4.3.3.

Table 4.3.1. ^{1}H – ^{31}P CP kinetics fitting parameters for CaHAps derived using various complexing agents as well as for Ca-CaHAp and different dipolar coupling profile approximation approaches.

T_2 averaging, n_{HH} = -1, ν_{MAS}=5 kHz						
Sample	I_0, a.u.	$T_{1\rho}$, s	T_{df}, ms	T_2, ms	λ	N
EDTA-CaHAp	$7.48 \cdot 10^{9}$	∞	4.99	0.25	0.80	–
EG-CaHAp	$1.23 \cdot 10^{10}$	∞	12.59	0.33	0.76	–
TA-CaHAp	$1.70 \cdot 10^{10}$	∞	7.14	0.32	0.85	–
GL-CaHAp	$2.04 \cdot 10^{10}$	∞	11.52	0.45	0.76	–
CA-CaHAp	$1.10 \cdot 10^{10}$	∞	3.22	0.29	0.466	–
CA-CaHAp	$5.879 \cdot 10^{9}$	∞	3.22	0.29	–	14.77
Radial distribution approach , n_{HH} = -1, ν_{MAS}=5 kHz							
Sample	I_0, a.u.	$T_{1\rho}$, s	T_{df}, ms	λ	b_{max}, Hz	b_{sc}, Hz	n_i
EDTA-CaHAp	$7.20 \cdot 10^{9}$	∞	4.27	0.84	1893	1022	30
EG-CaHAp	$9.47 \cdot 10^{9}$	∞	6.44	0.77	1664	694	30
TA-CaHAp	$1.56 \cdot 10^{10}$	∞	5.57	0.89	1844	831	30
GL-CaHAp	$1.85 \cdot 10^{10}$	∞	6.42	0.78	1722	191	30
CA-CaHAp	$1.07 \cdot 10^{10}$	∞	2.14	0.61	2124	694	30

The dominant peak at 0.43 nm together with minor peaks at 0.3 and 0.33 nm is clearly seen in the spatial distribution of protons surround ^{31}P nuclei. Moreover, the processing using radial distribution approach clearly allows to reduce far incoherent effects in the spatial distribution between ^{1}H and ^{31}P nuclei (Fig 4.3.3).

The CP behaviour in the CaHAps obtained using various complexing agents showed similar features as obtained for CA-CaHAp, namely fast rise and transient oscillations which were damped due to spin diffusion. The corresponding ^{1}H – ^{31}P CP kinetics of EDTA/EG/TA/GL-CaHAps under 5 kHz MAS condition are shown in figure 4.3.2. The CP behaviour seems rather similar for all nano-structured CaHAps only the oscilations in EDTA/EG-CaHAps are more pronounced.

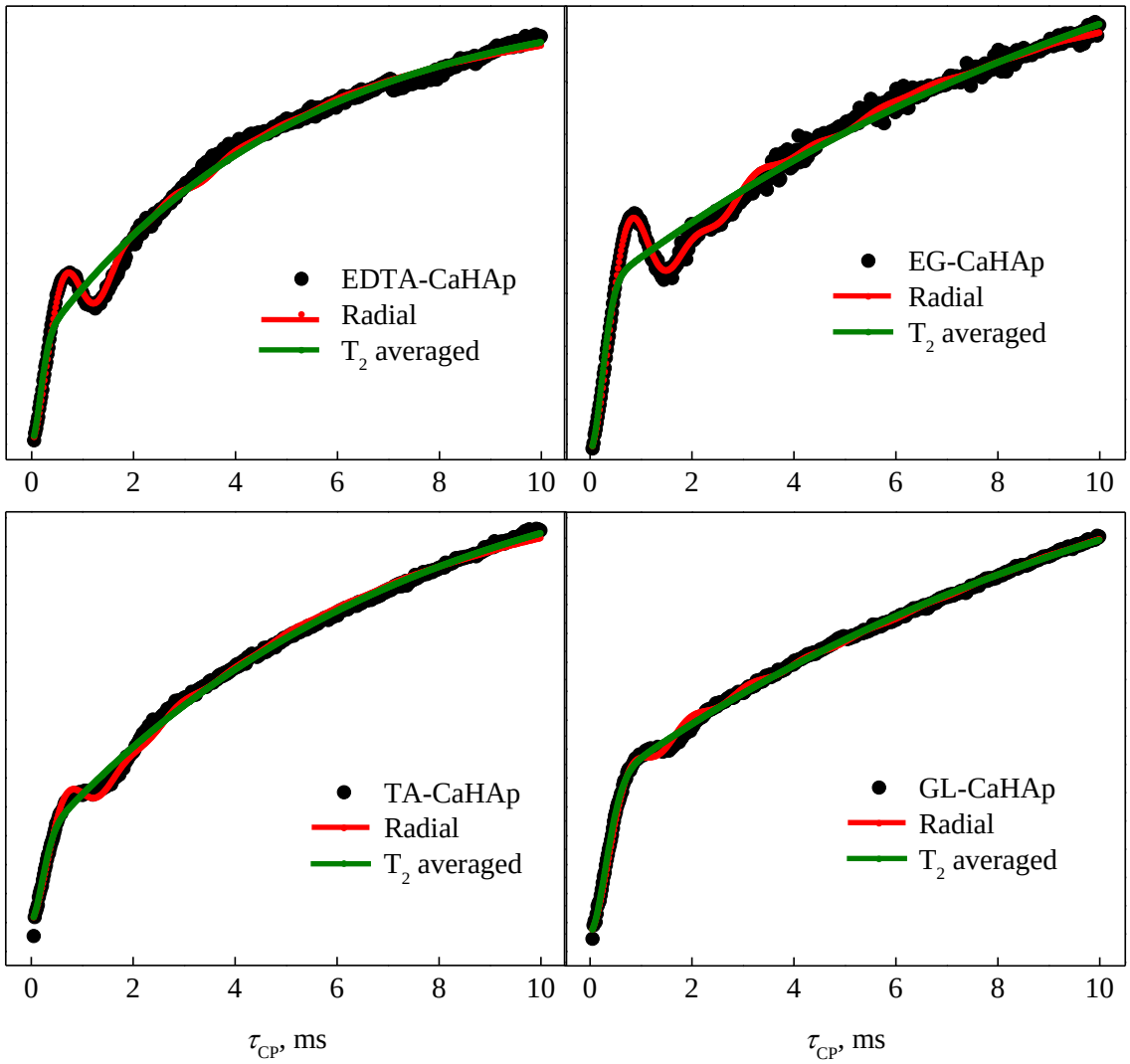

Fig. 4.3.2. ^{1}H-^{31}P CP kinetics in EDTA/EG/TA/GL-CaHAps together with theoretical fittings: Green line – eqs 4.2.22 and 4.2.23, Red line - eqs 4.2.22 and 4.2.23 using radial distribution instead of T_2 averaging approach. Obtained fitting parameters are shown in Table 4.3.1. More comments in the text.

The CP kinetics curves were processed using eqs 4.2.22 and 4.2.23 similarly as for CA-CaHAp. The parameters R^2 were obtained in the margins of 0.975-0.99 which show nice coincidence between the theoretical fitting and experiment. It is worth mentioning that the fitting results are rather provoking, namely in all of the samples parameter λ is between 0.76 and 0.85 which means that the quasi-equilibrium is not met. Comparing this observation with the results presented in chapter 4.1, where additional spectral lines appeared in ^{1}H and ^{31}P spectra of the corresponding CaHAps obtained during the aqueous sol gel

synthesis route, the idea comes to a mind that the lattice is slightly disrupted in these novel complex CaHAps. Such defects might be the reasoning for such behaviour. To corroborate this, there are similar values of λ calculated for similar understoichiometric HAp systems [75, 79]. Futhermore, the proton spin diffusion time constant T_{dif} vary within the CaHAps depending on the complexing agent used in the aqueous sol-gel synthesis route. In EDTA-CaHAp spin diffusion is the fastest and the time constant T_{dif} is more than two times smaller (4.99 ms) compared to EG-CaHAp and GL-CaHAp (12.59 ms and 11.52 ms respectively) whereas value obtained TA-CaHap (7.14 ms) is in the middle (table 4.3.1). Comparing these results to CA-CaHAp spin diffusion time T_{dif} (3.22 ms) appears that the CA-CaHAp lattice in the nanostructures is more proton-rich compared any other sol-gel derived CaHAp studied here [68]. The highest proton-deficit is seen in EG/GL-CaHAps. It is an exciting finding as it may be used as a probe to investigate minor differences and defects in the nano-structures. The parameters T_2 describing spin coupling distribution profiles width were calculated rather similar and varied between 0.25 and 0.33 for all the CaHAps except for GL-CaHAp which was equal to 0.45. Comparing this to the ^{31}P CP and BD spectra (Fig. 4.1.7) it is possible to address larger T_2 value to the present spectral line assigned to the disordered HPO_4.

The approximation using Radial distribution approach allowed to meet perfect fits (R^2 = 0.99 – 0.999) with the experiment for all of the sol-gel derived nano-structured CaHAps. The spin diffusion time T_{dif} for all CaHAps was calculated smaller compared to the one obtained using T_2 averaging approach. Though, the tendency was the same – it is 2-3 times smaller compared to the derived for CA-CaHAp which clearly proves that the lattice in the sol-gel derived CaHAps is less proton rich than in the stoichiometric nano-structured CA-CaHAp. The parameter λ is more or less independent on the chosen approach. The calculated spatial distributions of protons surround ^{31}P nuclei for all analysed nano-structured complex CaHAps are shown in Figure 4.3.3.

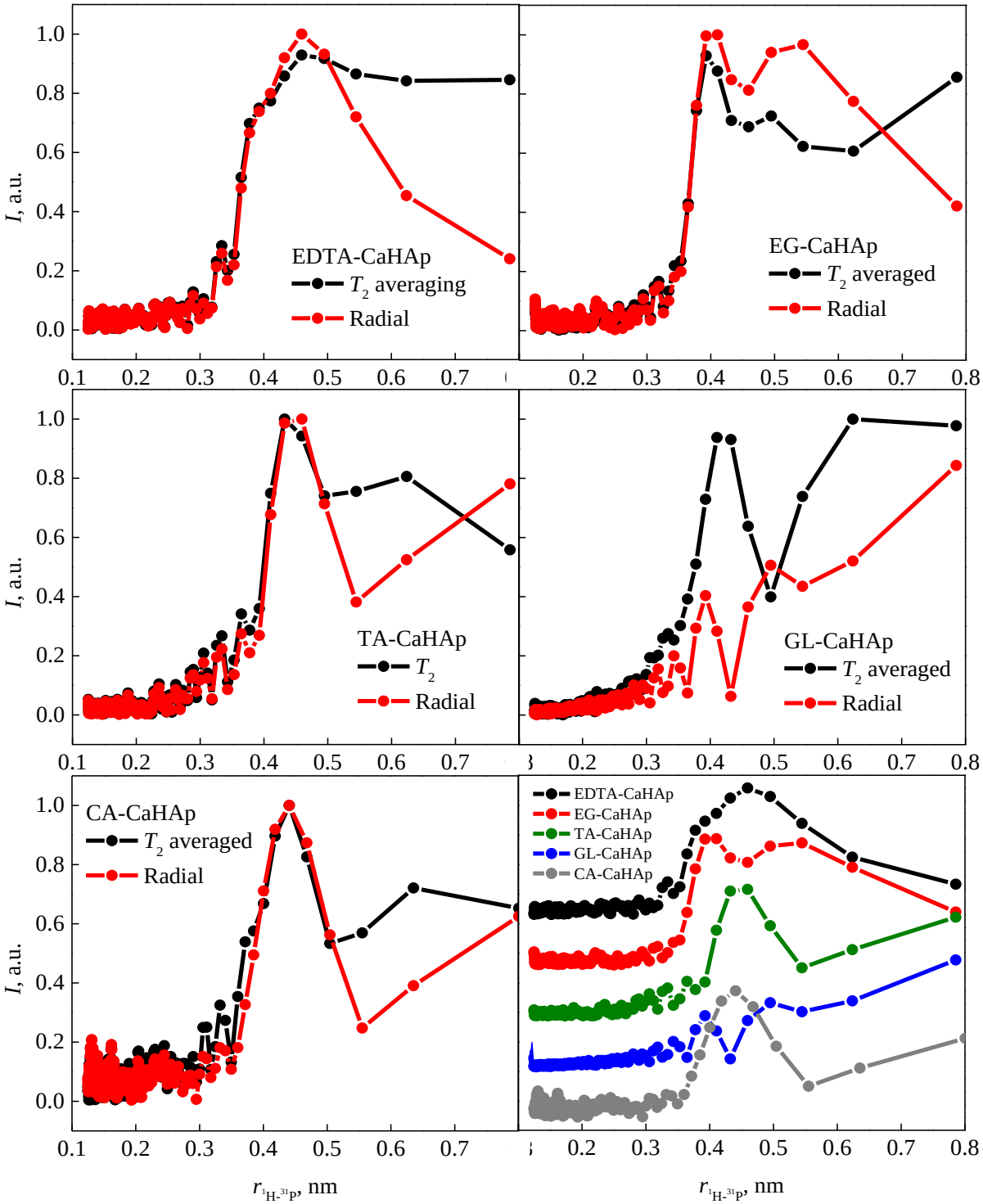

Fig. 4.3.3 Spatial distributions of protons surrounding ^{31}P nuclei in the EDTA/EG/TA/GL/CA-CaHAps at 5 kHz MAS. Spatial distributions were obtained using T_2 averaging (balck line) and Radial distribution (red line) approaches as well as averaging over angles. Relative intensity was normalized respectively to the most intense point. For comparison, all spatial distributions using radial distribution approach are shown in the lowest right graph. More details and comments in the graph and text.

They were calculated using dipolar coupling distribution $P(b/2)$ extracted from the experimental data applying formalism described in chapter 4.2.4, rescaling the dipolar coupling D respectively to the Hartmann-Hahn matching condition (present case n_{HH} = -1) and using T_2 averaging or Radial distribution approaches. It is clearly seen in figure 4.3.3 that the far range incoherent effects (> 0.5 nm) are better reduced using radial distribution approach. This observation nicely shows the benefit of using this approach. The spatial distribution profiles consist of 2 well resolved maxima at 0.39 nm, 0.44-0.49 nm. The differences are seen in their relative heights and in the resolution of the peaks. In pure crystalline CaHAp each P atom has two protons distanced at 0.385 nm, further two at 0.42 nm, while others are 0.6 nm or more away [127]. Particularly interesting is the presence of rather minor peaks at 0.3 - 0.33 nm. As discussed in chapter 4.2.2, distances of 0.21 – 0.25 nm are observed for P–O–H structural units from the surfaces layers and therefore extremely hardly seen applying various other experimental techniques, namely FTIR and NMR [71, 75]. The fact that the peaks for nano-structured CaHAps are observed in the spatial distribution profiles at 0.3 - 0.33 nm might be explained by the presence of defects within the HAp structure or they may arise from surface species. The spatial distributions correlate with FTIR spectroscopy data, namely the assigned surface O-H stretching vibration of the P-O-H groups in nano-structured CaHAps [53, 132]. Comparing all distance distribution profiles (fig 4.3.3 right lowest graph), it is possible to state that the tartaric acid used as complexing agent (TA-CaHAp) allows to produce nano-structured CaHAp which is the most similar with the commercially available CA-CaHAp according to their manifolds of the proximities between protons and ^{31}P nuclei in the nano-structures. Other two CaHAps, namely EDTA-CaHAp and EG-CaHap possess broader spatial distribution with better resolved peaks at 0.39 nm and 0.44-0.49 nm. The spatial distribution of the sample derived using glycerol as complexing agent (GL-CaHAP) drops out from the whole series of data (Fig 4.3.3) exhibiting certain peculiarities. What is more, in chapter 4.1 it was shown that the GL-CaHAp under CP conditions shows the appearance of

an unexpected peaks which were there assigned to the bulk disordered HPO_4 or surface H_xPO_4 and protonated HPO_4^{2-} groups. This observation is though provoking that the present sample is heterogenic. Moreover, ^1H-^{31}P HETCOR data shows two correlating spectral lines in GL-CaHAp 2D spectrum while only one is present for other nano-structured CaHAps (Fig. 4.3.4).

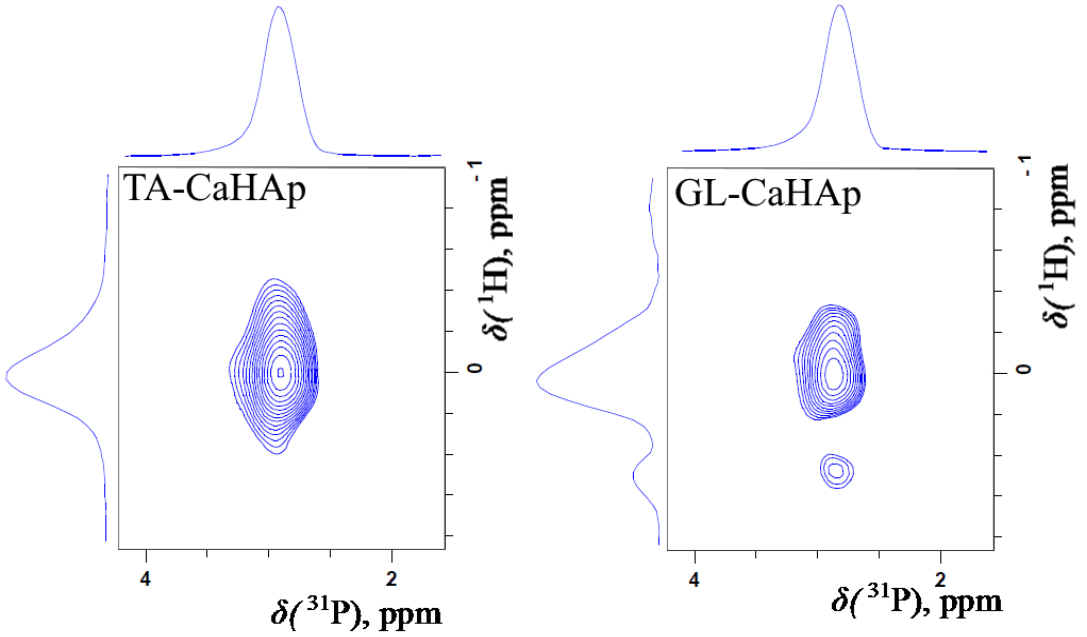

Fig. 4.3.4. A comparison between ^1H-^{31}P HETCOR spectra obtained for TA-CaHAp (right) and GL-CaHAp (left).

Note that the additional spectral line appearing for the GL-CaHAp specimen was not resolved in ^1H data as it was overlapped with much more intense line situating at 0ppm. As this peak is highlighted in HETCOR data it reveals that there are much shorter P…H contacts in the sample, most probably, from the protonated phosphate groups. It is a nice finding concerning fine details in the sample as the XRD data did not show any deviations from other CaHap specimens (see the Appendix). Also it was shown that the spatial 3D surface reconstruction of SEM micrographs of CaHAp samples synthesized by glycerate route was not possible. The unique CaHAp surface details of this specimen might be directly connected with sample heterogeneity. It was then

explained that the probability of formation of amorphous phosphate phase in the end product is higher [53]. This proposition rather agrees with the observed spatial distribution of protons surround ^{31}P nuclei in GL-CaHAp sample (Fig 4.3.3) as it seems that the sharp peaks are situated on the plateau, or in other words, on Gauss function shaped distribution, observed for the ACP-CaHap (Fig 4.2.7).

Summing up, it seems that the developed advanced processing routes for the CP kinetic data is a powerful tool to analyse nano-structured complex innovative materials. It allows to distinguish fine structural aspects concerning internuclear proximities between interacting spins in the novel compounds varying only in their morphological features at the nano- and meso-scales.

Conclusions of part 4.3

- The ^{1}H-^{31}P CP behaviour was described over the whole dynamic range for sol-gel derived EDTA/EG/TA/GL-CaHAps using non classical *I-I*-S* CP kinetics model applying radial distribution approach.

- The obtained fitting parameters allows to deduce that: i) quasi-equilibrium polarization is not accomplished for sol-gel derived EDTA/EG/TA/GL-CaHAps; ii) the crystal lattice in the sol gel derived EDTA/EG/TA/GL-CaHAps appears to have deficit of protons compared to the stoichiometric nano-structured CA-CaHAp.

- Minor structural differences in the nano-structured CaHAps, namely EDTA/EG/TA/GL/CA-CaHAps were indicated by the spatial distribution of protons surround ^{31}P nuclei.

- The higher level of the amorphous phosphate phase in the end CaHAp product using glycerate as a complexing agent in the sol-gel route was proven by the spatial distribution of protons surround ^{31}P nuclei.

Conclusions of the dissertation

1. ^{1}H and ^{31}P MAS NMR spectroscopy is a powerful experimental technique to analyse surface and bulk chemical species in the nano-structured sol-gel derived CaHAps as well as in the containing amorphous clustered phosphate phase (ACP) CaHAps. A precise analysis of the ^{1}H MAS NMR spectral contours allows to investigate the fine details of the structural organization of hydroxyl groups.

2. The existing CP kinetics models, namely the classical *I-S* and the non-classical *I-I*-S*, are not capable to describe CP behaviour in the nano-structured CaHAps over the whole dynamic range. The *I-I*-S* CP kinetics model complemented by introducing the cut-off averaging Gaussian distribution allows to describe the CP behaviour over the whole dynamic range and to determine the characteristic ^{1}H–^{31}P spin cluster size (0.3-0.5 nm).

3. The introduction of the radial distribution function for characterising spin coupling profile allows to reduce far range order incoherent effects and to resolve short contacts between ^{1}H and ^{31}P nuclei (0.24-0.27 nm) appearing from the surface species in the nano-structured CaHAp. It was shown that 9 kHz of MAS has a little impact to the spin diffusion process.

4. The advanced CP kinetic data processing routine was developed: the proper replica has been found that allowed to reduce the Fourier - Bessel (Hankel) transform calculating the angularly-averaged and purely distance-depending spin distribution profile to the routine Fourier transform.

5. The convergence of the non-classical *I*-*I**-*S* CP behaviour model to the classical *I*-*S* one was deduced. This clarifies the CP behaviour in the ACP-CaHAp: the classical *I*-*S* model describes the behaviour over the whole dynamic range, however the non-classical model seems to be more preferable because it directly provides the information on the spin diffusion rate that is originated from the exact microscopic quantum mechanical model.

6. The introduced CP kinetic data processing routine is powerful enough to distinguish the minor structural differences in the complex nano-structured CaHAps derived via aqueous sol-gel route using different complexing agents.

References

[1] F. Li, G. Li, H. Chen, J. Q. Jia, F. Dong, Y.B. Hu, Z. G. Shang, Y.X. Zhang, *Morphology and crystallinity-controlled synthesis of manganese cobalt oxide/manganese dioxides hierarchical nanostructures for high-performance supercapacitors*, J. Pow. Sourc.. 296, 86-91, (2015).

[2] M. Kumaresavanji, C.T. Sousa, A. Apolinario, A.M.L. Lopes, J.P. Araujo, *Influence of sol–gel parameters in the fabrication of ferromagnetic La2/3Ca1/3MnO3 nanotube arrays*, Mater. Sci. Eng. B-Adv. Funct. Solid-State Mater., 200, 117-123, (2015).

[3] O.M. Hemeda, N.Y. Mostafa, O.H. Abd Elkader, D.M. Hemeda, A. Tawfik, M. Mostafa, *Electrical and morphological properties of magnetocaloric nano ZnNi ferrite,* J. Magn. Magn. Mater., 394, 96-104, (2015).

[4] W. Zhang, T. Huynh, P. Xiu, B. Zhou, C. Ye, B.Q. Luan, R.H. Zhou, *Revealing the importance of surface morphology of nanomaterials to biological responses: Adsorption of the villin headpiece onto graphene and phosphorene*, Carbon., 94, 895-902, (2015).

[5] X.J. Chen, Y.Z. Dai, X.Y. Wang, *Methods and mechanism for improvement of photocatalytic activity and stability of* Ag_3PO_4, J. All. Compd., 649, 910-932, (2015).

[6] N.F. Mohammad, R. Othman, F.Y. Yeoh, *Controlling the pore characteristics of mesoporous apatite materials: Hydroxyapatite and carbonate apatite*, Ceram. Int., 41, 10624-10633, (2015).

[7] W. Habraken, P. Habibovic, M. Epple, M. Bohner, *Calcium phosphates in biomedical applications: materials for the future?* , Materials Today, 19 (2), 69–87, (2016).

[8] J.C. Elliott, M. L., Rakovan, J., Hughes, T. M., Eds., *Calcium phosphate biominerals.* In Reviews in Mineralogy & Geochemistry, Vol. 48; Kohn, Minerology Society of America, Washington, DC, 2002, p. 427-453.

[9] R. Z.Le Geros, *Calcium Phosphates in Oral Biology and Medicine*; Karger: Basel, 1991.

[10] P. W Brown, B. Constantz, B. *Hydroxyapatite and Related Materials*; CRC Press, 1994.

[11] H. Albee, S.J. Morrison, *Studies in bone growth, triple calcium phosphates as stimulus to osteogenesis*, Annals of Surgery, 71 (1), 32–39,(1920).

[12] C.P. Klein, K. de Groot, A.A. Drissen, H.B.M. van der Lubbe, *Interaction of biodegradable β-whitlockite ceramics with bone tissue: An in vivo study,* Biomat., 6(3), 189-192, (1985).

[13] P.S. Eggli, W. Muller, R.K. Schenk, *Porous hydroxyapatite and tricalcium phosphate cylinders with two different pore size ranges implanted in the cancellous bone of rabbits. A comparative histomorphometric and histologic study of bone ingrowth and implant substitution*, Clin. Orthop., 232, 127–138 ,(1988).

[14] D. Apelt, F. Theiss, A.O. El-Warrak, K. Zlinszky, R. Bettschart Wolfisberger, M. Bohner, S. Matter, J.A. Auer, B. von Rechenberg, *In vivo behavior of three different injectable hydraulic calcium phosphate cements*, Biomat., 25, 1439–1451, (2004).
[15] M. Bohner, H. Tiainen, P. Michel, N. Döbelin, *Design of an inorganic dual-paste apatite cement using cation exchange*, J. Mat. Scien.: Mat. in Med., 26, 1-13, (2015).
[16] G. Daculsi, *Biphasic calcium phosphate concept applied to artificial bone, implant coating and injectable bone substitute*, Biomat., 19 (16), 1473–1478, (1998)
[17] F. Barrere, M.E. Margot Snel, C. A. van Blitterswijk, K. de Groot, P. Layrolle, *Nano-scale study of the nucleation and growth of calcium phosphate coating on titanium implants*, Biomat., 25(14), 2901-2910, (2004).
[18] R.A. Levy, T.-M.G. Chu, J.W. Halloran, S.E. Feinberg, S. Hollister, *CT-generated porous hydroxyapatite orbital floor prosthesis as a prototype bioimplant*, AJNR Am. J. Neuroradiol., 18 (8), 1522–1525, (1997).
[19] H. Seitz, W. Rieder, S. Irsen, B. Leukers, C. Tille, *Three-dimensional printing of porous ceramic scaffolds for bone tissue engineering*, J. Biomed. Mater. Res. Part B: Appl. Biomater., 74 (2), 782–788, (2005).
[20] H. Lapczyna, L. Galea, S. Wüst, M. Bohner, S. Jerban, A. Sweedy, N. Doebelin, N. van Garderen, S. Hofmann, G. Baroud, R. Müller, B. von Rechenberg, *Effect of grain size and microporousity on the in vivo behavior of β-tricalcium phosphate scaffolds*, Eur. Cells and Mat., 28, 299-319, (2014).
[21] N. Groen, N. Tahmasebi, F. Shimizu, Y. Sano, T. Kanda, D. Barbieri, H. Yuan, P. Habibovic, C.A. van Blitterswijk, J. de Boer, *Exploring the Material-Induced Transcriptional Landscape of Osteoblasts on Bone Graft Materials,* Adv. Heal. Mat., 4,1691-1700, (2015)
[22] D. Smolen, T. Chudoba, I. Malka, A. Kedzierska, W. Lojkowski , W. Swieszkowski, K.J. Kurzydlowski, M. Kolodziejczyk-Mierzynska, M. Lewandowska-Szumiel, *Highly biocompatible, nanocrystalline hydroxyapatite synthesized in a solvothermal process driven by high energy density microwave radiation,* Int. J. of Nanomed., 8, 653-68, (2013).
[23] G. Ciobanu, G. Caria, O. Ciobanu, I. Sandu, *SEM and EDX studies of bioactive hydroxyapatite coatings on titanium implants,* Micron, 40, 143-146,(2009).
[24] A. Antonakos, E. Liarokapis, T. Leventouri, *Micro-Raman and FTIR studies of synthetic and natural apatites*, Biomaterials, 28, 3043-3054, (2007).
[25] I. Rehman, W. Bonfield, *Characterization of hydroxyapatite and carbonated apatite by photo acoustic FTIR spectroscopy*, J. Mat. Scien.: Mat. in Med., 8, 1-4, (1997).
[26] M.B, Osman, S. Diallo-Garcia, V. Herledan, D. Brouri, T. Yoshioka, J. Kubo, Y. Millot, G. Costentin, *Discrimination of Surface and Bulk Structure of Crystalline Hydroxyapatite Nanoparticles by NMR*, J. Phys. Chem. C, 119, 23008-23020, (2015).
[27] R.K. Harris, R.E. Wasylishen, M.J. Duer, *NMR Crystallography*, John Wiley and Sons Ltd, (2009)

[28] C.A. Fyfe, A.R. Lewis, J.M .Chezeau, *A Comparison of NMR Distance Determinations in the Solid State by Cross Polarization, REDOR and TEDOR Techniques*, Can. J. Chem., 77, 1984−1993, (1999).
[29] M. H. Levitt, *Spin Dynamics: Basics of Nuclear Magnetic Resonance*, John Wiley & Sons Ltd, (2008)
[30] E. Verron, J.M. Bouler, J. Guicheux, *Controlling the biological function of calcium phosphate bone substitutes with drugs*, Acta Biomaterialia 8, 3541–3551, (2012).
[31] R.Z. Le Geros, J.P. Le Geros, *Hydroxyapatite, in: Bioceramics and their clinical applications*, ed. T. Kokubo (Woodhead Publishing, Cambridge, 2008) pp. 367–394.
[32] S. Weiner, H.D. Wagner, *The material bone: Structure-Mechanical Function Relations*, Annu. Rev. Mater. Sci., 28 (1), 271–298, (1998).
[33] J.P. Nightingale, D. Lewis, *Pole Figures of the Orientation of Apatite in Bones*, Nature 232, 334–335, (1971).
[34] D.J. Zaner, R.A. Yukna, *Particle Size of Periodontal Bone Grafting Materials*, J. Periodontol. 55 (7), 406–409, (1984).
[35] S. Chernousova, J Klesing, N. Soklakovaa, M. Epple, *A genetically active nano-calcium phosphate paste for bone substitution, encoding the formation of BMP-7 and VEGF-A*, RSC Adv. 3 (28), 11155–11161, (2013).
[36] S. N. Bhaskar, J. M Brady, L. Getter, M. F. Grower, T. Driskell, *Biodegradable ceramic implants in bone: Electron and light microscopic analysis*, Oral. Surg. Oral. Med. Oral. Pathol., 32 (2), 336–346, (1971).
[37] P. Costantino, C. D. Friedman, K. Jones, L. C. Chow, G. A. Sisson, *Experimental Hydroxyapatite Cement Cranioplasty*, Plastic & Reconstructive Surgery, 90(2), (1992).
[38] S. Takagi, L. C. Chow, S. Hirayama, A. Sugawara, *Premixed calcium–phosphate cement pastes*, J. Biomed. Mater. Res. Part B: Appl. Biomater. 67 (2), 689–696, (2003).
[39] A.C. van Leeuwen, H. Yuan,G. Passanisi, J.W. van der Meer, J.D. de Bruijn, T.G. van Kooten, D.W. Grijpma, R.R.M. Bos, *Poly(trimethylene carbonate) and biphasic calcium phosphate composites) for orbital floor reconstruction: a feasibility study in sheep*, Eur. Cells Mater., 27, 81–97, (2014).
[40] P. Pascaud, P. Gras, Y. Coppel, C. Rey, S. Sarda, *Interaction between a Bisphosphonate, Tiludronate, and Biomimetic Nanocrystalline Apatites*, Langmuir 29, 2224−2232, (2013).
[41] M. Kawashita, K. Taninai, Z. Li, K. Ishikawa,·Y. Yoshida, *Preparation of low-crystalline apatite nanoparticles and their coating onto quartz substrates*, J. Materials Science: Materials in Medicine, 23, 1355–1362, (2012).
[42] K. Sunouchi, K. Tsuru, M. Maruta, G. Kawachi, S. Matsuya, Y. Terada and K. Ishikawa, *Fabrication of solid and hollow carbonate apatite microspheres as bone substitutes using calcite microspheres as a precursor*, Dental Materials Journal, 31, 549–557, (2012).
[43] I. Bogdanoviciene, K. Tonsuaadu, V. Mikli, I. Grigoraviciute-Puroniene,

A. Beganskiene, A. Kareiva, *pH impact on the sol-gel preparation of calcium hydroxyapatite, $Ca_{10}(PO_4)_6(OH)_2$, using a novel complexing agent, DCTA*, Centr. Eur. J. Chem., 8, 1323–1330, (2010).
[44] D. Milovac, G.G. Ferrer, M. Ivankovic, H. Ivankovic**,** *PCL-coated hydroxyapatite scaffold derived from cuttlefish bone: Morphology, mechanical properties and bioactivity*, Mater. Sci. Eng. C, 34, 437–445, (2014).
[45] P. Gentile, C.J. Wilcock, C.A. Miller, R. Moorehead, P.V. Hatton, *Process Optimisation to Control the Physico-Chemical Characteristics of Biomimetic Nanoscale Hydroxyapatites Prepared Using Wet Chemical Precipitation*, Materials, 8, 2297–2310, (2015).
[46] N. Kurgan, V. Karbivskyy, V. Kasyanenko, *Morphology and electronic structure of nanoscale powders of calcium hydroxyapatite,* Nanoscale Res. Lett., 10, 1–5, (2015).
[47] S. Pramanik, A.K. Agarwal, K.N. Rai, A. Garg, *Development of high strength hydroxyapatite by solid-state-sintering process*, Ceram. Int., 33, 419–426, (2007).
[48] K. Teshima, S. Lee, M. Sakurai, Y. Kameno, K. Yubuta, T. Suzuki, T. Shishido, M. Endo, S. Oishi, *Well-Formed One-Dimensional Hydroxyapatite Crystals Grown by an Environmentally Friendly Flux Method*, Cryst. Growth Des., 9, 2937–2940, (2009)
[49] H. Zreiqat, R. Roest, S. Valenzuela, A. Milev, B. Ben-Nissan, *Human Bone Derived Cell (HBDC) Behaviour of Sol-Gel Derived Carbonate Hydroxyapatite Coatings on Titanium Alloy Substrates,* Key Eng. Mater.,284–286, 541–544, (2005).
[50] I. Bogdanoviciene, A. Beganskiene, K. Tonsuaadu, J. Glaser, H.-J. Meyer, A. Kareiva, *Calcium hydroxyapatite, $Ca_{10}(PO_4)_6(OH)_2$ ceramics prepared by aqueous sol–gel processing*, Mater. Res. Bull., 41, 1754–1762, 2006.
[51] M. Malakauskaite-Petruleviciene, Z. Stankeviciute, A. Beganskiene, A. Kareiva, *Sol–gel synthesis of calcium hydroxyapatite thin films on quartz substrate using dip-coating and spin-coating techniques*, J. Sol-Gel Sci. Technol., 71, 437–446, (2014).
[52] S. Ramesh, A.N. Natasha, C.Y. Tan, L.T. Bang, A. Niakan, J. Purbolaksono, H. Chandran, C.Y. Ching, S. Ramesh, W.D. Teng, *Characteristics and properties of hydoxyapatite derived by sol–gel and wet chemical precipitation methods***,** Ceram. Int.**,** 41**,** 10434**–**10441, (2015).
[53] S. Kareiva, V. Klimavicius, A. Momot, J. Kausteklis, A. Prichodko, L. Dagys, F. Ivanauskas, S. Sakirzanovas, V. Balevicius, A. Kareiva, *Sol-gel synthesis, phase composition, morphological and structural characterization of $Ca_{10}(PO_4)_6(OH)_2$: XRD, FTIR, SEM, 3D SEM and solid-state NMR studies*, J. Mol. Struct., 1119, 1–11, (2016).
[54] Y. Suetsugu, J. Tanaka, *Crystal growth and structure analysis of twin-free monoclinic hydroxyapatite*, J. Mat. Scien. Mat. in Med., 13, 767-772, (2002).
[55] G.M. Poralan Jr., J.E. Gambe, E.M. Alcantara, R.M. Vequizo, *X-ray diffraction and infrared spectroscopy analyses on the crystallinity of engineered biological hydroxyapatite for medical application*, Mat. Scien. Eng., 79, 012028, (2015).

[56] C.K. Loong, C. Rey, L.T. Kuhn, C. Combes, Y. Wu, S.H. Chen, M.J. Glimcher ,*Evidence of Hydroxyl-Ion Deficiency in Bone Apatites: An Inelastic Neutron-Scattering Study*, Bone, 26 (6), 599–602, (2000).
[57] T. Leventouri, C.E. Bunaciu, V. Perdikatsis, *Neutron powder diffraction studies of silicon-substituted hydroxyapatite*, Biomaterials, 24(23), 4205-4211, (2003).
[58] D. Arcosa, J. Rodriguez-Carvajala, M. Vallet-Regib, *Neutron scattering for the study of improved bone implants*, Physica B, 350, 607–610, (2004).
[59] D. Arcosa, J. Rodríguez-Carvajala, M. Vallet-Regí, *The effect of the silicon incorporation on the hydroxylapatite structure. A neutron diffraction study*, Sol. St. Scien., 6, 987–994, (2004).
[60] V. Klimavicius, A. Kareiva, V. Balevicius, *Solid-State NMR Study of Hydroxyapatite Containing Amorphous Phosphate Phase and Nano-Structured Hydroxyapatite: Cut-Off Averaging of CP MAS Kinetics and Size Profiles of Spin Clusters*, J. Phys. Chem. C, 118 (49), 28914-28921, (2014)
[61] K. Kristinaityte, L. Dagys, J. Kausteklis, V. Klimavicius, I. Doroshenko, V. Pogorelov, N.R. Valveviciene, V. Balevicius, *NMR and FTIR studies of clustering water molecules: From low-temperature matrices to nano-structured materials used in innovative medicine*, J. Mol. Liq, 235, 1-6, (2016).
[62] S. K. Padmanabhan, A. Balakrishnah, M. Chu, Y.J. Lee, T.N. Kim, S. Cho, *Sol-Gel synthesis and characterization of hydroxyapatite nanorods*, Particuolgy, 7, 466-470, 2009.
[63] A. Anwar, I.U. Rehman, J. A. Darr, *Low-Temperature Synthesis and Surface Modification of High Surface Area Calcium Hydroxyapatite Nanorods Incorporating Organofunctionalized Surfaces*, J. Phys. Chem. C, 120, 29069−29076, (2016).
[64] D. Lee, C. Leroy, C. Crevant, L. Bonhomme-Coury, F. Babonneau, D. Laurencin, C. Bonhomme, G. Paepe, *Interfacial Ca2+ environments in nanocrystaline apatites revealed by dynamic nuclear polarization enhanced ^{43}Ca NMR spectroscopy*, Nat. Commun., 8, 14104, (2017).
[65] C. Gervais, D. Laurencin, A. Wong, F.Pourpoint, J. Labram, B. Woodward, A.P. Howes, K.J. Pike, R. Dupree, F. Mauri, C. Bonhomme, M.E. Smith, *New perspectives on calcium-oxygen bonds: a combined computational-experimental ^{43}Ca NMR approach*, Chem. Phys. Lett., 464, 42-48, (2008).
[66] D. Laurencin, A. Wong, R. Dupree, M.E. Smith, *Natural abundance ^{43}Ca solid state NMR characterization of hydroxyapatite: identification of the two calcium sites*, Magn. Reson., Chem, 46, 347-350, (2008).
[67] H. Kiyono, Y. Matsuda, T. Shimada, M. Ando, I. Oikawa, H. Maekawa, S. Nakayama, S. Ohki, M. Tansho, T. Shimidzu, P. Florian, *Oxygen-17 nuclear magnetic resonance measurements on apatite-type lanthanum silicate ($La_{9.33}(SiO_4)_6O_2$)*, Sol. Stat. Ion., 228, 64-69, (2012).
[68] A. Kaflak-Hachulska, A. Samoson, W. Kolodziejski, *^{1}H MAS and ^{1}H -^{31}P CP/MAS NMR Study of Human Bone Mineral*, Calc. Tiss. Int., 13 (5), 476-486, (2003).

[69] C. Jager, T. Welzel, W. Meyer-Zaika, M. Epple, *Solid-State NMR Investigation of the Structure of Nanocrystalline Hydroxyapatite*, Magn. Reson. Chem., 44, 573−580, (2006).
[70] S. Hayakawa, T. Kanaya, K. Tsuru, Y. Shirosaki, A. Osaka, E. Fujii, K. Kawabata, G. Gasqueres, C. Bonhomme, F. Babonneau, C. Jäger, H.J. Kleebe, *Heterogeneous structure and in vitro degradation behavior of wet-chemically derived nanocrystalline silicon-containing hydroxyapatite particles,* Acta Biomater., 9, 4856 -4867, (2013).
[71] A. Vyalikh, P. Simon, T. Kollmann, R. Kniep, U. Scheler, *Local Environment in Biomimetic Hydroxyapatite−Gelatin Nanocomposites As Probed by NMR Spectroscopy*, J. Phys. Chem. C, 115, 1513–1519, (2011).
[72] R. Mathew, P.N. Gunawidjaja, I. Izquierdo-Barba, K. Jansson, A. Garcia, D. Arcos, M. Vallet-Regi, M. Eden, *Solid-State ^{31}P and ^{1}H NMR Investigations of Amorphous and Crystalline Calcium Phosphates Grown Biomimetically From a Mesoporous Bioactive Glass,* J. Phys. Chem. C, 115, 20572- 20582, (2011).
[73] A. Kaflak, D. Chmielewski, W. Kolodziejski, *Solid-state NMR study of discrete environments of bone mineral nanoparticles using phosphorus-31 relaxation*, J. Appl. Biomed., 14, 321-330, (2016).
[74] A. Vyalikh, P. Simon, E. Rosseeva, J. Buder, R. Kniep, U. Scheler, *Intergrowth and Interfacial Structure of Biomimetic Fluorapatite–Gelatin Nanocomposite: A Solid-State NMR Study*, J. Phys. Chem. B, 118, 724 –730, (2014).
[75] J. Kolmas, A. Jaklewicz, A. Zima, M. Bućko, Z. Paszkiewicz, J. Lis, A. Ślosarczyk, W. Kolodziejski, *Incorporation of carbonate and magnesium ions into synthetic hydroxyapatite: The effect on physicochemical properties,* J. Mol. Struct., 987, 40-50, (2011).
[76]A. Kaflak, W. Kolodziejski, *Kinetics of ^{1}H-^{31}P NMR cross-polarization in bone apatite and its mineral standards*, Magn. Reon. Chem, 46, 335-341, (2008).
[77] C.H. Yoder, J.D. Pasteis, K.N. Worcester, D. Schermerhorn, *Structural Water in Carbonated Hydroxyapatite and Fluorapatite: Confirmation by Solid State ^{2}H NMR*, Calcif. Tissue Int., 90, 60−67, (2012).
[78] A. Kaflak, D. Chmielewski, A. Gorecki, W. Kolodziejski, *Kinetics of ^{1}H-^{31}P cross-polarization in human trabecular bone*, Sol. Stat. NMR, 10(4),191-195, (1998).
[79] J. Kolmas, W. Kolodziejski, *Inverse ^{31}P-^{1}H NMR Cross Polarization in Hydratated Nanocrystalline Calcium Hydroxyapatite*, Chem. Phys. Lett., 554, 128-132, (2012).
[80] P. Bertani, J. Raya, P Reinheimer, R. Gougeon, L. Delmotte, J. Hirschinger, *$^{19}F/^{29}Si$ Distance Determination in Fluoride-Containing Octadecacil by Hartmann-Hahn Cross-Polarization under Fast Magic Angle Spinning*, Solid State NMR, 13, 219-229, (1999).
[81] K. Yamamoto, V.L. Ermakov, D.K. Lee, A. Ramamoorthy, *PINTASEMA-MAS, a solid-state NMR method to measure heteronuclear dipolar coupling under MAS*, Chem. Phys. Lett., 408, 118-122, (2005).

[82] Y. Nishiyama, M. Malon, M.J. Potrzebowski, P. Paluch, J.P. Amoureux, *Accurate NMR determination of C-H or N-H distances for unlabeled molecules*, Sol. Stat. NMR, 73, 15-21,(2016).
[83] J. Ren, H. Eckert, *DQ-DRENAR with back-to-back (BABA) excitation: Measuring homonuclear dipole-dipole interactions in multiple spin-1/2 systems*, Sol. Stat. NMR, 71, 11-18, (2015).
[84] M. Hologne, P. Bertani, T. Azraïs, C. Bonhomme, J. Hirschinger, *$^{1}H/^{31}P$ Distance Determination by Solid State NMR in Multiple-Spin Systems*, Solid State Nucl. Magn. Reson., 28, 50−56, (2005).
[85] G. Mollica, M. Dekhil, F. Ziarelli, P. Thureau, S. Viel, *Probing crystal packing of uniformly 13C-enriched powder samples using homonuclear dipolar coupling measurements*, Sol. Stat. NMR, 65, 114-121, (2015).
[86] G. Mali, N. Rajic, N. Zabukovec Logar, V. Kaucic, *Solid-StateNMR Study of an Open-Framework Aluminophosphate-Oxalate Hybrid*, J. Phys. Chem. B, 107, 1286−1292, (2003).
[87] G. Mali, V. Kaucic, *Determination of distances between aluminium and spin-1/2 nuclei using cross polarization with very weak radio –frequency fields*, J. Chem. Phys., 117(7), 3327-3339, (2002).
[88] M.J. Potrzebowski, J. Gajda, W. Cieselski, I.M, Montesinos, *Distance measurements in disodium ATP hydrates by means of ^{31}P double quantum two-dimensional solid-state NMR spectroscopy*, J. Magn. Reson., 179, 173-181, (2006).
[89] F.G Vogt, D.J Aurentz, K.T Mueller, *Determination of internuclear distances from solid-state nuclear magnetic resonance: Dipolar transforms and regularization methods*, Mol. Phys, *95, 907 (1998)*
[90] S.R. Hartmann, E.L. Hahn, *Transfer of magnetisation from protons to low gamma nuclei*, Phys. Rev., 128, 2042–2046, (1962).
[91] A. Pines, M.G. Gibby, J.S. Waugh, *Proton-Enhanced Nuclear Induction Spectroscopy. A Method for High Resolution NMR of Dilute Spins in Solids*, J. Chem. Phys., 56, 1776 (1972).
[92] M. Ernst, B.H. Meier, *Lecture Notes. High-Resolution Solid-State NMR: Principles and Applications*, ETH Zurich, Switzerland.
[93] E.O. Stejskal, J. Schaefer, J.S. Waugh, *Magic-angle spinning and polarization transfer in proton-enhanced NMR*, J. Magn. Reson., 28, 105, (1977).
[94] W. Kolodziejski, J. Klinowski, *Kinetics of Cross-Polarization in Solid-State NMR: A Guide for Chemists*, Chem. Rev., 102, 613−628, (2002).
[95] L. Muller, A. Kumar, T. Baumann, R.R. Ernst, *Transient Oscillations in NMR Cross-Polarization Experiments in Solids*, Phys.Rev.Lett, 32(25), 1402-1406, (1974).
[96] L.B. Alemany, D.M. Grant, T.D. Alger, R.J. Pugimire, *Cross polarization and magic angle sample spinning NMR spectra of model organic compounds. 3. Effect of the carbon-13-proton dipolar interaction on cross polarization and carbon-proton dephasing*, JACS, 105, 6697-6704, (1983).
[97] E.M. Purcell, H.C. Torrey, R.V. Pound, *Resonance Absorption by Nuclear Magnetic Moments in a Solid*, Phys. Rev. 69(1), 37-38, (1946)

[98] F. Bloch, W.W. Hansen, M. Pacard, *Nuclear induction*, Phys. Rev. 69, 127, (1946).
[99] A. Abragam, *Principles of Nuclear Magnetism*, Clarendon press, Oxford U.K., (1961).
[100] J. Keeler, *Understanding NMR spectroscopy*, Wiley, The Atrium, Southern Gate Chichester, England, (2002).
[101] D. N. Nikogosyan, *Nonlinear Optical Crystals: A Complete Survey* (Springer Science + Business Media Inc., New York, 2005), pp. 133–145.
[102] D. Xue and H. Ratajczak, *Effect of hydrogen bonds on physical properties of ammonium dihydrogenphosphate crystals*, J. Mol. Struct.: THEOCHEM 716, 207-210, (2005).
[103] D. Xu, D. Xue, *Chemical bond analysis of the crystal growth of KDP and ADP*,J. Cryst. Growth, 286, 108-113, (2006).
[104]A. A. Khan and W. H. Baur, *Refinement of the crystal structures of ammonium dihydrogen phosphate and ammonium dihydrogen arsenate*, Acta Crystallogr., Sect. B: Struct. Crystallogr. Cryst. Chem., 29, 2721-2726, (1973).
[105]N. Peres, A. Boukhris, M. Souhassou, G. Gavoille, and C. Lecomte, *Electron density in ammonium dihydrogen phosphate: non-uniqueness of the multipolar model in simple inorganic structures*, Acta Crystallogr., Sect. A: Found. Crystallogr. A55, 1038-1048, (1999).
[106]T. Fukami, S. Akahoshi, K. Hukuda, and T. Yagi, *Refinement of the Crystal Structure of $NH_4H_2PO_4$ above and below Antiferroelectric Phase Transition Temperature*, J. Phys. Soc. Jpn., 56, 2223-2224, (1987).
[107]T. Fukami, S. Akahoshi, K. Hukuda, and T. Yagi, *X-Ray Study of Thermal Parameters of $NH_4H_2PO_4$ and $ND_4D_2PO_4$ in the Paraelectric Phase*, J. Phys. Soc. Jpn. 56, 4388-4392, (1987).
[108]L. Tenzer, B. C. Frazer, and R. Pepinsky, *A neutron structure analysis of tetragonal $NH_4(H_2PO_4)$*, Acta Crystallogr. 11, 505-509, (1958).
[109]N. Peres, M. Souhassou, B. Wyncke, G. Gavoille, A. Cousson, W. Paulus, *Neutron diffraction study of the paraelectric phase of ammoniumdihydrogen phosphate (ADP): hydrogen bonding of NH_4^-*, J. Phys.: Condens. Matter 9, 6555-6562, (1997).
[110]R. R. Choudhury, R. Chitra, *Influence of N-H-O hydrogen bonds on the structure and properties of $(K_{(1-x)}(NH_4)_{(x)}H_2PO_4)$ proton glasses: a single crystal neutron diffraction study*, J. Phys.Condens. Matter, 25, 075902 (2013).
[111] V. Klimavicius, L. Dagys, V. Balevicius, *Sub-Nano Scale Order and Spin Diffusion in Complex Solids through the Processing of Cross Polarization Kinetics*, The Journal of Physical Chemistry C, 120 (6), 3542–3549, (2016).
[112] OrigigLab Corporation, http://www.OriginLab.com,
[113] http://www.ptc.com/product/mathcad/
[114] M.M. Maricq, J.s. Waugh, *NMR in Rotating solids*, J. Chem. Phys., 70, 3300-3316, (1979).
[115] M.J Thrippleton, M, Cutajar, S. wimperis, *Magic Angle Spinning (MAS) NMR linewidths in the presence of solid-state dynamics*, Chem. Phys. Lett., 452, 233-238, (2008).

[116] B. Grünberg, T. Emmler, E. Gedat, I. Shenderovich, G.H. Findenegg, H.H. Limbach, G. Buntkowsky, *Hydrogen Bonding of Water Confined in the Mesoporous Silica MCM-41 and SBA-15 Studied by 1H Solid-State NMR*, Chem. Eur. J., 10, 5689 – 5696, (2004).
[117] H.H. Limbach, P.M. Tolstoy, N.Perez-Hernandez, J.Guo, I.G, Shenderovich, G.S. Denisov, *OHO Hydrogen Bond Geometries and NMR Chemical Shifts: From Equilibrium Structures to Geometric H/D Isotope Effects, withApplications for Water, Protonated Water, and Compressed Ice*, Israel J. Chem., 49, 199-216, (2009).
[118] M. Nakahara, C. Wakai, *Monomeric and Cluster of Water Molecules in Organic Solvent*, Chem. Lett., 21(5), 809-812, (1992).
[119] L. Dagys, V. Klimavicius, J. Kausteklis, A. Chodosovskaja, V. Aleksa, A. Kareiva, V. Balevicius, *Solid State ^{1}H and ^{31}P NMR and FTIR Spectroscopy study of Static and Dynamic Structures in Sol-gel derived Calcium Hydroxyapatites*, Lith. Phys, 55(1), 1-9, (2015).
[120] A.P. Legrand, H. Sfihi, N. Lequeux, J. Lemaitre, *^{31}P Solid-State NMR Study of the Chemical Setting Process of a Dual-Paste Injectable Brushite Cements*, J. Biomed. Mater. Res. Part B: Appl. Biomater., 91, 46-54, (2009).
[121] R.K. Hester, J.L. Ackermann, V.R. Cross, J.S. Waugh, *Resolved Dipolar Coupling Spectra of Dilute Nuclear Spins in Solids*, Phys. Rev. Lett., 34, 993-995, (1975).
[122] S. Ando, R.K. Harris, S.A. Reisenberg, *Analysis of Cross-Polarization Dynamics between Two abundant nuclei , ^{19}F and ^{1}H, based on Spin Thermodynamics Theory*, J. Magn. Reson., 141, 91-103, (1999).
[123] R. Zhang, J. Damron, T. Vosegaard, A. Ramamoorthy, *A cross-polarization based rotating-frame separated-local-field NMR experiment under ultrafast MAS conditions*, J. Magn. Resn., 250, 37-44, (2015).
[124] A. Vyalikh, P. Simon, E. T. Kolmann, R. Kniep, U. Scheler, *Local environment in Biomimetic Hydroxyapatite-Gelatin Nanocomposites As probed by NMR Spectroscopy*, J. Phys. Chem. C, 115, 1513-1519, (2011).
[125] J.M. Ziman, *Models of disorder. The Theoretical Physics of Homogeneously Disodered Systems*, Cambridge University Press, London (1979).
[126] G.P. Holland, R. Sharma, J.O. Agola, S. Amin, V.C. Solomon, P Singh, D. A. Buttry, J.L. Yager, *NMR Characterization of Phosphonic Acid Capped SnO_2 Nanoparticles*, Chem. Mater., 19, 2519-2526, (2007).
[127] W. Kolodziejski, *Solid-State NMR Studies of Bone*, Top. Curr. Chem., 246, 235-270, (2005).
[128] T. Azraïs, L. Bonhomme-Coury, J. Vaissermann, P. Bertani, J. Hirschinger, J. Maquet, C. Bonhomme, *Synthesis and Characterization of a Novel Cyclic Aluminophosphinate: Structure and Solid- State NMR Study*, Inorg. Chem., 41, 981−988, (2002).
[129] T.C Stringfellow, J.D Trudeau, T.C Farrar, *Experimental and Theoretical Studies of the P-H Bond Length and Stretching Mode of the Phoshite Anion*, J. Phys. Chem., 97, 3985-3989, (1993).

[130] K.T Muller**,** *Analytic Solutions for the Time Evolution of Dipolar-Dephasing NMR Signals*, J. Magn. Reson. Ser. A, 113, 81-93, (1995).
[131] J. Mathews, R. Walker, *Mathematical methods of Physics*, W.A. Benjamin, Inc., Amsterdam, New York, (1964)
[132] T. Ishikawa, A.Teramachi, H. Tanaka, A. Yasukawa, K . Kandori, *Fourier Transform Infrared Spectroscopy Study of Deuteration of Calcium Hydroxyapatite Particles,* Langmuir, 16, 10221-10226, (2000).
[133] V. Klimavicius, L. Dagys, V. Chizik, V. Balevicius, *CP MAS Kinetics Study of Ionic Liquids Confined in Mesoporous Silica: Convergence of Non-Classical and Classical Spin Coupling Models,* Appl. Magn. Reson., XX, XX-XX, (2017).
[134] D. Sakellariou, P. Hodgkinson, S. Hedinger, L. Emsley, *Experimental observation of periodic quasi-equilibia in the solid state*, Chem. Phys. Lett., 308, 381-389, (1999).
[135] V. Ladizhansky, S. Vega, *Polarization transfer dynamics in Lee-Goldburg cross polarization nuclear magnetic resonance experiments on rotating solids*, J. Chem. Phys., 112(16), 7158-7168, (2000).
[136] R. Gupta, G. Hou, T. Polenova, A.J. Vega, *RF inhomogeneity and how it controls CPMAS*, Sol. Stat. Nucl. Magn. Reson, 72, 17-26, (2015).
[137] S.R. Kasturi, P.R. Moran, *Study of antiferroelectric ammonium duhydrogen phosphate (ADP) by pulsed NMR*, Phys. Rew. B, 12(5), 1874-1884, (1975).

Appendix

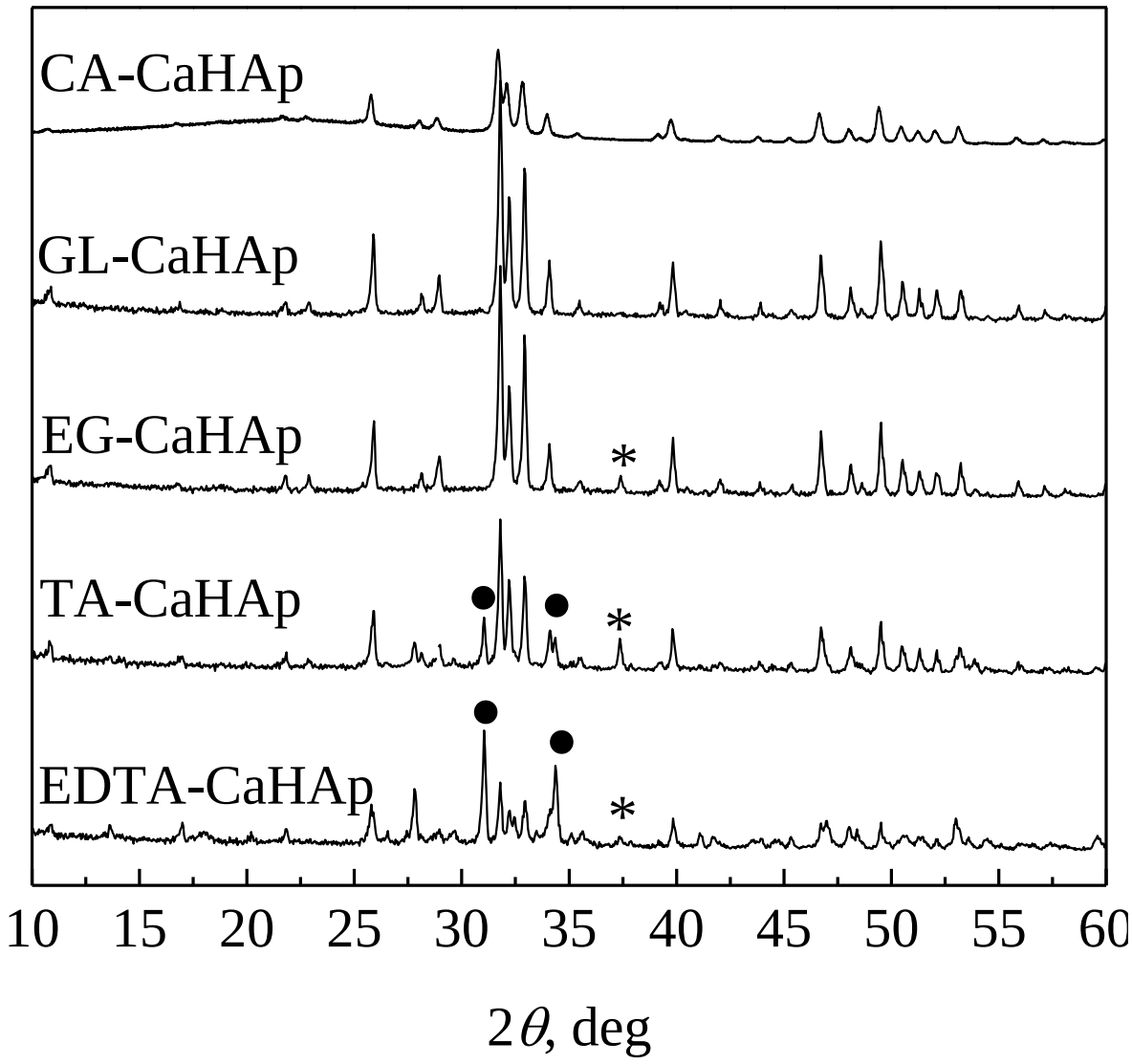

Fig. AI. XRD patterns of CA/GL/EG/TA/EDTA-CaHAps. Impurity phases: $Ca_3(PO_4)$ - *, CaO - ●.

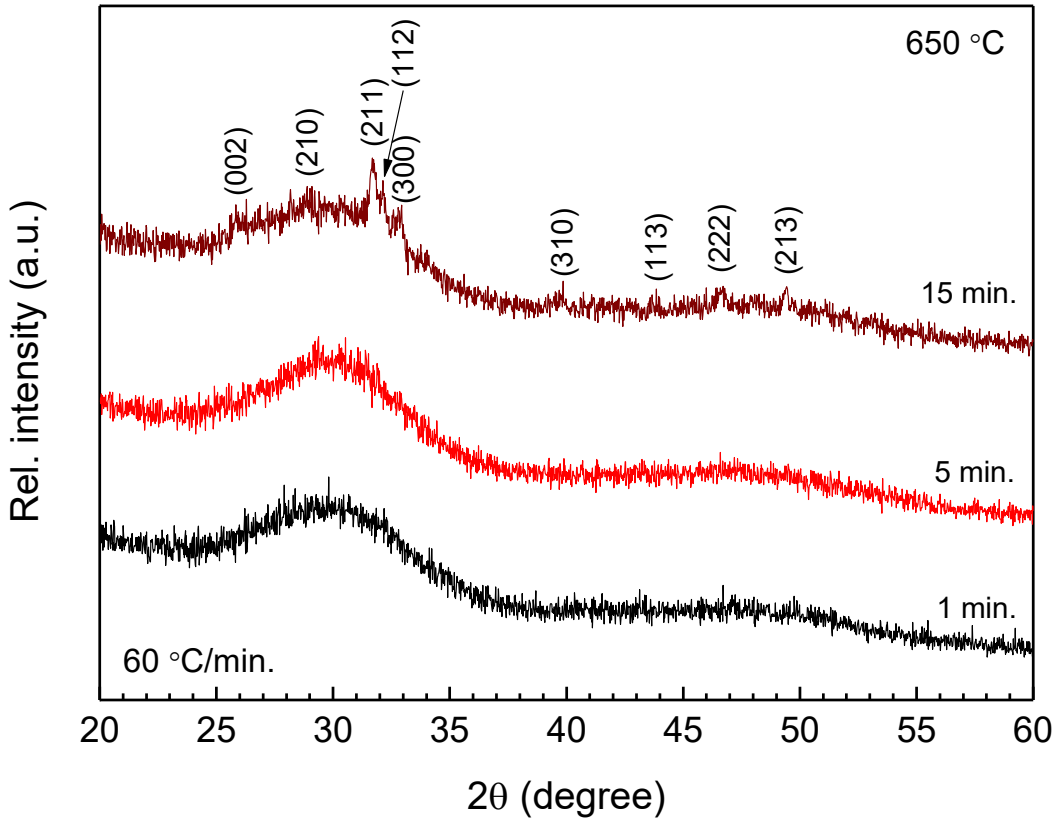

Fig. AII. XRD patterns of ACP-CaHAp depending on the sintering time at 650˚C.

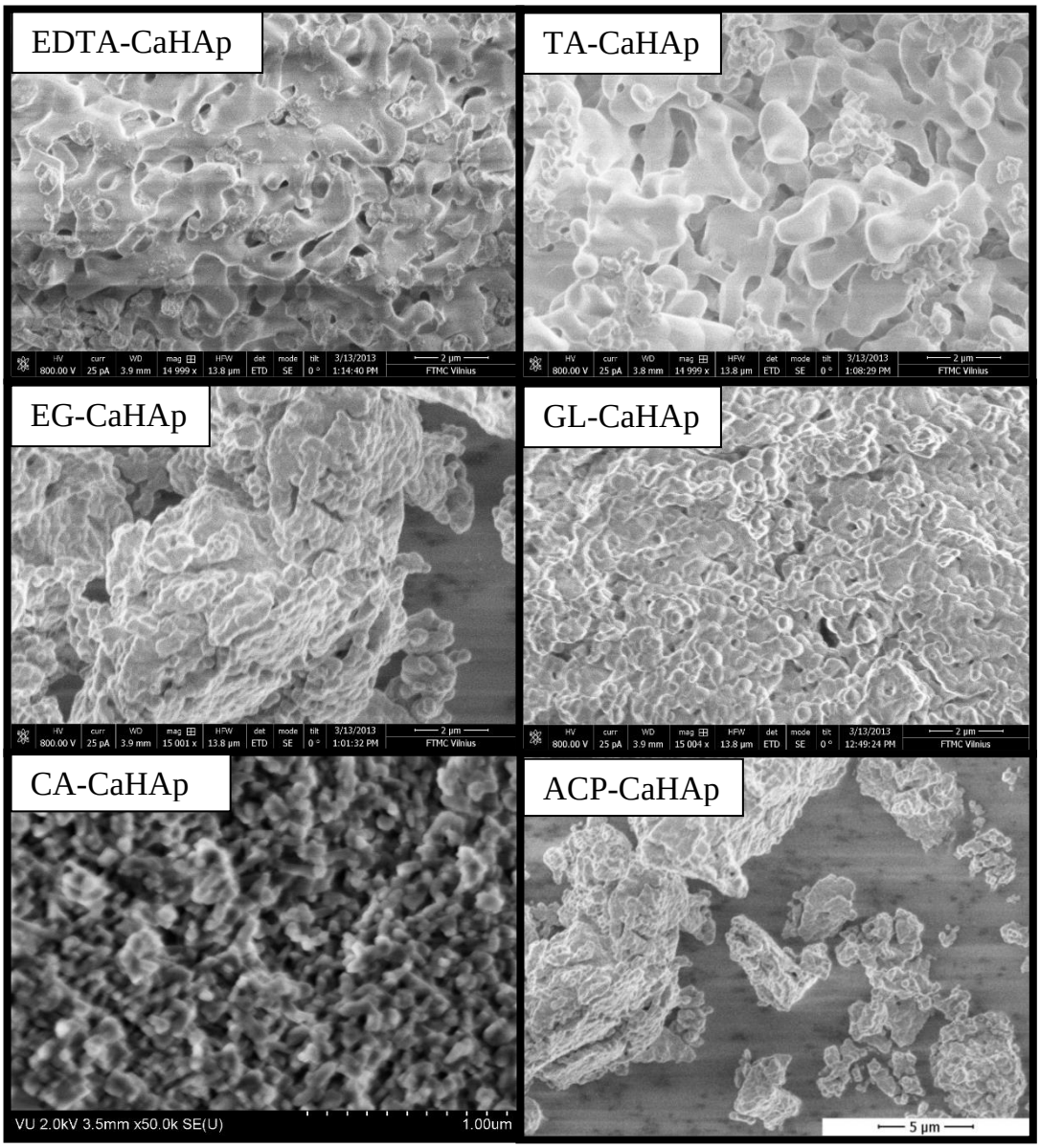

Fig AIII. SEM micrographs of EDTA/TA/EG/GL/CA/ACP-CaHAps. See the scale in the figure.